

Springer Theses

Recognizing Outstanding Ph.D. Research

Junfeng He

Angle-Resolved Photoemission Spectroscopy on High-Temperature Superconductors

Studies of Bi2212 and Single-Layer
FeSe Film Grown on SrTiO_3
Substrate

 Springer

Springer Theses

Recognizing Outstanding Ph.D. Research

Aims and Scope

The series “Springer Theses” brings together a selection of the very best Ph.D. theses from around the world and across the physical sciences. Nominated and endorsed by two recognized specialists, each published volume has been selected for its scientific excellence and the high impact of its contents for the pertinent field of research. For greater accessibility to non-specialists, the published versions include an extended introduction, as well as a foreword by the student’s supervisor explaining the special relevance of the work for the field. As a whole, the series will provide a valuable resource both for newcomers to the research fields described, and for other scientists seeking detailed background information on special questions. Finally, it provides an accredited documentation of the valuable contributions made by today’s younger generation of scientists.

Theses are accepted into the series by invited nomination only and must fulfill all of the following criteria

- They must be written in good English.
- The topic should fall within the confines of Chemistry, Physics, Earth Sciences, Engineering and related interdisciplinary fields such as Materials, Nanoscience, Chemical Engineering, Complex Systems and Biophysics.
- The work reported in the thesis must represent a significant scientific advance.
- If the thesis includes previously published material, permission to reproduce this must be gained from the respective copyright holder.
- They must have been examined and passed during the 12 months prior to nomination.
- Each thesis should include a foreword by the supervisor outlining the significance of its content.
- The theses should have a clearly defined structure including an introduction accessible to scientists not expert in that particular field.

More information about this series at <http://www.springer.com/series/8790>

Junfeng He

Angle-Resolved Photoemission Spectroscopy on High-Temperature Superconductors

Studies of Bi2212 and Single-Layer FeSe
Film Grown on SrTiO₃ Substrate

Doctoral Thesis accepted by
The University of Chinese Academy of Sciences, China

 Springer

Author

Dr. Junfeng He
Institute of Physics
Chinese Academy of Sciences
Beijing
China

Supervisor

Prof. Xingjiang Zhou
Institute of Physics
Chinese Academy of Sciences
Beijing
China

ISSN 2190-5053

Springer Theses

ISBN 978-3-662-52730-6

DOI 10.1007/978-3-662-52732-0

ISSN 2190-5061 (electronic)

ISBN 978-3-662-52732-0 (eBook)

Library of Congress Control Number: 2016940328

© Springer-Verlag Berlin Heidelberg 2016

This work is subject to copyright. All rights are reserved by the Publisher, whether the whole or part of the material is concerned, specifically the rights of translation, reprinting, reuse of illustrations, recitation, broadcasting, reproduction on microfilms or in any other physical way, and transmission or information storage and retrieval, electronic adaptation, computer software, or by similar or dissimilar methodology now known or hereafter developed.

The use of general descriptive names, registered names, trademarks, service marks, etc. in this publication does not imply, even in the absence of a specific statement, that such names are exempt from the relevant protective laws and regulations and therefore free for general use.

The publisher, the authors and the editors are safe to assume that the advice and information in this book are believed to be true and accurate at the date of publication. Neither the publisher nor the authors or the editors give a warranty, express or implied, with respect to the material contained herein or for any errors or omissions that may have been made.

Printed on acid-free paper

This Springer imprint is published by Springer Nature

The registered company is Springer-Verlag GmbH Berlin Heidelberg

Parts of this thesis have been published in the following journal articles:

Junfeng He, Xu Liu, Wenhao Zhang, Lin Zhao, Defa Liu, Shaolong He, Daixiang Mou, Fansen Li, Chenjia Tang, Zhi Li, Lili Wang, Yingying Peng, Yan Liu, Chaoyu Chen, Li Yu, Guodong Liu, Xiaoli Dong, Jun Zhang, Chuangtian Chen, Zuyan Xu, Xi Chen, Xucun Ma, Qikun Xue and X. J. Zhou. “Electronic Evidence of an Insulator-Superconductor Crossover in Single-Layer FeSe/SrTiO₃ Films” PNAS **111**, 18501–18506 (2014)

Zhuojin Xie, Shaolong He, Chaoyu Chen, Ya Feng, Hemian Yi, Aiji Liang, Lin Zhao, Daixiang Mou, Junfeng He, Yingying Peng, Xu Liu, Yan Liu, Guodong Liu, Xiaoli Dong, Li Yu, Jun Zhang, Shenjin Zhang, Zhimin Wang, Fengfeng Zhang, Feng Yang, Qinjun Peng, Xiaoyang Wang, Chuangtian Chen, Zuyan Xu, and X. J. Zhou. “Orbital-Selective Spin Texture and its Manipulation in a Topological Insulator” Nature Communications **5**, 3382 (2014)

Junfeng He, Wentao Zhang, JinMo Bok, Daixiang Mou, Lin Zhao, Yingying Peng, Shaolong He, Guodong Liu, Xiaoli Dong, Jun Zhang, J. S. Wen, Z. J. Xu, G. D. Gu, Xiaoyang Wang, Qinjun Peng, Zhimin Wang, Shenjin Zhang, Feng Yang, Chuangtian Chen, Zuyan Xu, H.-Y. Choi, C. M. Varma and X. J. Zhou. “Coexistence of Two Sharp-Mode Couplings and Their Unusual Momentum Dependence in the Superconducting State of Bi₂Sr₂CaCu₂O_{8+δ} Superconductor Revealed by Laser-Based Angle-Resolved Photoemission” Physical Review Letters **111**, 107005 (2013)

Shaolong He, Junfeng He, Wenhao Zhang, Lin Zhao, Defa Liu, Xu Liu, Daixiang Mou, Yun-Bo Ou, Qing-Yan Wang, Zhi Li, Lili Wang, Yingying Peng, Yan Liu, Chaoyu Chen, Li Yu, Guodong Liu, Xiaoli Dong, Jun Zhang, Chuangtian Chen, Zuyan Xu, Xi Chen, Xucun Ma, Qikun Xue and X. J. Zhou. “Phase Diagram and Electronic Indication of High Temperature Superconductivity at 65K in Single-Layer FeSe Films” Nature Materials **12**, 605–610 (2013)

Defa Liu, Wenhao Zhang, Daixiang Mou, Junfeng He, Yun-Bo Ou, Qing-Yan Wang, Zhi Li, Lili Wang, Lin Zhao, Shaolong He, Yingying Peng, Xu Liu, Chaoyu Chen, Liyu, Guodong Liu, Xiaoli Dong, Jun Zhang, Chuangtian Chen, Zuyan Xu, Jiangping Hu, Xi Chen, Xucun Ma, Qikun Xue and X. J. Zhou. “Electronic Origin of High-temperature Superconductivity in Single-layer FeSe Superconductor” Nature Communications **3**, 931 (2012)

Guodong Liu, Guiling Wang, Yong Zhu, Hongbo Zhang, Guochun Zhang, Xiaoyang Wang, Yong Zhou, Wentao Zhang, Haiyun Liu, Lin Zhao, Jianqiao Meng, Xiaoli Dong, Chuangtian Chen, Zuyan XU and X. J. Zhou, Development of a Vacuum Ultraviolet Laser-Based Angle-Resolved Photoemission System with a Superhigh Energy Resolution Better Than 1 meV, Review of Scientific Instruments **79**, 023105 (2008)

Supervisor's Foreword

Many novel quantum materials have been discovered with unusual physical properties and exotic phenomena, such as high-temperature superconductivity in copper oxide compounds, colossal magnetoresistance in manganites, high-temperature iron-based superconductors, and topological insulators and related materials. These unusual behaviors are dictated by the electrons and their interaction with other entities in the materials. Therefore, probing the electronic structure of materials with emergent phenomena holds the key to unravel the underlying physics. Angle-resolved photoemission spectroscopy (ARPES), which directly measures the electronic structure of a material via photoelectrons, has been demonstrated to be a powerful experimental tool in condensed matter physics. This book focuses on the unique electronic structures of two high-temperature superconductors: $\text{Bi}_2\text{Sr}_2\text{CaCu}_2\text{O}_{8+\delta}$ (Bi2212) and single-layer FeSe films grown on SrTiO_3 substrate, which differentiate it from the previous ARPES books. Clear many-body effects are observed in Bi2212 (Chaps. 4 and 5), and distinct electronic structures compatible with high-temperature superconductivity are obtained in FeSe/ SrTiO_3 films (Chaps. 6–8).

High-temperature superconductivity, a central theme in condensed matter physics, has generated continuous efforts in unveiling the driving mechanism since its first observation in cuprates in 1986. The interest has been re-energized by a recent discovery of high- T_c superconductivity in the iron-based superconductors in 2008. Although a final consensus is yet to be reached, considerable progresses have been made in both experiment and theory. The current status and a brief review of the studies in cuprates and the iron-based superconductors are given in Chap. 1.

Among these progresses, ARPES has played an important role in revealing the single-particle spectral function of the materials which contains the fundamental information of electron interaction and electron pairing in superconductors. In Chap. 2, the basic principles and theoretical formalisms of the ARPES technique are reviewed and introduced.

As a state-of-the-art technique, ARPES has been experiencing continuous development in the past decades. By using a vacuum ultraviolet (VUV) laser as the light source, super-high energy resolution with unprecedented data quality can be obtained, which enables the studies of fine electronic structures in high- T_c superconductors. The later realization of tunable photon energies in VUV laser has greatly enhanced the capability of the laser-based ARPES. A combination of laser-based ARPES and Mott detectors has provided a unique pathway toward the complete characterization of electrons (energy, momentum, and spin) with super-high resolution. By utilizing the latest time-of-flight electron analyzer, a real-time 2D detection of momentum is realized. In Chap. 3, several state-of-the-art ARPES systems with unique capabilities are introduced.

Chapter 4 presents the study of many-body effects in Bi2212 by laser-based ARPES. Two prominent energy scales are observed to coexist in a large area of momentum space in the superconducting state. One energy scale is seen over the Fermi surface from nodal to antinodal regions with nearly a fixed energy of ~ 78 meV, whereas the other energy scale evolves from the antinodal region to the nodal region with its energy varying from ~ 40 meV to ~ 70 meV. These observations have solved the long-standing puzzle about the momentum evolution between nodal kink and antinodal kink in cuprates.

In Chap. 5, fine electronic features are presented in the angle-integrated spectra of Bi2212 in the superconducting state. These features bear some resemblances to those observed in Pb by tunneling which, via McMillan–Rowell inversion, provided the direct evidence for electron–phonon-mediated electron pairing in conventional superconductors.

Single-layer FeSe films grown on SrTiO₃ substrate represent a special and important case in the iron-based superconductors, which have the simplest crystal structure but exhibit a record-high T_c . Chapter 6 shows the electronic structure and energy gap of the superconducting FeSe film. The Fermi surface consists only of electron-like pockets near Brillouin zone corner without indication of any Fermi surface around the zone center. Nearly isotropic superconducting gap without a gap node has been defined in this typical 2D system. These observations have provided stringent constraints to the superconductivity theories and demonstrated the simplest electronic structure compatible with high- T_c superconductivity in the iron-based superconductors.

Chapter 7 establishes the electronic phase diagram of single-layer FeSe films grown on SrTiO₃ substrate. Two distinct phases are observed through an extensive *in situ* annealing process. The electronic phase with low carrier concentration shows some similarities to that of the parent compound of BaFe₂As₂ superconductors, whereas the other electronic phase becomes superconducting with sufficient carrier concentration. A record-high T_c of ~ 65 K is observed in the superconducting phase with an optimized carrier density.

Chapter 8 describes the investigation of an insulator to superconductor crossover in single-layer FeSe films grown on SrTiO₃ substrate. The clear evolution has been identified with increasing carrier concentration which exhibits similar behaviors to that observed in the cuprate superconductors. These results suggest that the reduced

dimensionality and the interfacial effect may enhance the electron correlation in the system. They have added a significant piece of information to the understanding of superconductivity origin and provided a new pathway in searching for novel superconductors.

We hope the experimental methods introduced in this book will stimulate and further push the ongoing efforts in advancing the ARPES technique and the scientific results presented here will shed insights in understanding the mechanism of high-temperature superconductivity. We would like to thank Springer for the encouragement, support, and patience.

Beijing
March 2016

Prof. Xingjiang Zhou

Acknowledgements

First, I would like to thank my supervisor Prof. Xingjiang Zhou. He always supported me and encouraged me. I really appreciate the freedom he gave me on the research. Although very busy, he always made himself available whenever I wanted to discuss with him. Thanks to his guidance and help, I really enjoyed my stay in the Zhou group. To me, he is not only a supervisor but also a friend in need.

I also appreciate the help from Guodong Liu, Xiaoli Dong, Shaolong He, and Jun Zhang at the Institute of Physics. I learned a lot of technical details about our laser light source from Guodong, and I did enjoy the collaboration with Shaolong on the FeSe project.

I was very lucky to work with Lin Zhao and Wentao Zhang, who sacrificed a lot of time to teach me during my early years in the Zhou group.

I am also grateful to Jianqiao Meng, Haiyun Liu, Xiaowen Jia, Daixiang Mou, Shanyu Liu, Chaoyu Chen, Xu Liu, Zhuojin Xie, Ya Feng, Hemian Yi, and others who worked with me in the Zhou group. Of course, I want to mention Yingying Peng, Yan Liu, Defa Liu, and Cheng Hu, who spent a lot of time working with me on the laser ARPES system.

Zhuojin Xie, Yuxiao Zhang, Defa Liu, Cong Li, and Ping Ai provided constructive comments and suggestions to my thesis.

Concluding, I would like to mention my parents and wife. Their continuous support made the work in this book possible.

Contents

1	Introduction	1
1.1	Observation of Superconductivity	1
1.2	Cuprate Superconductors	3
1.2.1	The Crystal Structure of Cuprates	3
1.2.2	The Phase Diagram of Cuprates	5
1.2.3	The Electronic Structure of Cuprates	6
1.2.4	The Theoretical Models of Cuprates	8
1.2.5	Many-Body Effects in Cuprates	10
1.3	Iron-Based Superconductors	12
1.3.1	The Crystal Structure of Iron-Based Superconductors	12
1.3.2	The Phase Diagram of Iron-Based Superconductors	13
1.3.3	The Electronic Structures of Iron-Based Superconductors	14
1.3.4	The Magnetic Structures of Iron-Based Superconductors	14
1.3.5	The Theoretical Models for Iron-Based Superconductors	15
	References	18
2	Angle-Resolved Photoemission Spectroscopy	21
2.1	Energy Resolution of ARPES	22
2.1.1	ARPES Measures the Occupied States	23
2.1.2	The Selection of Work Function	24
2.2	Momentum Resolution of ARPES	24
2.2.1	Momentum Conservation in Step One: Ejection of Electrons from Initial to Final States	25
2.2.2	Momentum Conservation in Step Two: Traveling of the Excited Electrons to Sample Surface	26

2.2.3	Momentum Conservation in Step Three: Escape of the Excited Electrons into the Vacuum	27
2.2.4	Determination of K_z in 3D Systems [2, 15]	29
2.3	Physical Properties Measured by ARPES [1, 2]	30
2.3.1	Transition Probability for the Optical Excitation	30
2.3.2	Single-Particle Spectral Function	33
	References	33
3	ARPES Systems.	35
3.1	Constituents and Categories of ARPES Systems	36
3.1.1	Constituents of a Typical ARPES System	36
3.1.2	Categories of ARPES Systems.	37
3.2	Vacuum Ultraviolet Laser-Based ARPES System.	38
3.2.1	Energy Resolution of the System [2]	40
3.2.2	Space Charge Effect Test [2].	41
3.2.3	Angular Mode and Momentum Resolution Test [2]	44
3.2.4	Bulk Sensitivity Test of the 6.994 eV Laser ARPES [2]	45
3.2.5	Modifications on the Helium Discharge Lamp of the ARPES System	47
3.3	Tunable Laser-Based ARPES System.	49
3.4	Spin-Resolved Laser-Based ARPES System	50
3.5	Time-of-Flight System	54
	References	57
4	Coexistence of Two Sharp-Mode Couplings in $\text{Bi}_2\text{Sr}_2\text{CaCu}_2\text{O}_{8+\delta}$.	59
4.1	Introduction	59
4.2	Materials and Methods	60
4.3	Observation of Two Coexisting Energy Features	60
4.4	Momentum Dependence of the Energy Features	62
4.5	Temperature Dependence of the Energy Features	64
4.6	Doping Dependence of the Energy Features	66
4.7	The Possible Origin of the Coexisting Energy Features.	66
4.8	Simulation of the Electron–Boson Coupling	67
4.9	Challenge to the Conventional Understanding	68
4.10	Summary	69
	References	69
5	Similar Energy Features in $\text{Bi}_2\text{Sr}_2\text{CaCu}_2\text{O}_{8+\delta}$ and Pb	71
5.1	Introduction	71
5.2	Observation of the Fine Structures	73
5.3	Temperature Dependence of the Fine Structures.	74
5.4	Momentum Dependence of the Fine Structures	75
5.5	Summary	78
	References	79

6	Electronic Structures of the Superconducting Single-Layer FeSe/SrTiO₃ Films	81
6.1	Introduction	81
6.2	Method	83
6.2.1	Preparation and Post-Annealing of the Single-Layer FeSe Films	83
6.2.2	Calibration of the Sample Temperature	83
6.2.3	High-Resolution ARPES Measurements	84
6.3	Fermi Surface and Band Structure	84
6.4	Temperature Dependence of the Superconducting Gap	86
6.5	Momentum Dependence of the Superconducting Gap	87
6.6	Discussion	89
	References	91
7	Phase Diagram and High T_c Superconductivity in Single-Layer FeSe Films	95
7.1	Introduction	95
7.2	Materials and Methods	96
7.2.1	Thin Film Preparation and Post-Annealing	96
7.2.2	Sample Temperature Calibration	98
7.2.3	High-Resolution ARPES Methods	98
7.3	Coexistence and Evolution of Two Competing Phases	98
7.3.1	Observation of Two Competing Phases and Their Evolution with Carrier Concentration	98
7.3.2	Electronic Structure for the N Phase, the S Phase, and the Intermediate State	102
7.4	Carrier Concentration Change Induced by Post-Annealing	104
7.5	N Phase of the Single-Layer FeSe Film and the Magnetic Phase of BaFe ₂ As ₂	105
7.6	Optimization of the High-Temperature Superconductivity in the Superconducting Phase	107
7.7	Examination of Particle–Hole Symmetry Along the Fermi Surface	109
7.8	Phase Diagram of the Single-Layer FeSe Films	110
7.9	Summary	111
	References	112
8	Insulator–Superconductor Crossover in Single-Layer FeSe/SrTiO₃ Films	115
8.1	Introduction	116
8.2	Materials and Methods	117
8.3	Doping Evolution of the Energy Gaps in Single-Layer FeSe/SrTiO ₃ Films	117

8.4	Two Distinct Gaps	118
8.4.1	Different Temperature Dependence of the Gap Size	118
8.4.2	Different Temperature Dependence of the Peak Intensity	120
8.5	Similar Doping Evolution Between S Phase of FeSe Films and Cuprates	121
8.5.1	Single-Layer FeSe/SrTiO ₃ Films and La-doped Bi ₂ Sr ₂ CuO _{6+δ}	121
8.5.2	Single-Layer FeSe/SrTiO ₃ Films and La _{2-x} Sr _x CuO ₄	122
8.6	Origin of the Insulator–Superconductor Crossover and Strong Electron Correlation	124
8.7	Summary	125
	References	125

Chapter 1

Introduction

1.1 Observation of Superconductivity

There was a long-standing question in human history: Is it possible to get zero resistance in a material? It was thought to be unrealistic in the early years because it seemed that the scattering between electrons and atoms (impurities) is unavoidable, which should give rise to resistivity. Moreover, ultralow temperature was thought to be an enemy to decreasing resistance. Naively, everything is supposed to be “frozen” near zero K, including electrons. Therefore, the resistance should increase dramatically when the temperature gets very low. However, all these “natural” ideas were changed after the famous experiment performed by K. Onnes et al. in the year of 1911 [1]. This experiment was made possible by the successful liquefaction of helium. Onnes et al. successfully lowered the temperature to 4.2 K, near which they found that the resistance of Hg went to zero, as shown in Fig. 1.1. This observation was totally different from the earlier expectation that the resistance should increase at low temperature. On the contrary, it represented the first example of zero resistance conductor, which was named as “superconductor” by Onnes. People immediately realized that the discovery of superconductivity might bring a new revolution to science and industry if the superconductors can be broadly used, and Onnes was awarded the Nobel Prize in 1913. In the years after, more superconductors were found in different elements and simple compounds. Meanwhile, the expulsion of magnetic field was also broadly found in the superconducting materials, which was named as “Meissner effect.” “Meissner effect” is the second key character of superconductors besides “zero resistance” [2]. However, after many years, people were disappointed that the transition temperatures (T_c s) in all the discovered superconductors were very low and the application was yet to be realized. Nevertheless, great progresses were made in understanding the superconductivity. The BCS theory [3] successfully describes the origin of superconductivity and the authors, Bardeen, Cooper and Schrieffer, were awarded the Nobel Prize in 1972. However, a maximum temperature of ~ 40 K was given by the BCS theory as the upper limit of T_c , which disappointed many people.



Onnes (1853-1926)

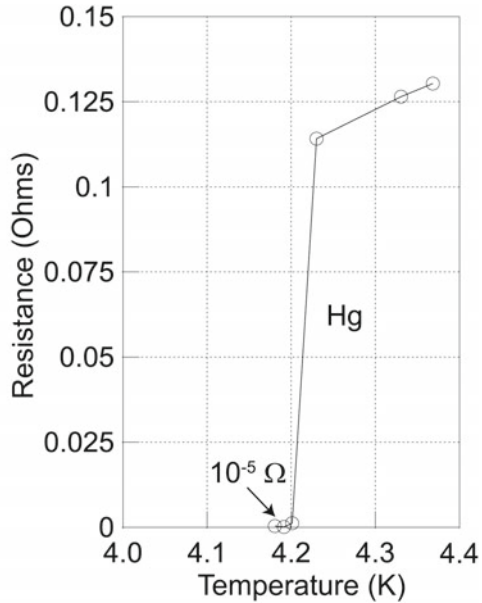


Fig. 1.1 Observation of superconductivity. *Left panel* Onnes. *Right panel* superconductivity in Hg below 4.2 K [1]

This limit was later known as “McMillan limit.” If this limit is true, then the broad application of superconductors would not be possible.

However, the human history is a history of discovery. New observations always enrich or renew the original understandings. Similar to the observation of superconductivity which changed the original understanding of resistance at low temperature, the later observation of high-temperature superconductors had also refreshed people’s minds by breaking the “McMillan limit.” In the year of 1986, a T_c of 35 K was found in cuprate (La-Ba-Cu-O) by Bednorz and Müller [4]. Then, a remarkable T_c of higher than 90 K was observed in the material of Y-Ba-Cu-O independently by Prof. Chu’s group in the USA [5] and Prof. Zhao’s group in China [6]. This T_c is higher than the “McMillan limit” and within the temperature range that liquid nitrogen can reach which makes the real application of superconductivity possible. So far, the highest T_c was observed in $\text{HgBa}_2\text{Ca}_2\text{Cu}_3\text{O}_{8+x}$ with a value of $\sim 130\text{K}$ at normal ambient pressure [7], which can be enhanced to $\sim 160\text{K}$ at high pressure [8]. In Fig. 1.2, the transition temperatures of various superconductors were plotted versus their observation times, respectively.

However, despite the continuous efforts, people were not able to find any system other than cuprates which has a T_c higher than 40 K in the following 20 years. As for the origin of high-temperature superconductivity in cuprates, although many progresses have been made, a final understanding has yet to be reached. Part of the reason is the complexity of cuprates. Too many striking phenomena coexist in cuprate which

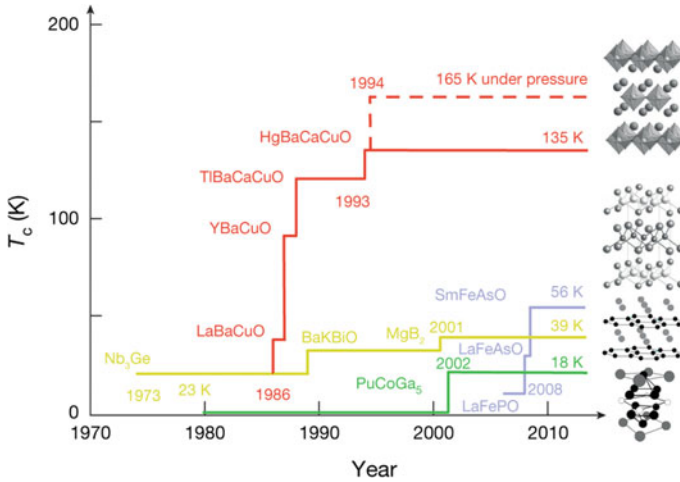


Fig. 1.2 The observation of high T_c cuprate superconductors. Reprinted with the permission from Macmillan Publishers Ltd: [9], copyright 2015

makes it very hard to distinguish the one related to high-temperature superconductivity from others. Therefore, it is very important to find another high-temperature superconducting system. On the one hand, it can provide more options for the possible applications. On the other hand, by comparing two different systems and looking for the phenomena in common, one can get the key insight in understanding the high-temperature superconductivity. In 2008, Prof. Hosono’s group observed a T_c as high as 26 K in $LaOFeAs$ [10]. Right after this observation, Prof. Xianhui Chen’s group at the university of science and technology of China and Prof. Nanlin Wang’s group at the institute of physics(IOP), Chinese academy of sciences(CAS), observed remarkable T_c s of 43 K and 41 K in $SmFeAsO_{0.85}F_{0.15}$ and $CeFeAsO_{0.84}F_{0.16}$, respectively [11, 12]. These temperatures broke the “McMillan limit” again. Later, Prof. Zhongxian Zhao’s group at IOP and Prof. Zhuan Xu’s group at Zhejiang university discovered new iron-based superconductors with T_c s as high as 55–56 K [13, 14]. Recently, an electronic indication of high-temperature superconductivity at ~ 65 K was observed in a collaborative work performed by our group and Prof. Qikun Xue’s group [15] which will be presented in the following chapters.

1.2 Cuprate Superconductors

1.2.1 The Crystal Structure of Cuprates

Most of cuprate superconductors crystallize in a perovskite structure consisting of different layers. Generally, the layers are labeled as “copper oxygen plane” and “charge reservoirs.” The “copper oxygen plane” is supposed to be the layer on which super-

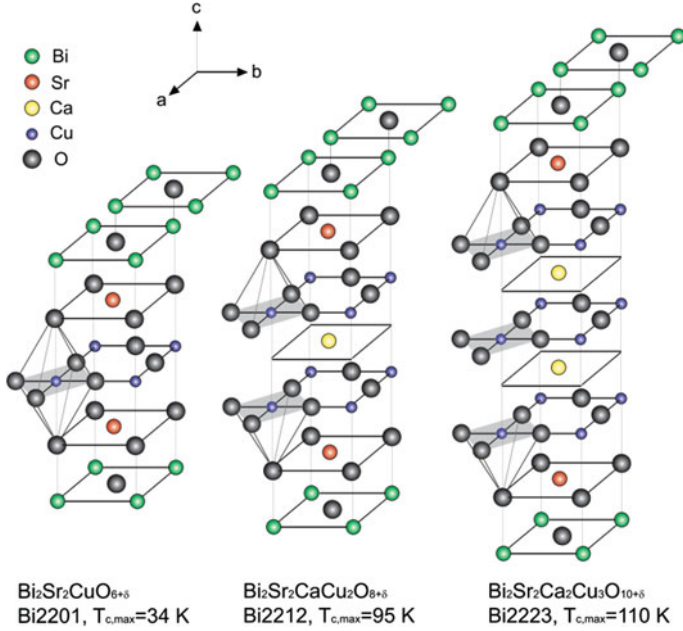


Fig. 1.3 The crystal structure of high T_c cuprate superconductors [16]

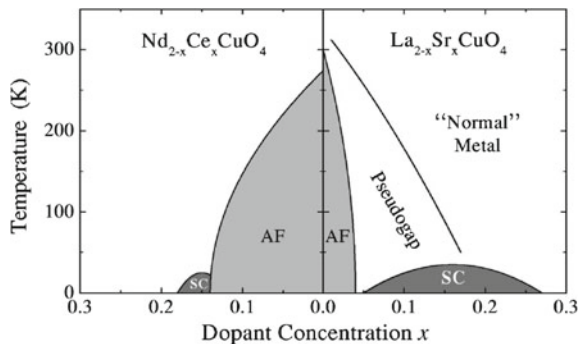
conductivity takes place, and the “charge reservoirs” can be used to tune the carrier density on the “copper oxygen plane.” To the content of this book, the cuprate-related research was performed on $\text{Bi}_2\text{Sr}_2\text{CaCu}_2\text{O}_{8+\delta}$ single crystals. Therefore, the Bi family is taken as an example to show the crystal structures of cuprates. Drawn in Fig. 1.3 are the crystal structures of three typical Bi-related cuprates: $\text{Bi}_2\text{Sr}_2\text{CuO}_{6+\delta}$ (Bi2201), $\text{Bi}_2\text{Sr}_2\text{CaCu}_2\text{O}_{8+\delta}$ (Bi2212), and $\text{Bi}_2\text{Sr}_2\text{Ca}_2\text{Cu}_3\text{O}_{10+\delta}$ (Bi2223). On the one hand, all of them consist of the same Cu-O and Bi-O planes. On the other hand, the number of Cu-O planes in a unit cell is different for these three materials: one, two, and three planes, respectively. It is very interesting that the value of T_c increases with the number of Cu-O planes per unit cell in these materials. Meanwhile, the T_c of a particular material can also be tuned by changing the carrier density. In particular, it can be realized by substituting the elements or changing the oxygen content via annealing. For example, substituting one Ca atom with Dy in Bi2212 dopes one electron into the Cu-O plane which effectively removes one hole. Therefore, underdoped samples with different doping levels can be obtained by controlling the Dy content. On the other hand, if we increase the oxygen content in the sample via annealing, we can effectively increase the number of holes in the Cu-O plane and get overdoped samples.

1.2.2 The Phase Diagram of Cuprates

The phase diagram of cuprates is shown in Fig. 1.4. The parent compound of cuprates is an antiferromagnetic Mott insulator in which the antiferromagnetism is gradually suppressed with doping. Superconductivity eventually appears through an insulator to superconductor transition when the doping level reaches a certain value. Based on the different carriers, the cuprates are divided into two categories: hole-doped and electron-doped samples. The typical phase diagram of hole-doped cuprates (e.g., $\text{La}_{2-x}\text{Sr}_x\text{CuO}_4$) is drawn on the right panel of Fig. 1.4, whereas the left panel shows that of the electron-doped side (e.g., $\text{Nd}_{2-x}\text{Ce}_x\text{CuO}_4$). It is generally believed that the superconductivity only occurs after the antiferromagnetism disappears with doping on the hole-doped side. However, whether superconductivity and antiferromagnetism can coexist on the electron-doped side is still under debate. The transition temperature T_c of cuprates reaches its maximum when the doping level is optimized, and this doping level is called optimal doping. The region between optimal doping and parent compound is regarded as underdoped, whereas the region with doping level higher than optimal doping is called overdoped region. The maximum T_c varies with different cuprate materials. However, the overall doping evolution is similar, consisting of the aforementioned underdoped, optimal doped, and overdoped regions.

Another important part of the phase diagram is the “normal state” which locates right above the superconducting phase. The normal state of the conventional superconductors is Fermi liquid which had provided a very good starting point to establish the theory for superconductivity. In BCS theory, starting from Fermi liquid, people realized that the Fermi surface of the material should become unstable if copper pairs are formed by electron–phonon interaction. Instead, the material enters a superconducting state described by Bogoliubov quasi-particles. However, in hole-doped cuprates, only the “normal state” near the overdoped region behaves normal as Fermi liquid. The “normal state” near the optimally doped region is actually abnormal that the resistance of the copper oxygen plane shows linear temperature dependence at high temperature which is different from that of the Fermi liquid. Therefore, it is called “strange metal.” As for the “normal state” near underdoped region, energy

Fig. 1.4 The phase diagram of high T_c cuprate superconductors. Reprinted with the permission from [17]. Copyright 2003 by the American Physical Society



gap was observed in this state with a temperature higher than the superconducting transition temperature. This energy gap is called pseudogap and has been considered to be very important to superconductivity. However, whether pseudogap works as a “friend” (precursor) to superconductivity or as an “enemy” competing with superconductivity is still under debate. Another important issue is about the closing temperature of the pseudogap: T^* . Whether T^* represents a phase transition has yet to be addressed.

As for the electron-doped cuprates, limited results were obtained comparing to their hole-doped counterparts due to the sample quality and complication in the sample growth. Whether the strange phenomena observed in hole-doped cuprates universal in electron-doped samples is yet to be confirmed. Generally speaking, the electron-doped side of cuprates still shares some resemblances to the hole-doped side on the phase diagram.

1.2.3 The Electronic Structure of Cuprates

In cuprates, the low-energy electronic states (within several eVs below Fermi level) are contributed by the Cu 3d and O 2p electrons. Here, La_2CuO_4 , the parent compound of $\text{La}_{2-x}\text{Sr}_x\text{CuO}_4$ (LSCO), is taken as an example to show the basic electronic structures of the cuprates. As for Cu, 3d electrons are considered in the half-filled parent compound with a total number of 9. Because of the energy splitting by crystal field, 5 energy levels are formed from the e_g and t_{2g} bands, including: XY, YZ, XY, $3Z^2-Y^2$, and X^2-Y^2 orbital as shown in Fig. 1.5. These electronic states are occupied by the 9 electrons. The X^2-Y^2 orbital, which forms the highest energy

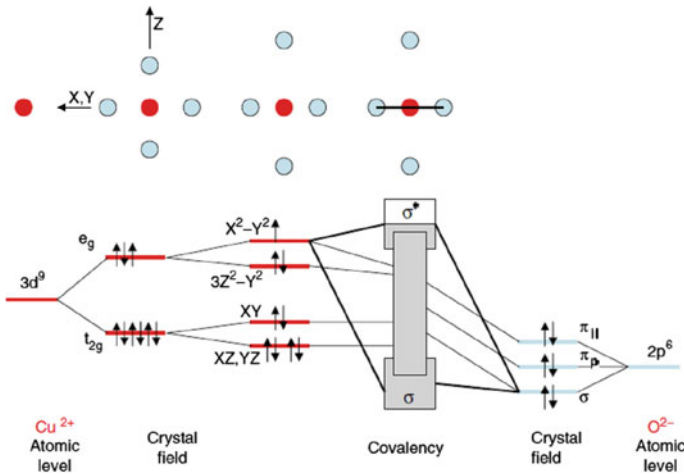


Fig. 1.5 The Cu orbital of cuprates [18]

level, is only half filled with one electron. Therefore, the electronic structures near Fermi level is dominated by the $d_{x^2-y^2}$ electrons. Meanwhile, the O 2p electrons are also hybridized to the Cu 3d electrons due to a similar binding energy. In general, the low electronic structures in cuprates are mainly dictated by the Cu $d_{x^2-y^2}$ and O $2p_x, 2p_y$ orbital [17, 18].

Shown in Fig. 1.6a and b are the LDA results calculated for LSCO. For the half-filled parent compound, it is clear that the antibonding band goes across the Fermi level as shown in Fig. 1.6a and c. In this regard, the parent compound should be a metal. However, as evidenced by many experiments, the parent compound of cuprates is not a metal but an insulator. Therefore, the LDA calculations are not sufficient to describe the cuprate system. In fact, there is strong electron correlation in cuprates that the strong on-site Coulomb repulsion prevents any double occupancy of the electrons on a single site of the lattice. As shown in Fig. 1.6d when Coulomb

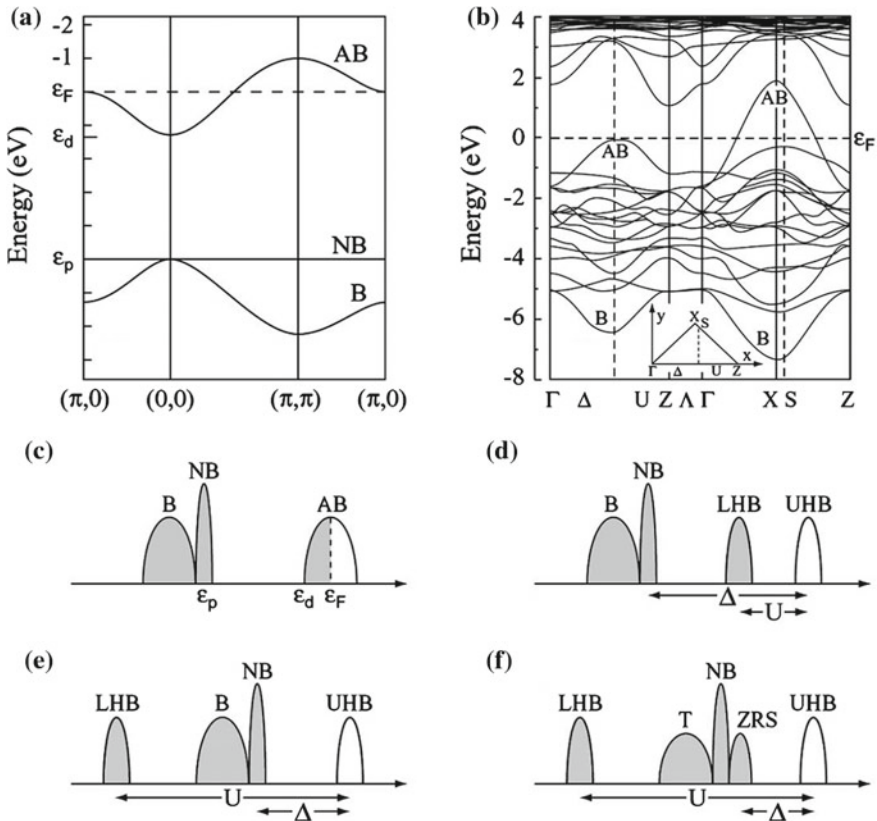


Fig. 1.6 The electronic structure of cuprates. **a** Antibonding band, bonding band, and non-bonding band from LDA. **b** The calculated electronic bands for $\text{La}_2\text{CuO}_{4+\delta}$. **c-e** Electronic states without U and Δ (**c**), $U < \Delta$ (**d**) and $U > \Delta$ (**e**). **f** Zhang-Rice singlet. Reprinted with the permission from [17]. Copyright 2003 by the American Physical Society

repulsion U is larger than the band width W , the antibonding band splits into two bands: upper Hubbard band and lower Hubbard band, which gives rise to a Mott insulator. If the on-site Coulomb repulsion is extremely strong and U is larger than the energy difference between the non-bonding band and the antibonding band Δ , then the energy gap near Fermi level is not a Mott gap but a charge transfer gap as shown in Fig. 1.6e, and this is the case for cuprates. Since the antibonding band, bonding band, and non-bonding band are all involved in the electronic structures near Fermi level, it is necessary to consider the three-band model which contains the Cu $d_{x^2-y^2}$ and O $2p_x, 2p_y$ orbital. However, more complexities were induced by this three-band model [17]. Later, Zhang and Rice proposed a simplified version in which one Cu atom and the O atoms surrounded are considered together as a singlet, called “Zhang–Rice singlet” [19]. Then a one-band model based on “Zhang–Rice singlet” can be used to describe cuprates, as shown in Fig. 1.6f.

1.2.4 The Theoretical Models of Cuprates

In the past more than twenty years, many theoretical models were proposed for cuprates. However, none of them has been well accepted by the community till now. These models can be divided into two types: The first type of models does not break the crystal symmetry, whereas the second one breaks it. One of the earliest models among the first type is the band calculations based on Fermi liquid theory [20, 21]. In this model, with carrier doping, the screening effect is strong enough to soften the strong electron correlation in the parent compound such that the Fermi liquid picture becomes valid again. The Fermi surface calculated by this model is shown in Fig. 1.7a. Another theory, in which the crystal symmetry is kept, considers the umklapp scattering [22–24] and predicts a Fermi surface as shown in Fig. 1.7b. Among the theories which break the crystal symmetry, the most famous one is probably the RVB theory [17, 25, 26]. Fermi pockets are predicted (Fig. 1.7c) by this theory. Shown in Fig. 1.7d is a nearly rectangle Fermi surface given by another theory based on stripe model, which also breaks the crystal symmetry.

The theoretical models of the cuprates can also be separated by considering whether a pairing glue is needed. As is known to all, electron–phonon coupling works as a glue for the electron pairing in the conventional superconductors. However, whether a pairing glue is necessary in cuprates becomes a critical question under hot debate. For example, in the aforementioned RVB theory, a glue is not needed. The electrons are considered to be paired in the parent compound, and carrier doping simply provides a path for the paired electrons to move in the material which naturally leads to superconductivity. Meanwhile, the pairing glue is still considered to be essential in many other theories, and the key issue to be unveiled in these theories is the origin of the glue. One of the popular candidates is spin fluctuation [28]. Another promising candidate is the loop current proposed by Chandra Varma et al. [29]. Of course, phonon has also been discussed as the glue in cuprates by some researchers.

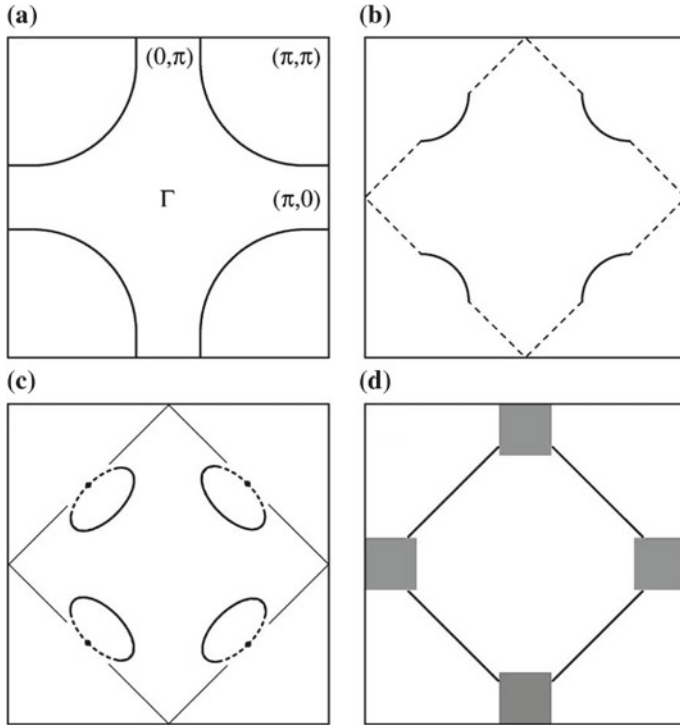
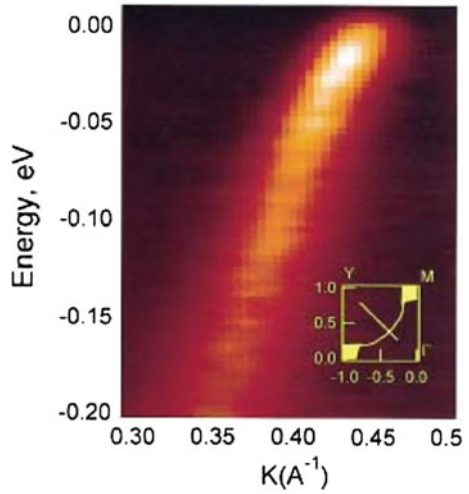


Fig. 1.7 Fermi surfaces from different theoretical models for high T_c cuprate superconductors. Reprinted with the permission from [17]. Copyright 2003 by the American Physical Society

Fig. 1.8 The observation of nodal kink. Reprinted with the permission from [27]. Copyright 2000 by the American Physical Society



1.2.5 Many-Body Effects in Cuprates

It is believed that the electron–boson interaction which might mediate the electron pairing should manifest themselves as some energy structures in the electronic bands of the materials. Therefore, exploring the many-body effects in the band structure of cuprates may provide the key information for the electron pairing which is believed to be essential for realizing superconductivity.

Among the studies of the many-body effects in cuprates, the most prominent ones are probably the observation of nodal and antinodal kinks [27, 30–38]. Shown in Fig. 1.8 is the dispersion kink at an energy of ~ 70 meV first observed along the nodal direction (diagonal of the Brillouin zone) of the Bi2212 sample [27, 30, 32–35]. Later, this nodal kink was broadly observed in different cuprate families with different doping levels (Fig. 1.9) which generated great interests in the research community.

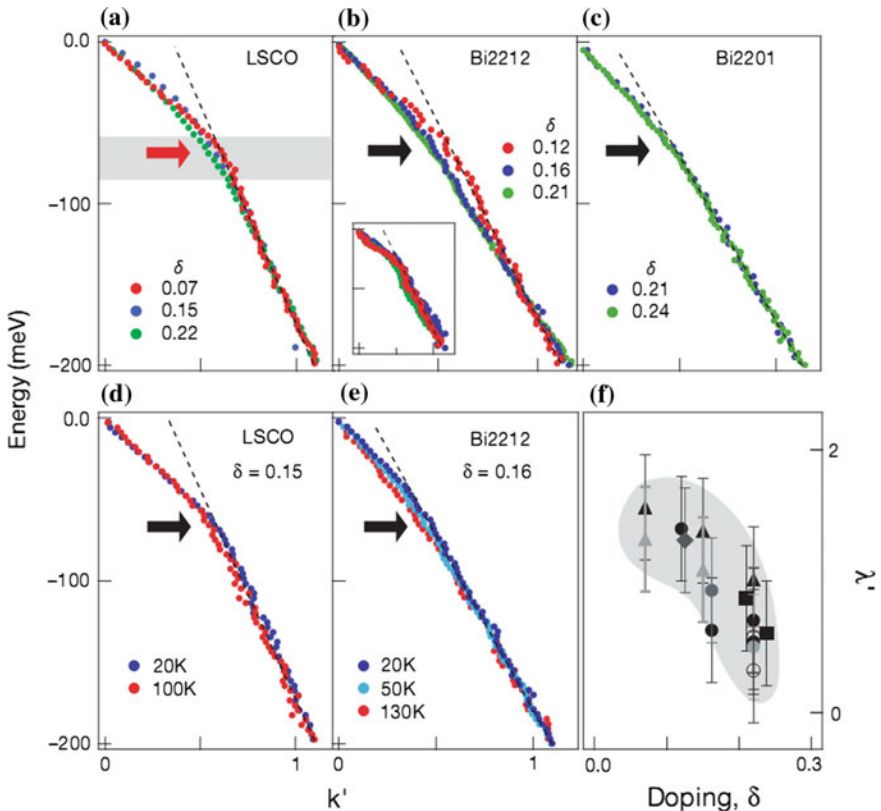


Fig. 1.9 The observation of nodal kink in various cuprates: **a** LSCO with different doping levels. **b** Bi2212 with different doping levels. **c** Bi2201 with different doping levels. Kink is observed both above and below T_c in LSCO (**d**) and Bi2212 (**e**). **f** The coupling strength changes with doping. Reprinted with the permission from Macmillan Publishers Ltd: [30], copyright 2001

As for the origin of the nodal kink, two different explanations were proposed. The first one is the electron coupling to collective magnetic excitations since a resonant mode with the similar energy scale was observed by neutron scattering [32, 33]. Another possibility is the electron-phonon coupling [30]. The major experimental results supporting this scenario come from the facts that the nodal kink was observed above T_c and in heavily overdoped samples where the resonant mode disappears.

The existence of antinodal kink (Fig. 1.10) [31, 36–38] is another important observation besides the nodal kink. Different from the nodal kink, the antinodal kink only appears in the superconducting state with an energy scale of ~ 40 meV. Again, both collective magnetic excitation and phonon have been proposed as the candidate responsible for the electron–boson coupling.

While the existence of nodal and antinodal kinks has been well established by many experiments, the relationship between them is a long-standing puzzle. In particular, how does the ~ 70 meV nodal kink evolve into the ~ 40 meV antinodal kink when the momentum gradually moves from the nodal to the antinodal regions? Do they share a common origin? By carrying out super-high-resolution measurements with the state-of-the-art laser-based angle-resolved photoemission spectroscopy, the

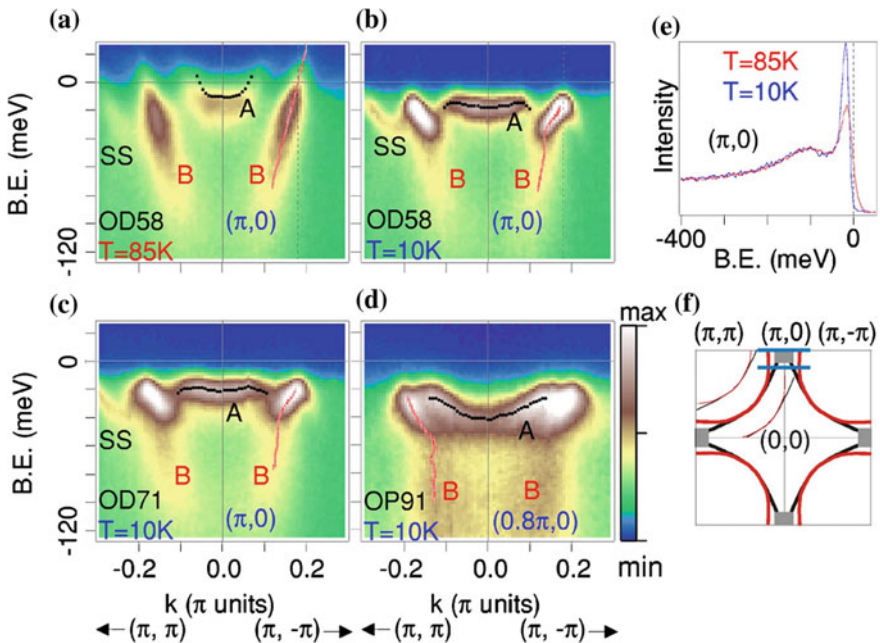


Fig. 1.10 The observation of antinodal kink. In the overdoped 58 K sample, the antinodal kink disappears above T_c (a measured at 85 K) but appears below T_c (b measured at 10 K). The kink is also observed in the overdoped 71 K sample (c) and optimally doped 91 K sample (d) at 10 K. e EDC at the $(\pi, 0)$. f The momentum locations of the cuts. Reprinted with the permission from [31]. Copyright 2003 by the American Physical Society

coexistence of two energy scales in a large area of momentum space was observed for the first time by the author and collaborators. One of the energy scales is observed over the momentum space from nodal to antinodal region with a fix energy of ~ 78 meV, whereas the other one evolves from the nodal to antinodal region with its energy varying from ~ 70 to ~ 40 meV. Different temperature dependence was also observed for these two energy scales. These observations have experimentally established the relationship between the nodal and antinodal kinks. Details are presented in the corresponding chapter.

1.3 Iron-Based Superconductors

1.3.1 The Crystal Structure of Iron-Based Superconductors

Shown in Fig. 1.11 are the typical crystal structures of several different iron-based superconductor systems: “11” [40], “111” [41], “122” [42], “1111” [10–13] and

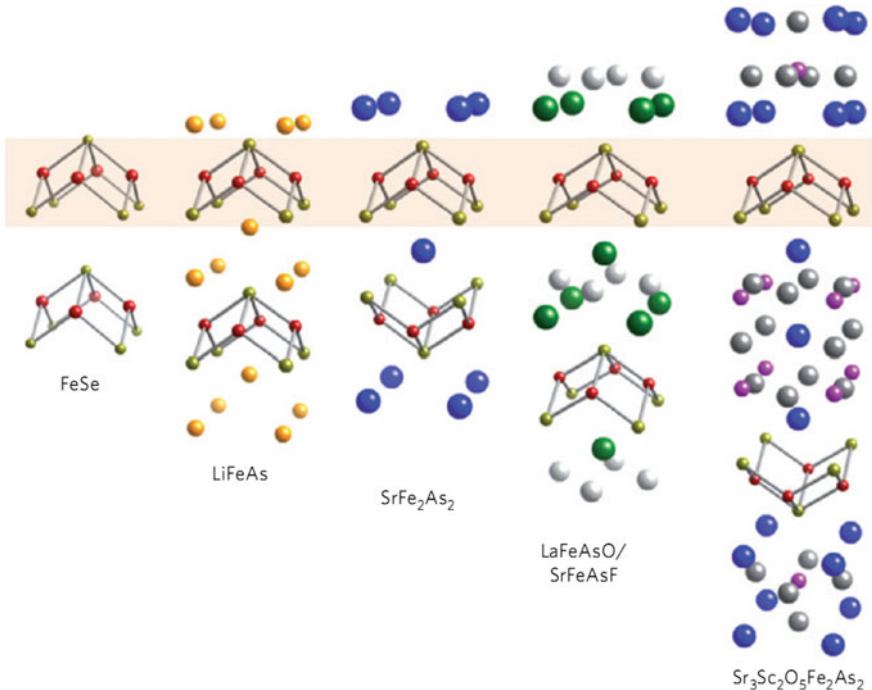


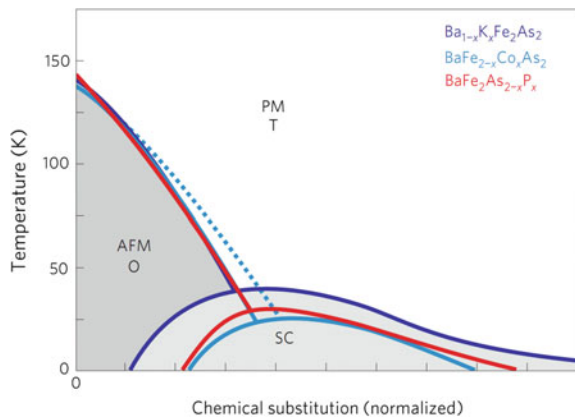
Fig. 1.11 The crystal structure of various iron-based superconductors. Reprinted with the permission from Macmillan Publishers Ltd: [39], copyright 2010

“32522” [43]. Although many new materials with more complicated chemical compositions are still coming out, a common crystal structure can be recognized in all the iron-based superconductors: the so-called FeAs layer or FeSe layer. People believe these FeAs (FeSe) layers are responsible for the superconductivity, similar to the case of Cu-O layers in cuprates. Different iron-based superconductors have different FeAs (FeSe) layers in its unit cell, and it seems that higher T_c can be found in materials with more FeAs (FeSe) layers. However, different from the Cu-O plane, the Fe and As (Se) atoms of the FeAs (FeSe) layer are not in the same plane which gives the iron-based superconductors a stronger three-dimensionality than the cuprates.

1.3.2 The Phase Diagram of Iron-Based Superconductors

Figure 1.12 shows the typical phase diagram of BaFe_2As_2 . Similar to the case in cuprates, superconductivity appears when antiferromagnetism is suppressed with doping in iron-based superconductors, which indicates the possible relationship between the superconductivity and the antiferromagnetism. However, there are also differences between the phase diagram of cuprates and iron-based superconductors. Pseudogap is well established in cuprates, but its existence in iron-based superconductors is still under debate. Although arguable evidences for pseudogap were found in “11” system, no pseudogap was reported in “122” system. Another intriguing point is the possible coexistence of antiferromagnetism and superconductivity in iron-based superconductors, which is different from the hole-doped cuprates but similar to the electron-doped compounds. Moreover, there are structural and magnetic transitions with temperature in the parent compound of iron-based superconductors.

Fig. 1.12 A typical phase diagram of BaFe_2As_2 . Reprinted with the permission from Macmillan Publishers Ltd: [39], copyright 2010



For example, a structural transition from a tetragonal to an orthorhombic phase may take place [44].

1.3.3 The Electronic Structures of Iron-Based Superconductors

In iron-based superconductors, the Fe 3d electrons are mainly responsible for the superconducting process. As for the 6 electrons around Fe^{2+} , the 3d states are split into e_g and t_{2g} orbital states by the crystal field. Different from the orbital states in cuprate, the e_g orbital state has the lowest energy in iron-based superconductors. Meanwhile, Hund's rule coupling also plays an important role, which favors the electrons on the same site of the lattice showing the same spin polarization. Therefore, when the Hund's coupling is stronger than the splitting by the crystal field, the five energy levels of the e_g and t_{2g} orbital states are first filled by the electrons with the same spin polarization. Then the last 3d electron with different spin polarization occupies the lowest energy level of the e_g states. Finally, there are three electrons in e_g and t_{2g} orbital states, respectively, with a total magnetic moment $S = 2$. However, if the Hund's coupling is not as strong as the crystal field splitting, then electrons start to occupy the states from low energy to high energy with each energy level filled by two electrons. In this case, the e_g orbital states are occupied by 4 electrons, whereas the t_{2g} states hold two electrons, which gives a magnetic moment $S = 1$ [45]. Generally speaking, in iron-based superconductors, multiband models are needed to describe the low-energy electronic structures near Fermi level, which is different from the single-band model in cuprate and adds complications in understanding this system.

1.3.4 The Magnetic Structures of Iron-Based Superconductors

Magnetic order is widely observed in the parent compound of iron-based superconductors. However, different magnetic structures exist in different materials. As for the FeAs "11," "111," and "122" compounds, along the direction of the magnetic moments, neighboring sites show opposite signs, which looks like antiferromagnetism. However, the magnetic moment keeps the same sign along the direction perpendicular to itself, which looks like ferromagnetism. This magnetic structure is called "collinear" antiferromagnetism, as shown in Fig. 1.13a. The corresponding wave vector is $(1/2, 1/2)$. As for the FeSe "11" family, the magnetic moment is along the crystal lattice, exhibiting a "bi-collinear" antiferromagnetic order with a wave vector of $(1/2, 0)$, as shown in Fig. 1.13b [46].

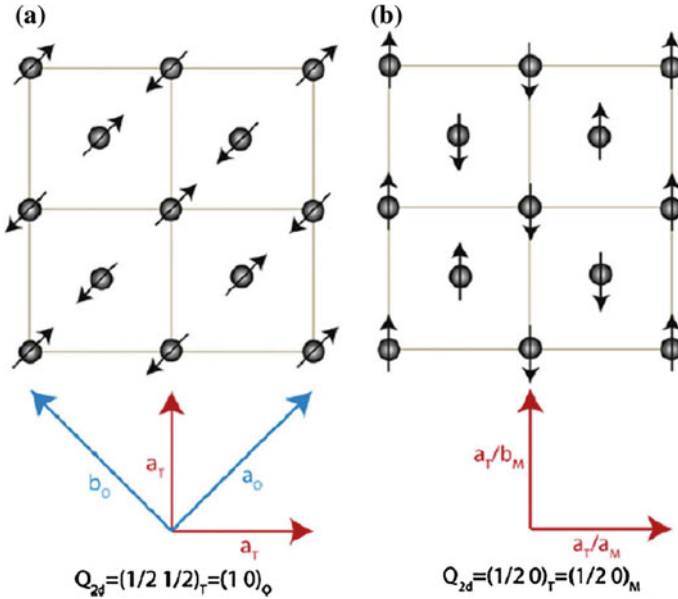


Fig. 1.13 The magnetic structures of iron-based superconductors. **a** “Collinear” antiferromagnetism. **b** “Bi-collinear” antiferromagnetism. IOP Publishing. Reproduced with the permission from [46]. All rights reserved

1.3.5 The Theoretical Models for Iron-Based Superconductors

Many theoretical models have been proposed after the discovery of iron-based superconductors. The central issue under debate is about the starting point: either from an itinerant picture or a localized picture. The most popular theory based on the itinerant picture is probably the “Fermi surface nesting” [47–49]. In the parent compound of some iron-based superconductors, hole pockets were observed centering at Γ point of the Fermi surface, whereas electron pockets with the shape and size similar to those of the hole pockets were found at M point. The nesting between these Fermi pockets enhances the electron scattering between them, which induces spin density wave (SDW) to the system. With carrier doping, the relative size of the Fermi pockets at Γ and M changes, which weakens the nesting condition and suppresses the SDW. Meanwhile, the remanent spin fluctuation works well as a pairing glue for superconductivity, which explains the emergence of superconductivity with doping. In the overdoped region, the spin fluctuation disappears, so the superconductivity vanishes due to the lack of pairing glue. The doping evolution of the phase diagram is shown in Fig. 1.14. In the first few years after the observation of FeAs-based compounds, this itinerant picture was very popular because most of the FeAs-based parent compounds are antiferromagnetic bad metals, and the “Fermi surface nesting” explained

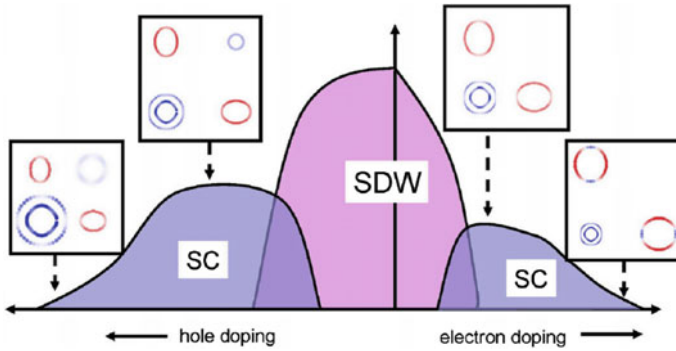


Fig. 1.14 Fermi surface nesting versus doping. IOP Publishing. Reproduced with the permission from [59]. All rights reserved

many experimental results. However, this scenario was seriously challenged by the successful synthesis of $A_x\text{Fe}_{2-y}\text{Se}_2$ ($A = \text{K}, \text{Cs}, \text{Rb}, \text{Tl}$) superconductors [50–52] and the related ARPES results [53–56]. First, the parent compound of $A_x\text{Fe}_{2-y}\text{Se}_2$ ($A = \text{K}, \text{Cs}, \text{Rb}, \text{Tl}$) is probably an insulator which makes people worry about the validity of the itinerant picture. Second, no hole pocket was observed at Γ point which invalidates the aforementioned nesting picture. Although electron pockets are still observed at both Γ and M points [55, 56], the possible nesting wave vector is not consistent with the magnetic wave vector in this material. Therefore, “Fermi surface nesting” cannot give a reasonable explanation to describe the $A_x\text{Fe}_{2-y}\text{Se}_2$ ($A = \text{K}, \text{Cs}, \text{Rb}, \text{Tl}$) system. If one can still claim the complications from three dimensions (3D) of the material and the existence of electron pockets at Γ point, the recent experimental results from the single-layer FeSe films grown on SrTiO_3 substrate showed no consistency with the “Fermi surface nesting” at all. First, the single-layer films are pure 2D which is free from the 3D complications. Second, there is no Fermi surface near Γ point. Third, the parent compound of the single-layer FeSe films is very likely to be an insulator. These new experimental results remind people to reconsider the general validity of the itinerant picture.

The other scenario is based on the localized picture. In the localized picture, electrons in iron-based superconductors are not considered to be itinerant, but strongly correlated as the ones in cuprates. By using slave-spin approach, Si et al. suggested that the Mott transition may take place when the parent compound of the iron-based superconductors is doped with carriers [57]. The localized models can directly explain the insulator to superconductor transition as well as the antiferromagnetism in the parent compound. However, the calculated magnetic moment cannot reach a quantitative agreement with the experiments. Of course, explanations have also been given by considering the competition between the nearest neighboring and second nearest neighboring exchange interactions [58].

Generally speaking, the electron correlation in iron-based superconductors is not as strong as that in cuprates. However, the simple itinerant picture cannot fully explain the experimental results either. Nevertheless, there are only several years

since the first observation of the iron-based superconductors. More materials will be explored and the mechanism of the superconductivity will also be unveiled with more experimental observations and theoretical efforts.

In this book, the research on the electronic structure of the single-layer FeSe films grown on SrTiO₃ substrate will be presented. Great interests have been generated by the possible existence of high transition temperature (T_c) in these single-layer films. First, the T_c in single-layer FeSe film may break the current record in iron-based superconductors. Second, the T_c in bulk FeSe is only ~ 8 K although it can be enhanced to 36.7 K under high pressure. However, a much higher T_c was observed in the single-layer FeSe film. Third, the single-layer FeSe film represents an ideal platform to study the mechanism of the high-temperature superconductivity. On one hand, it has the simplest crystal structure consisting only a single FeSe layer which is the building block of the iron-based superconductors. The 2D character of the film as well as its simple electronic structure can give direct evidence to the superconducting mechanism. On the other hand, the interface between the single-layer FeSe and SrTiO₃ substrate plays an important role which gives us a unique opportunity to study the interface-induced high-temperature superconductivity.

Firstly, by performing high-resolution angle-resolved photoemission on the single-layer FeSe films grown on SrTiO₃ substrate, we found a simple Fermi surface with only electron pocket(s) around M point but no Fermi surface near Γ point. Then, a nearly isotropic energy gap without any node was identified in the superconducting state by measuring along the underlying Fermi surface. Because of the pure 2D character which rules out the complication from k_z , a solid conclusion can be drawn: There is no gap node in this system.

Doping-dependent measurements have been successfully carried out by annealing the as-grown films in vacuum. To keep track of the evolution, the annealing process was divided into many small steps, after each step ARPES measurements were carried out. Two different but competing phases (N phase and S phase) have been clearly identified. The N phase which was observed at the early stage of the annealing process (possibly with low doping level) shares some similarities with the parent compound of Ba122 system in the magnetic state. This “magnetic-like” N phase was then suppressed with annealing after which the superconducting phase was finally observed with sufficient electron doping. By optimizing the doping level, electronic indication of superconductivity with a T_c of ~ 65 K was identified.

Meanwhile, we notice that the single-layer FeSe film with low doping level is insulating which becomes superconducting with sufficient electron doping. Therefore, it works as an ideal case to study the insulator to superconductor crossover in iron-based superconductors. Based on the experimental observations, we notice that the insulator to superconductor crossover and the emergence of S phase do not take place at the same time. There is a large insulating gap in the S phase with low electron doping. The spectral weight starts to appear near the Fermi level with electron doping, which finally leads to the insulator to superconductor crossover. The overall doping evolution is very similar to that observed in hole-doped cuprates, which indicates that the strong electron correlations play an important role in the single-layer FeSe films. The details will be presented in the corresponding chapters.

References

1. Onnes, H.K.: Disappearance of the electrical resistance of mercury at helium temperatures. In: Proceedings Koninklijke Akademie van Wetenschappen te Amsterdam, pp. 113–115 (1911)
2. Meissner, W., Ochsenfeld, R.: Ein neuer Effekt bei Eintritt der Supraleitfähigkeit. *Naturwissenschaften* **21**, 787 (1933)
3. Bardeen, J., Cooper, L.N., Schrieffer, J.R.: Theory of superconductivity. *Phys. Rev.* **108**, 1175–1204 (1957)
4. Bednorz, J.G., Müller, K.A.: Possible high- T_c superconductivity in the Ba-La-Cu-O system. *Z. Phys. B Condens. Matter* **64**(2), 189–193 (1986)
5. Wu, M.K., Ashburn, J.R., Torng, C.J., Hor, P.H., Meng, R.L., Gao, L., Huang, Z.J., Wang, Y.Q., Chu, C.W.: Superconductivity at 93 K in a new mixed-phase Y-Ba-Cu-O compound system at ambient pressure. *Phys. Rev. Lett.* **58**, 908–910 (1987)
6. Zhao, Z.X.: Superconductivity with critical temperature greater than the boiling point of liquid nitrogen in Ba-Y-Cu. *Chin. Sci. Bull.* **32**, 412 (1987)
7. Schilling, A., Cantoni, M., Guo, J.D., Ott, H.R.: Superconductivity above 130 K in the Hg-Ba-Ca-Cu-O system. *Nature* **363**(6424), 56–58 (1993)
8. Gao, L., Xue, Y.Y., Chen, F., Xiong, Q., Meng, R.L., Ramirez, D., Chu, C.W., Eggert, J.H., Mao, H.K.: Superconductivity up to 164 K in $\text{HgBa}_2\text{Ca}_{m-1}\text{Cu}_m\text{O}_{2m+2+\delta}$ ($m = 1, 2, \text{ and } 3$) under quasihydrostatic pressures. *Phys. Rev. B* **50**, 4260–4263 (1994)
9. Keimer, B., Kivelson, S.A., Norman, M.R., Uchida, S., Zaanen, J.: From quantum matter to high-temperature superconductivity in copper oxides. *Nature* **518**(7538), 179–186 (2015)
10. Kamihara, Y., Watanabe, T., Hirano, M., Hosono, H.: Iron-based layered superconductor $\text{LaO}_{1-x}\text{F}_x\text{FeAs}$ ($x = 0.05 - 0.12$) with $T_c = 26$ K. *J. Am. Chem. Soc.* **130**(11), 3296–3297 (2008)
11. Chen, X.H., Wu, T., Wu, G., Liu, R.H., Chen, H., Fang, D.F.: Superconductivity at 43 K in $\text{SmFeAsO}_{1-x}\text{F}_x$. *Nature* **453**(7196), 761–762 (2008)
12. Chen, G.F., Li, Z., Wu, D., Li, G., Hu, W.Z., Dong, J., Zheng, P., Luo, J.L., Wang, N.L.: Superconductivity at 41 K and its competition with spin-density-wave instability in layered $\text{CeO}_{1-x}\text{F}_x\text{FeAs}$. *Phys. Rev. Lett.* **100**(24), 247002 (2008)
13. Ren, Z.-A., Yang, J., Lu, W., Yi, W., Shen, X.-L., Li, Z.-C., Che, G.-C., Dong, X.-L., Sun, L.-L., Zhou, F., Zhao, Z.-X.: Superconductivity in the iron-based F-doped layered quaternary compound $\text{NdO}_{1-x}\text{F}_x\text{FeAs}$. *Europhys. Lett.* **82**(5), 57002 (2008)
14. Wang, C., Li, L., Chi, S., Zhu, Z., Ren, Z., Li, Y., Wang, Y., Lin, X., Luo, Y., Jiang, S., Xu, X., Cao, G., Xu, Z.: Thorium-doping-induced superconductivity up to 56 K in $\text{Gd}_{1-x}\text{Th}_x\text{FeAsO}$. *Europhys. Lett.* **83**(6), 67006 (2008)
15. He, S., He, J., Zhang, W., Zhao, L., Liu, D., Liu, X., Mou, D., Ou, Y., Wang, Q., Li, Z., Wang, L., Peng, Y., Liu, Y., Chen, C., Yu, L., Liu, G., Dong, X., Zhang, J., Chen, C., Xu, Z., Chen, X., Ma, X., Xue, Q., Zhou, X.J.: Phase diagram and electronic indication of high-temperature superconductivity at 65 K in single-layer FeSe films. *Nat. Mater.* **12**(7), 605–610 (2013)
16. Tanaka, K.: Photoemission study of Bi-cuprate high- T_c superconductors in the lightly-doped to underdoped regions. Ph.D. thesis. University of Tokyo (2004)
17. Damascelli, A., Hussain, Z., Shen, Z.-X.: Angle-resolved photoemission studies of the cuprate superconductors. *Rev. Mod. Phys.* **75**, 473–541 (2003)
18. Fink, J., Nucker, N., Romberg, H.A., Fuggle, J.C.: Electronic structure studies of high- T_c superconductors by high-energy spectroscopies. *IBM J. Res. Dev.* **33**(3), 372–381 (1989)
19. Zhang, F.C., Rice, T.M.: Effective Hamiltonian for the superconducting Cu oxides. *Phys. Rev. B* **37**(7), 3759–3761(R) (1988)
20. Pines, D., Nozières, P.: *The Theory of Quantum Liquids*, vol. 1. Benjamin, New York (1966)
21. Pickett, W.E.: Electronic structure of the high-temperature oxide superconductors. *Rev. Mod. Phys.* **61**(2), 433–512 (1989)
22. Furukawa, N., Rice, T.M.: Instability of a Landau-Fermi liquid as the Mott insulator is approached. *J. Phys.: Condens. Matter* **10**(23), L381 (1998)

23. Furukawa, N., Rice, T.M., Salmhofer, M.: Truncation of a two-dimensional Fermi surface due to quasiparticle gap formation at the saddle points. *Phys. Rev. Lett.* **81**(15), 3195 (1998)
24. Honerkamp, C., Salmhofer, M., Furukawa, N., Rice, T.M.: Breakdown of the Landau-Fermi liquid in two dimensions due to umklapp scattering. *Phys. Rev. B* **63**(3), 035109 (2001)
25. Wen, X.G., Lee, P.A.: Theory of underdoped cuprates. *Phys. Rev. Lett.* **76**(3), 503 (1996)
26. Lee, P.A., Nagaosa, N., Wen, X.G.: Doping a Mott insulator: physics of high-temperature superconductivity. *Rev. Mod. Phys.* **78**(1), 17–85 (2006)
27. Bogdanov, P.V., Lanzara, A., Kellar, S.A., Zhou, X.J., Lu, E.D., Zheng, W.J., Gu, G., Shimoyama, J.-I., Kishio, K., Ikeda, H., Yoshizaki, R., Hussain, Z., Shen, Z.-X.: Evidence for an energy scale for quasiparticle dispersion in $\text{Bi}_2\text{Sr}_2\text{CaCu}_2\text{O}_8$. *Phys. Rev. Lett.* **85**, 2581–2584 (2000)
28. Scalapino, D.J., Loh Jr., E., Hirsch, J.E.: D-wave pairing near a spin-density-wave instability. *Phys. Rev. B* **34**(11), 8190–8192 (1986)
29. Varma, C.M.: Non-Fermi-liquid states and pairing instability of a general model of copper oxide metals. *Phys. Rev. B* **55**(21), 14554–14580 (1997)
30. Lanzara, A., Bogdanov, P.V., Zhou, X.J., Kellar, S.A., Feng, D.L., Lu, E.D., Yoshida, T., Eisaki, H., Fujimori, A., Kishio, K., Shimoyama, J.-I., Noda, T., Uchida, S., Hussain, Z., Shen, Z.-X.: Evidence for ubiquitous strong electron-phonon coupling in high-temperature superconductors. *Nature (London)* **412**(6846), 510–514 (2001)
31. Gromko, A.D., Fedorov, A.V., Chuang, Y.-D., Koralek, J.D., Aiura, Y., Yamaguchi, Y., Oka, K., Ando, Y., Dessau, D.S.: Mass-renormalized electronic excitations at $(\pi, 0)$ in the superconducting state of $\text{Bi}_2\text{Sr}_2\text{CaCu}_2\text{O}_{8+\delta}$. *Phys. Rev. B* **68**, 174520 (2003)
32. Johnson, P.D., Valla, T., Fedorov, A.V., Yusof, Z., Wells, B.O., Li, Q., Moodenbaugh, A.R., Gu, G.D., Koshizuka, N., Kendziora, C., Jian, S., Hinks, D.G.: Doping and temperature dependence of the mass enhancement observed in the cuprate $\text{Bi}_2\text{Sr}_2\text{CaCu}_2\text{O}_{8+\delta}$. *Phys. Rev. Lett.* **87**, 177007 (2001)
33. Kaminski, A., Randeria, M., Campuzano, J.C., Norman, M.R., Fretwell, H., Mesot, J., Sato, T., Takahashi, T., Kadowaki, K.: Renormalization of spectral line shape and dispersion below T_c in $\text{Bi}_2\text{Sr}_2\text{CaCu}_2\text{O}_{8+\delta}$. *Phys. Rev. Lett.* **86**, 1070–1073 (2001)
34. Zhou, X.J., Yoshida, T., Lanzara, A., Bogdanov, P.V., Kellar, S.A., Shen, K.M., Yang, W.L., Ronning, F., Sasagawa, T., Kakeshita, T., Noda, T., Eisaki, H., Uchida, S., Lin, C.T., Zhou, F., Xiong, J.W., Ti, W.X., Zhao, Z.X., Fujimori, A., Hussain, Z., Shen, Z.-X.: High-temperature superconductors: universal nodal Fermi velocity. *Nature (London)* **423**(6938), 398 (2003)
35. Kordyuk, A.A., Borisenko, S.V., Zabolotnyy, V.B., Geck, J., Knupfer, M., Fink, J., Bchner, B., Lin, C.T., Keimer, B., Berger, H., Pan, A.V., Komiya, S., Ando, Y.: Constituents of the quasiparticle spectrum along the nodal direction of high- T_c cuprates. *Phys. Rev. Lett.* **97**, 017002 (2006)
36. Kim, T.K., Kordyuk, A.A., Borisenko, S.V., Koitzsch, A., Knupfer, M., Berger, H., Fink, J.: Doping dependence of the mass enhancement in $(\text{Pb}, \text{Bi})_2\text{Sr}_2\text{CaCu}_2\text{O}_8$ at the antinodal point in the superconducting and normal states. *Phys. Rev. Lett.* **91**, 167002 (2003)
37. Sato, T., Matsui, H., Takahashi, T., Ding, H., Yang, H.B., Wang, S.C., Fujii, T., Watanabe, T., Matsuda, A., Terashima, T., Kadowaki, K.: Observation of band renormalization effects in hole-doped high- T_c superconductors. *Phys. Rev. Lett.* **91**(15), 157003 (2003)
38. Cuk, T., Baumberg, F., Lu, D.H., Ingle, N., Zhou, X.J., Eisaki, H., Kaneko, N., Hussain, Z., Devereaux, T.P., Nagaosa, N., Shen, Z.-X.: Coupling of the $b1g$ phonon to the antinodal electronic states of $\text{Bi}_2\text{Sr}_2\text{Ca}_{0.92}\text{Y}_{0.08}\text{Cu}_2\text{O}_{8+\delta}$. *Phys. Rev. Lett.* **93**, 117003 (2004)
39. Paglione, J., Greene, R.L.: High-temperature superconductivity in iron-based materials. *Nat. Phys.* **6**(9), 645–658 (2010)
40. Hsu, F.C., Luo, J.Y., Yeh, K.W., Chen, T.K., Huang, T.W., Wu, P.M., Lee, Y.C., Huang, Y.L., Chu, Y.Y., Yan, D.C., Wu, M.K.: Superconductivity in the PbO -type structure α - FeSe . *Proc. Natl. Acad. Sci. USA* **105**(38), 14262–14264 (2008)
41. Wang, X.C., Liu, Q.Q., Lv, Y.X., Gao, W.B., Yang, L.X., Yu, R.C., Li, F.Y., Jin, C.Q.: The superconductivity at 18 K in LiFeAs system. *Solid State Commun.* **148**(11), 538–540 (2008)

42. Rotter, M., Tegel, M., Johrendt, D.: Superconductivity at 38 K in the iron arsenide $(\text{Ba}_{1-x}\text{K}_x)\text{Fe}_2\text{As}_2$. *Phys. Rev. Lett.* **101**(10), 107006 (2008)
43. Shirage, P.M., Kihou, K., Lee, C.H., Kito, H., Eisaki, H., Iyo, A.: Emergence of superconductivity in “32522” structure of $(\text{Ca}_3\text{Al}_2\text{O}_{5-y})(\text{Fe}_2\text{Pn}_2)(\text{Pn} = \text{As and P})$. *J. Am. Chem. Soc.* **133**(25), 9630–9633 (2011)
44. McQueen, T.M., Williams, A.J., Stephens, P.W., Tao, J., Zhu, Y., Ksenofontov, V., Casper, F., Felser, C., Cava, R.J.: Tetragonal-to-orthorhombic structural phase transition at 90 K in the superconductor $\text{Fe}_{1.01}\text{Se}$. *Phys. Rev. Lett.* **103**(5), 057002 (2009)
45. Singh, D.J., Du, M.H.: Density functional study of $\text{LaFeAsO}_{1-x}\text{F}_x$: a low carrier density superconductor near itinerant magnetism. *Phys. Rev. Lett.* **100**(23), 237003 (2008)
46. Lumsden, M.D., Christianson, A.D.: Magnetism in Fe-based superconductors. *J. Phys.: Condens. Matter* **22**(20), 203203 (2010)
47. Mazin, I.I., Singh, D.J., Johannes, M.D., Du, M.H.: Unconventional superconductivity with a sign reversal in the order parameter of $\text{LaFeAsO}_{1-x}\text{F}_x$. *Phys. Rev. Lett.* **101**(5), 057003 (2008)
48. Mazin, I.I., Johannes, M.D.: A key role for unusual spin dynamics in ferropnictides. *Nat. Phys.* **5**(2), 141–145 (2009)
49. Wang, F., Zhai, H., Lee, D.H.: Antiferromagnetic correlation and the pairing mechanism of the cuprates and iron pnictides: a view from the functional renormalization group studies. *Europhys. Lett.* **85**(3), 37005 (2009)
50. Guo, J., Jin, S., Wang, G., Wang, S., Zhu, K., Zhou, T., He, M., Chen, X.: Superconductivity in the iron selenide $\text{K}_x\text{Fe}_2\text{Se}_2$ ($0 \leq x \leq 1.0$). *Phys. Rev. B* **82**(18), 180520(R) (2010)
51. Li, C.H., Shen, B., Han, F., Zhu, X., Wen, H.H.: Transport properties and anisotropy of $\text{Rb}_{1-x}\text{Fe}_{2-y}\text{Se}_2$ single crystals. *Phys. Rev. B* **83**(18), 184521 (2011)
52. Fang, M.H., Wang, H.D., Dong, C.H., Li, Z.J., Feng, C.M., Chen, J., Yuan, H.Q.: Fe-based superconductivity with $T_c = 31$ K bordering an antiferromagnetic insulator in $(\text{Tl}, \text{K})\text{Fe}_x\text{Se}_2$. *Europhys. Lett.* **94**(2), 27009 (2011)
53. Zhang, Y., Yang, L.X., Xu, M., Ye, Z.R., Chen, F., He, C., Xu, H.C., Jiang, J., Xie, B.P., Ying, J.J., Wang, X.F., Chen, X.H., Hu, J.P., Matsunami, M., Kimura, S., Feng, D.L.: Nodeless superconducting gap in $\text{A}_x\text{Fe}_2\text{Se}_2$ ($\text{A} = \text{K}, \text{Cs}$) revealed by angle-resolved photoemission spectroscopy. *Nat. Mater.* **10**(4), 273–277 (2011)
54. Qian, T., Wang, X.P., Jin, W.C., Zhang, P., Richard, P., Xu, G., Dai, X., Fang, Z., Guo, J.-G., Chen, X.-L., Ding, H.: Absence of a holelike Fermi surface for the iron-based $\text{K}_{0.8}\text{Fe}_{1.7}\text{Se}_2$ superconductor revealed by angle-resolved photoemission spectroscopy. *Phys. Rev. Lett.* **106**(18), 187001 (2011)
55. Mou, D., Liu, S., Jia, X., He, J., Peng, Y., Zhao, L., Yu, L., Liu, G., He, S., Dong, X., Zhang, J., Wang, H., Dong, C., Fang, M., Wang, X., Peng, Q., Wang, Z., Zhang, S., Yang, F., Xu, Z., Chen, C., Zhou, X.J.: Distinct Fermi surface topology and nodeless superconducting gap in a $(\text{Tl}_{0.58}\text{Rb}_{0.42})\text{Fe}_{1.72}\text{Se}_2$ superconductor. *Phys. Rev. Lett.* **106**(10), 107001 (2011)
56. Zhao, L., Mou, D., Liu, S., Jia, X., He, J., Peng, Y., Yu, L., Liu, X., Liu, G., He, S., Dong, X., Zhang, J., He, J.B., Wang, D.M., Chen, G.F., Guo, J.G., Chen, X.L., Wang, X., Peng, Q., Wang, Z., Zhang, S., Yang, F., Xu, Z., Chen, C., Zhou, X.J.: Common Fermi-surface topology and nodeless superconducting gap of $\text{K}_{0.68}\text{Fe}_{1.79}\text{Se}_2$ and $(\text{Tl}_{0.45}\text{K}_{0.34})\text{Fe}_{1.84}\text{Se}_2$ superconductors revealed via angle-resolved photoemission. *Phys. Rev. B* **83**(14), 140508(R) (2011)
57. Yu, R., Si, Q.: Mott transition in multiorbital models for iron pnictides. *Phys. Rev. B* **84**(23), 235115 (2011)
58. Si, Q., Abrahams, E.: Strong correlations and magnetic frustration in the high T_c iron pnictides. *Phys. Rev. Lett.* **101**(7), 076401 (2008)
59. Hirschfeld, P.J., Korshunov, M.M., Mazin, I.I.: Gap symmetry and structure of Fe-based superconductors. *Rep. Prog. Phys.* **74**(12), 124508 (2011)

Chapter 2

Angle-Resolved Photoemission Spectroscopy

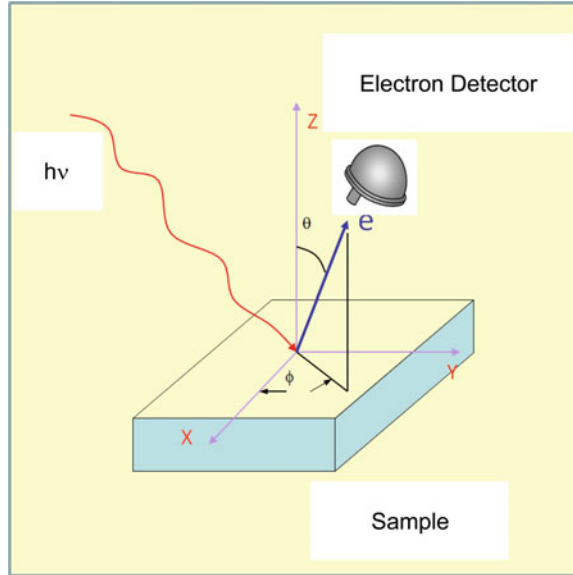
Angle-resolved photoemission spectroscopy (ARPES) is a powerful tool to directly probe the electronic structure of materials, which has been broadly used in the research of condensed matter physics. It plays an important role in unraveling the mechanism of many exotic phenomena in high-temperature superconductors, graphene, topological insulator, and many other advanced materials [1–6]. Generally speaking, ARPES measures the electronic structure of a material via photoelectrons. Shown in Fig. 2.1 is a sketch of an ARPES system containing the light source, sample, and analyzer.

In the history of photoemission, the first breakthrough was the observation of photoelectric effect in 1887 by Hertz [7]. It was then explained by Einstein in 1905 [8] with a simple equation describing the photoelectric effect:

$$E_{\max} = h\nu - \Phi. \quad (2.1)$$

in which E_{\max} is the maximum kinetic energy of the emitted photoelectrons, $h\nu$ is the energy of the incident photon, and Φ is the sample work function. Continuous efforts have been made over a hundred years, which finally enable an accurate measurement of the energy and momentum of the photoelectrons. Spin-resolved photoemission spectroscopy has also been developed, which probes the spin of the electrons. Combining the information of energy, momentum, and spin, one can have a full description of the electronic states in the materials. The light source has also been improved over the decades. Besides the synchrotron radiation and gas discharge lamps, a newly developed laser source has induced significant improvement to the total resolution of the ARPES system by its monochromaticity and narrow line width. The works presented in this book are mainly based on ARPES. In this chapter, a general description of the ARPES technique will be given. In particular, it will explain how the energy and momentum of the electrons are resolved and what physical quantities are deduced from the ARPES spectra.

Fig. 2.1 Schematic of ARPES



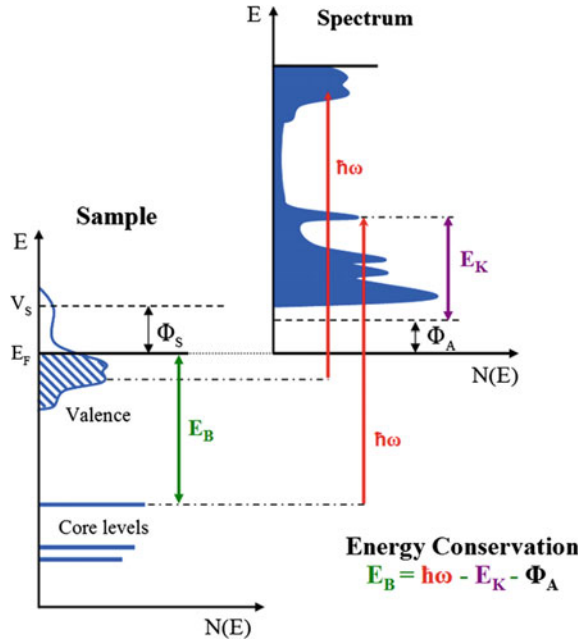
2.1 Energy Resolution of ARPES

Based on Einstein's equation for photoelectric effect, we have:

$$E_{kin} = h\nu - |E_B| - \Phi. \quad (2.2)$$

in which E_{kin} is the kinetic energy of the photoelectrons, $h\nu$ is the energy of the incident photon, Φ is the sample work function, and E_B is the binding energy of the initial states of the electrons in the material. For simplicity, fermi level of the material is always used as an energy reference and binding energy is therefore presented with negative values. If we only consider the energy resolution, then we can simply ignore the emission angles of the photoelectrons and calculate the electron density of states as a function of energy. Figure 2.2 illustrates how the density of states is probed by the photoemission process. According to the energy conservation law, electrons with different binding energy (e.g., valence bands vs. core levels) emit into the vacuum with different kinetic energies after absorbing photons with the same amount of energy. The kinetic energy of the photoelectrons is then detected by the electron analyzer. Shown on the top right of the figure is a typical photoemission spectrum in which the original shallow valence bands and deep core levels are presented as sharp peaks with different kinetic energies. Using Eq. 2.2, we can directly calculate the corresponding binding energy E_B of the original bands or core levels from the measured kinetic energy, which realizes the energy resolution. Nevertheless, according to Eq. 2.2, the correct analysis also depends on the correct determination of work function, which will be discussed in detail below. We also note that accurate analysis of the data

Fig. 2.2 Schematic of photoemission, in which E_F is the Fermi energy, E_B is the binding energy, Φ_S is the work function of the sample, Φ_A is the work function of the analyzer, and E_K is the electron kinetic energy detected by the analyzer [2]



will sometimes involve various factors, for example, the background given by the scattering of secondary electrons.

2.1.1 ARPES Measures the Occupied States

ARPES measures the photoelectrons which are ejected from the initial states to the final states after absorbing the incident photons. In other words, it measures the electronic states occupied by electrons but not the unoccupied states. To measure the unoccupied states, inverse photoemission is needed, in which low-energy electrons are directed at the sample surface and coupled with the unoccupied states. The occupied electrons to be measured by ARPES are governed by Fermi–Dirac distribution function. At zero temperature, if the energy resolution of the system is perfect, then the measured electronic states should show a sudden cutoff in the form of a step function as shown in Fig. 2.2. This is called Fermi cutoff, and the corresponding energy is Fermi energy, an energy reference for the binding energy of the occupied electronic states. In real experiments, the Fermi cutoff is broadened by the temperature and energy resolution of the measurements. On the one hand, we can take advantage of this broadening and calibrate the energy resolution of the system at a given temperature. On the other hand, we can also check the temperature of the sample by the Fermi cutoff broadening when the energy resolution is known.

2.1.2 *The Selection of Work Function*

Another important term included in Eq. 2.2 is work function. Work function is an energy barrier which prevents the electrons from leaving the materials. The existence of work function at the material surface is natural. Naively, if there is no work function, then electrons with the highest energy in the material can leave the material surface and get into the vacuum without losing any energy, and thus, no stable bulk material can ever exist. The correct selection of work function is very crucial for the ARPES measurement. As for the photoemission process alone, the work function refers to material work function which is the energy an photoelectron needs to pay if it moves from the Fermi level of the material to the vacuum. However, in the real measurement, the free electron-like photoelectrons are measured by the electron analyzer. The electric contact between the sample and the electron analyzer aligns their Fermi levels but not the work functions. Therefore, the measured kinetic energy is relative to the work function of the analyzer, which might be different from the real kinetic energy of the photoelectrons. In other words, if the work function of the material is different from that of the electron analyzer, then the photoelectrons are accelerated or decelerated in the analyzer. Nevertheless, the energy conservation law in Eq. 2.2 is still valid. In order to get the correct binding energy from the measured kinetic energy of the photoelectrons, we need to replace the sample work function with the work function of the electron analyzer.

This work function difference is always very small, and the acceleration or deceleration process is perpendicular to the sample surface and thus does not change the in-plane momentum of the photoelectrons. By considering the work function of the electron analyzer, this effect can be corrected. Nevertheless, we should notice that the real work function which takes place in the photoemission process is the material work function. Therefore, the lower limit of the photoelectron kinetic energy is determined by the material work function. This point has also been clearly illustrated in Fig. 2.2, in which Φ_S is the work function of the material and Φ_A is the work function of the electron analyzer. If $\Phi_S > \Phi_A$, in a certain energy range where the minimum kinetic energy of the photoelectrons E_K determined by Φ_A is larger than zero but $E_K + \Phi_A < \Phi_S$, no spectral weight is obtained in the electron analyzer. This is shown in Fig. 2.2 that an energy cutoff appears at V_S , below which the measured electron density is zero. This is simply because those electrons cannot leave the sample surface in the photoemission process and thus cannot be detected by the analyzer.

2.2 Momentum Resolution of ARPES

In the previous discussion, only energy conservation of the photoemission process was used. We notice that there is also momentum conservation in ARPES measurements. Correct analysis of the momentum conservation can give us the momentum

information of the electrons in the materials and thus realize the momentum resolution. Photoemission is a complicated process which involves the incident photons, photoelectrons, and the detection of photoelectrons. In order to accurately describe it, a so called one-step model is needed [9–12]. In this model, the absorption of photons, ejection of electrons, movement of the photoelectrons, and the detection are all considered as a coherent process and the properties of the bulk material, sample surface, and vacuum level are all included. Although accurate, this model is hard to be understood. Another phenomenology model is also proposed [13, 14], in which the photoemission is divided into three steps: (1) The ejection of electrons from initial states to final states. (2) Travel of the excited electrons from the bulk material to its surface. (3) Escape of the excited electrons from the sample surface into the vacuum. This model is called “three-step model.”

2.2.1 Momentum Conservation in Step One: Ejection of Electrons from Initial to Final States

This is the most important step in the three-step model, in which the essential information of the electron interactions is included. When incident light is directed on the sample surface, the electron of the material may absorb a photon and be ejected from the initial state to a final state. In typical ARPES measurements with soft X-rays, the photon energy is from several eV to ~ 100 eV and the corresponding momentum of the photons is negligible comparing to that of the electrons. Therefore, although the energy of the electron is changed by $h\nu$ in the ejection, the momentum of the electron conserves. Shown in Fig. 2.3 is an illustration of this process. After absorbing a photon with an energy of $h\nu$, the electron in the occupied initial state jumps vertically to a final state above Fermi level without changing its momentum. This is called “vertical transition.” In order to quantitatively describe this process, we study the momentum along x, y, and z directions, respectively.

If we label the electron momentum in the initial state as K_i and that of the final state as K_f , then we have:

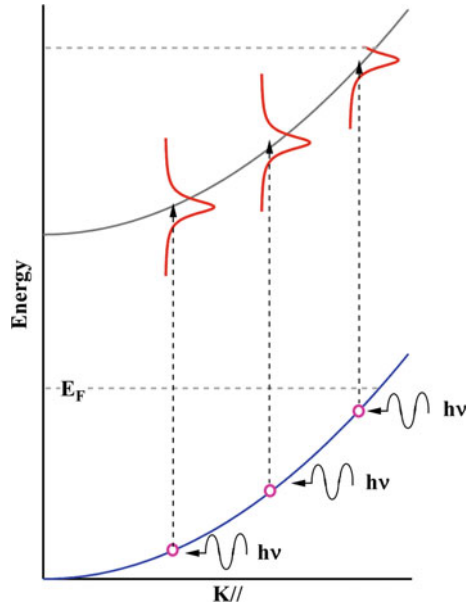
$$K_{f,x} = K_{i,x}; K_{f,y} = K_{i,y}; K_{f,z} = K_{i,z}. \quad (2.3)$$

As a comparison, the equation for the energy conservation in the first step is also listed here:

$$E_f = h\nu + E_B. \quad (2.4)$$

in which E_B is the electron binding energy which is the same as the electron energy in its initial state E_i .

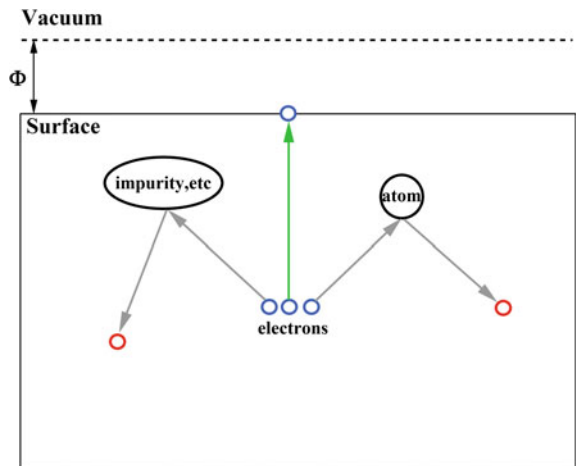
Fig. 2.3 The first step in the “three-step model,” the ejection of electrons from initial states to final states



2.2.2 Momentum Conservation in Step Two: Traveling of the Excited Electrons to Sample Surface

The second step of photoemission is the travel of the excited electrons from bulk material to the sample surface. As shown in Fig. 2.4, many inelastic-scattering processes are involved in this step. For example, the excited electrons might be scattered by

Fig. 2.4 The second step in the “three-step model,” travel of the excited electrons from the bulk material to its surface



other atoms or impurities. Secondary electrons might also be created in the process. However, only the electrons which are not scattered in their travel to the sample surface can contribute to the intrinsic electronic structure we measure. The following two points should be noticed: First, not all the excited electrons move toward the sample surface. Second, the scattered electrons might also travel to the sample surface and be detected, which do not represent the intrinsic electronic states in the material. However, the scattered electrons do not have a particular preference on the emission angle; therefore, they only contribute to some background in the measured photoemission intensity. The intrinsic signal comes from the excited electrons without any scattering. For those electrons, the momentum and energy do not change in step 2. If we define the corresponding momentum as K_{in} and energy as E_{in} , then we have:

$$K_{in,x} = K_{f,x}; K_{in,y} = K_{f,y}; K_{in,z} = K_{f,z}. \tag{2.5}$$

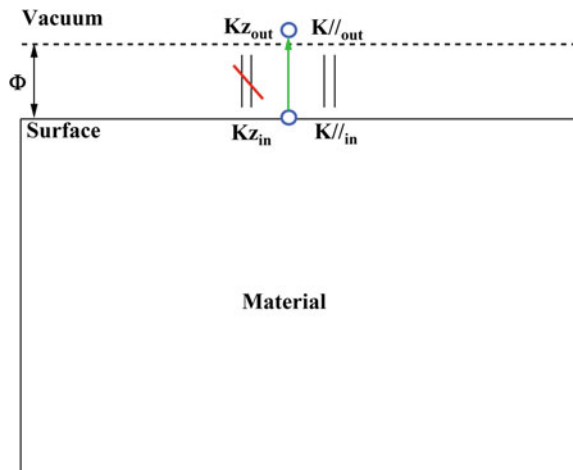
$$E_{in} = E_f. \tag{2.6}$$

2.2.3 Momentum Conservation in Step Three: Escape of the Excited Electrons into the Vacuum

In order to escape from the sample surface into the vacuum, the excited electrons need to go through the surface potential barrier, as shown in Fig. 2.5.

The energy of the potential barrier is the work function Φ of the material. In this step, the in-plane symmetry of the sample is not affected by the photoemission process. In other words, the in-plane momentum of the excited electrons keeps the same. On the other hand, the crystal symmetry is broken along the sample surface

Fig. 2.5 The third step in the “three-step model,” escape of the excited electrons from the sample surface into the vacuum



normal with the appearance of an interface between sample and vacuum. The excited electrons are coupled with the potential barrier perpendicular to the sample surface. Therefore, the momentum conservation law for the excited electrons along the sample surface normal is broken. Of course, the energy of the excited electrons is also changed due to the potential barrier. If we define the momentum of the electrons in the vacuum as K_{out} and the corresponding energy as E_{out} , then:

$$K_{out,x} = K_{in,x}; K_{out,y} = K_{in,y}; K_{out,z} \neq K_{in,z}. \quad (2.7)$$

$$E_{out} = E_{in} - \Phi. \quad (2.8)$$

If the materials are 2D or quasi-2D (for example, cuprate high-temperature superconductors, selected iron-based superconductors, thin films), only the in-plane momenta ($K_{i,x}$, $K_{i,y}$) are concerned. By using Eqs. 2.7, 2.5, and 2.3, we can easily get $K_{i,x}$, $K_{i,y}$ from $K_{out,x}$ and $K_{out,y}$ which are the momenta of the photoelectrons measured by the analyzer. Therefore, the key step is to calculate $K_{out,x}$ and $K_{out,y}$ from E_{out} and the corresponding electron emission angles, both of which are directly measured by the experiment. As for the photoelectron detected by the electron analyzer, the free electron-like plane wave is a sufficient description:

$$E_{out} = \frac{\hbar^2}{2m_e} (K_{out,x}^2 + K_{out,y}^2 + K_{out,z}^2). \quad (2.9)$$

For the electron analyzer with a horizontal slit, the momenta of the photoelectrons can be given as:

$$\begin{aligned} K_{out,x} &= \frac{1}{\hbar} \sqrt{2m_e E_{out}} \sin \Phi; K_{out,y} = \frac{1}{\hbar} \sqrt{2m_e E_{out}} \cos \Phi \sin \Theta; \\ K_{out,z} &= \frac{1}{\hbar} \sqrt{2m_e E_{out}} \cos \Phi \cos \Theta. \end{aligned} \quad (2.10)$$

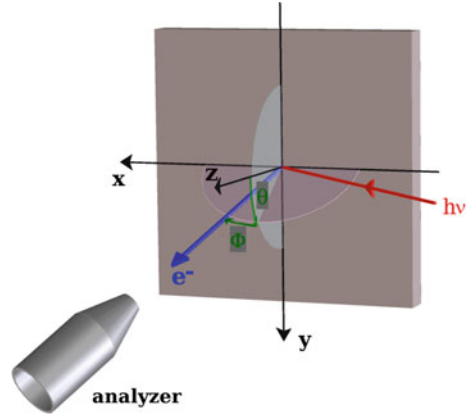
The corresponding emission angles are defined in Fig. 2.6.

Therefore,

$$K_{i,x} = \frac{1}{\hbar} \sqrt{2m_e E_{out}} \sin \Phi; K_{i,y} = \frac{1}{\hbar} \sqrt{2m_e E_{out}} \cos \Phi \sin \Theta. \quad (2.11)$$

As illustrated above, the momenta of the initial states $K_{i,x}$, $K_{i,y}$ can be obtained by the measured electron kinetic energy E_{out} and the corresponding electron emission angles, and thus, the momentum resolution can be achieved by ARPES.

Fig. 2.6 Different angles in the ARPES system. The momenta can be calculated from the angles [2]



2.2.4 Determination of K_z in 3D Systems [2, 15]

ARPES is broadly used to study 2D systems. Due to the breaking of momentum conservation along the sample surface normal, the measurement of K_z in 3D materials is not as straightforward as that of the in-plane momenta. $K_{i,z}$ of the initial state is not given by $K_{out,z}$ directly. However, we are still able to get the information of $K_{i,z}$ under some simple assumptions. Let us first consider the excited electrons after step one in the three-step model. Being ejected to the final states, those electrons can be assumed as quasi-free electrons and thus be described as:

$$E_f = \frac{\hbar^2}{2m_e} (K_{f,x}^2 + K_{f,y}^2 + K_{f,z}^2) + E_0. \quad (2.12)$$

Here, E_0 is called “bottom of the muffin tin” which represents the energy of the parabolic band bottom. Considering Eqs. 2.3, 2.6, and 2.8, we have:

$$E_{out} = \frac{\hbar^2}{2m_e} (K_{i,x}^2 + K_{i,y}^2 + K_{i,z}^2) + E_0 - \Phi. \quad (2.13)$$

Then,

$$K_{i,z} = \sqrt{\frac{2m_e}{\hbar^2} (E_{out} + \Phi - E_0) - K_{i,x}^2 - K_{i,y}^2}. \quad (2.14)$$

If we define $E_0 - \Phi$ as inner potential V_0 , then:

$$K_{i,z} = \sqrt{\frac{2m_e}{\hbar^2} (E_{out} - V_0) - K_{i,x}^2 - K_{i,y}^2}. \quad (2.15)$$

A simple way to determine V_0 is to measure normal emitted electrons whose in-plane momenta $K_{i,x} = K_{i,y} = 0$. By changing the photon energy of the incident beam, we can get different E_{out} values. We also know that $K_{i,z}$ should follow the periodicity of the 3D Brillouin zone. Therefore, we can get V_0 by fitting various attempted $K_{i,z}$ values (obtained with different photon energies) to the Brillouin zone boundary. Finally, the real $K_{i,z}$ can be directly calculated with the obtained V_0 .

2.3 Physical Properties Measured by ARPES [1, 2]

As explained in the previous sections that the energy and momentum resolutions of ARPES are realized by measuring the photoelectrons which are emitted from the material into the vacuum. However, electrons in most materials are correlated. For example, in a strongly correlated superconducting system, the electron–electron and electron–boson interactions are very important. A natural question for ARPES measurement is: How can we get the information of the many-body interactions in the materials by measuring the free electron-like excited photoelectrons. In this section, explanations will be given by introducing the single-particle spectral function.

2.3.1 Transition Probability for the Optical Excitation

Let us consider an optical excitation process in a system with N-electrons. Electrons are excited after absorbing photons, and the N-electron system goes from an initial state Ψ_i^N to a final state Ψ_f^N . The transition probability w_{fi} for this excitation process is given by Fermi's golden rule:

$$w_{fi} = \frac{2\pi}{\hbar} | \langle \Psi_f^N | H_{int} | \Psi_i^N \rangle |^2 \delta(E_f^N - E_i^N - h\nu). \quad (2.16)$$

$E_i^N = E_i^{N-1} - E_B^k$ and $E_f^N = E_f^{N-1} + E_{kin}$ are the energy values for the initial states and final states, respectively. E_B^k is the original binding energy of the photoelectron whose kinetic energy is E_{kin} and momentum is k . The operator describing the interaction between electron and photon is given by

$$H_{int} = \frac{-e}{2mc} (\mathbf{A} \cdot \mathbf{p} + \mathbf{p} \cdot \mathbf{A}) = -\frac{e}{mc} \mathbf{A} \cdot \mathbf{p}, \quad (2.17)$$

under a perturbation theory. Here, \mathbf{p} is the electronic momentum operator, and \mathbf{A} is the electromagnetic vector potential. It seems that the many-body interactions included in these equations are too complicated to be calculated. In order to simplify this problem and obtain the essential physical properties of the materials, reasonable assumptions are needed.

2.3.1.1 Sudden Approximation and Adiabatic Limit

Although based on single-particle picture which is not ideal for the discussion of many-body interactions, the three-step model has achieved great success in practice. Electron transition in the first step of the model contains essential information of the many-body interactions. For simplicity, let us consider the excitation of one electron in the N-electron system. If the transition process is so fast that the excited electron does not interact with the rest N-1 electrons, then the question is simplified and the final state of the N-electron system can be written as:

$$\Psi_f^N = \mathcal{A} \phi_f^k \Psi_f^{N-1}. \quad (2.18)$$

in which \mathcal{A} is an antisymmetric operator, ϕ_f^k is the wave function of the photoelectron, and Ψ_f^{N-1} is the final state wave function of the (N-1)-electron system which can be written as an eigenstate Ψ_m^{N-1} with energy E_m^{N-1} . Then, the total transition probability can be estimated by summing over m. This is called “sudden approximation” in which the photoemission process is assumed to be sudden [1]. This approximation works good for photoelectrons with high kinetic energy. However, if the kinetic energy of the photoelectron is very low that the time it takes to escape is comparable to the system response time, then the transition process cannot be regarded as sudden and the sudden approximation cannot be used any more. This is called “adiabatic limit” [16]. In this case, the final state wave function cannot be simplified in the above way and will be much more complicated. A practical concern is the lower limit of the photon energy by which the “sudden approximation” still works. This question is still under debate. It has been generally accepted that “sudden approximation” works for the light from helium lamp which provides photons with an energy of 21.2 eV. Experiments with an photon energy of 19 eV has also been reported in which “sudden approximation” also works good [17]. Other papers indicate that the “sudden approximation” is still OK with a photon energy of 6.05 eV [18, 19]. Recently, with the advantage of small band width and high photon flux, laser has been used as a new light source for ARPES which greatly improved the data quality. However, the photon energy of laser is relative low ($\sim 6-10$ eV) which makes people worry about the solidity of “sudden approximation.” Fortunately, experimental evidence indicates that the “sudden approximation” still works good with laser light source.

2.3.1.2 Transition Probability Under Sudden Approximation

For simplicity, we write the initial state of the N-electron system Ψ_i^N as the combination of a one-electron wave function ϕ_i^k and an (N-1)-electron term Ψ_i^{N-1} :

$$\Psi_i^N = \mathcal{A} \phi_i^k \Psi_i^{N-1}, \quad (2.19)$$

where $\Psi_i^{N-1} = c_k \Psi_i^N$, and c_k is the annihilation operator for an electron with momentum k . Here, Ψ_i^{N-1} is not an eigenstate of the (N-1)-electron system. It is just the remaining part of the N-electron wave function after removing one electron. Therefore, the matrix elements in Eq. 2.16 can be written as:

$$\langle \Psi_f^N | H_{int} | \Psi_i^N \rangle = \langle \phi_f^k | H_{int} | \phi_i^k \rangle \langle \Psi_m^{N-1} | \Psi_i^{N-1} \rangle, \quad (2.20)$$

in which $\langle \phi_f^k | H_{int} | \phi_i^k \rangle = M_{f,i}^k$ is called one-electron dipole matrix element. The final state of the (N-1)-electron system Ψ_f^{N-1} is an eigenstate and thus can be replaced by Ψ_m^{N-1} . Then, the photoemission intensity $I(k, E_{kin})$ can be written as:

$$I(k, E_{kin}) = \sum_{f,i} w_{f,i} \propto \sum_{f,i} |M_{f,i}^k|^2 \sum_m |c_{m,i}|^2 \delta(E_{kin} + E_m^{N-1} - E_i^N - h\nu), \quad (2.21)$$

in which $|c_{m,i}|^2 = |\langle \Psi_m^{N-1} | \Psi_i^{N-1} \rangle|^2$ represents the probability that the remaining (N-1)-electron system is at the eigenstate m after removing one electron from the i state. It includes the fundamental information of the transition.

In order to understand the transition probability, let us first consider a non-interacting electron system. In this case, the removal of one electron in the N-electron system does not have any effect on the rest electrons, which means the Ψ_i^{N-1} state is still an eigenstate $\Psi_{m_0}^{N-1}$ of the $(N-1)$ -electron system. Therefore, in the equation of photoemission intensity $I(k, E_{kin})$, only $|c_{m_0,i}|^2 = 1$ (when $m = m_0$) and all the other $c_{m,i}$ terms are zero. Considering the δ function part in $I(k, E_{kin})$, we should expect ARPES spectra with δ function peaks at $E_B^k = -\epsilon_k$. However, in correlated systems, the removal of one electron gives rise to a dramatic change to the rest (N-1)-electron system. Therefore, many terms of $|c_{m,i}|^2 \neq 0$ and Ψ_i^{N-1} will overlap with many of the eigenstates Ψ_m^{N-1} . The corresponding ARPES spectra will not show single delta functions any more. Instead, a main line with several satellites is expected (Fig. 2.7).

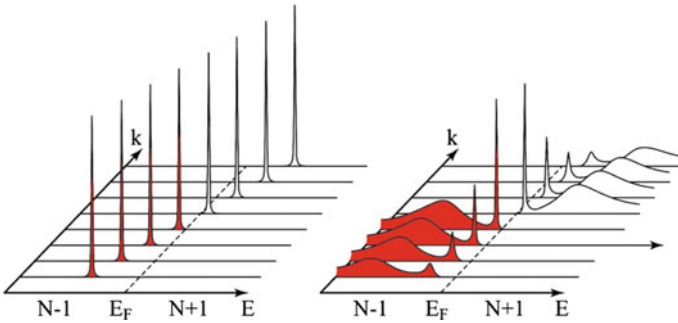


Fig. 2.7 *Left panel:* ARPES spectra for a non-interacting electron system. *Right panel:* ARPES spectra for correlated systems. The filled red regions represent the occupied states, whereas the empty regions represent the unoccupied states [2]

2.3.2 Single-Particle Spectral Function

Green's function has been widely used in solid physics to describe many-body effects. The propagation of a single electron can be written as a time-ordered one-electron Green's function $g(t - t')$ which describes the probability amplitude that an electron added at a time of zero keeps in the same state after a time of $|t - t'|$. An energy-momentum representation can be given by performing a Fourier transform:

$$G^\pm(k, \omega) = \sum_m \frac{|\langle \Psi_m^{N\pm 1} | c_k^\pm | \Psi_i^N \rangle|^2}{\omega - E_m^{N\pm 1} + E_i^N \pm i\eta}, \quad (2.22)$$

in which $G^+(k, \omega)$ and $G^-(k, \omega)$ represent the Green's function for adding and removing a single electron, respectively. The single-particle spectral function can thus be given by the imaginary part of the Green's function:

$$A(k, \omega) = A^+(k, \omega) + A^-(k, \omega) = -(1/\pi) \text{Im} G(k, \omega); \quad (2.23)$$

$$A^\pm(k, \omega) = \sum_m |\langle \Psi_m^{N\pm 1} | c_k^\pm | \Psi_i^N \rangle|^2 \delta(\omega - E_m^{N\pm 1} + E_i^N). \quad (2.24)$$

By comparing the single-particle spectral function $A^-(k, \omega)$ with the photoemission intensity $I(k, E_{kin})$ (Eq. 2.21), we have:

$$I(k, E_{kin}) \propto \sum_{f,i} |M_{f,i}^k|^2 A^-(k, \omega). \quad (2.25)$$

Therefore, it is clear that the photoemission intensity measured by ARPES is proportional to the single-particle spectral function which explains the reason why the energy gap, Fermi surface, band structures, and many-body effects in the materials can be captured by the ARPES spectra.

References

1. Damascelli, A., Hussain, Z., Shen, Z.-X.: Angle-resolved photoemission studies of the cuprate superconductors. *Rev. Mod. Phys.* **75**, 473–541 (2003)
2. Jozwiak, C.M.: A New Spin on Photoemission Spectroscopy. PhD thesis, University of California, Berkeley (2008)
3. Campuzano, J.C.: *The Physics of Superconductors: Superconductivity in Nanostructures, High- T_c and Novel Superconductors, Organic Superconductors*. Springer, Heidelberg (2004)
4. Zhou, X.J., Cuk, T., Devereaux, T., Nagaosa, N., Shen, Z.-X.: *Handbook of High-temperature Superconductivity: Theory and Experiment*. Springer, New York (2007)
5. Bostwick, A., Ohta, T., Seyller, T., Horn, K., Rotenberg, E.: Quasiparticle dynamics in graphene. *Nat. Phys.* **3**(1), 36–40 (2007)
6. Hasan, M.Z., Kane, C.L.: Colloquium: topological insulators. *Rev. Mod. Phys.* **82**(4), 3045 (2010)
7. Hertz, H.: *Ann. Phys. (Leipzig)* **31**, 983 (1887)

8. Einstein, A.: *Ann. Phys. (Leipzig)* **31**, 132 (1905)
2. Mahan, G.D.: Theory of photoemission in simple metals. *Phys. Rev. B* **2**, 4334–4350 (1970)
10. Schaich, W.L., Ashcroft, N.W.: Model calculations in the theory of photoemission. *Phys. Rev. B* **3**, 2452–2465 (1971)
11. Caroli, C., Lederer-Rozenblatt, D., Roulet, B., Saint-James, D.: Inelastic effects in photoemission: microscopic formulation and qualitative discussion. *Phys. Rev. B* **8**, 4552–4569 (1973)
12. Feibelman, P.J., Eastman, D.E.: Photoemission spectroscopy-correspondence between quantum theory and experimental phenomenology. *Phys. Rev. B* **10**, 4932–4947 (1974)
13. Fan, H.Y.: Theory of photoelectric emission from metals. *Phys. Rev.* **68**, 43–52 (1945)
14. Berglund, C.N., Spicer, W.E.: Photoemission studies of copper and silver: theory. *Phys. Rev.* **1**(36), A1030–A1044 (1964)
15. Chiang, T.C., Knapp, J.A., Aono, M., Eastman, D.E.: Angle-resolved photoemission, valence-band dispersions $E(k)$, and electron and hole lifetimes for GaAs. *Phys. Rev. B* **21**(8), 3513 (1980)
16. Gadzuk, J.W.: Šunjić.: excitation energy dependence of core-level x-ray-photoemissionspectra line shapes in metals. *Phys. Rev. B* **12**, 524–530 (1975)
17. Randeria, M., Ding, H., Campuzano, J.-C., Bellman, A., Jennings, G., Yokoya, T., Takahashi, T., Katayama-Yoshida, H., Mochiku, T., Kadowaki, K.: Momentum distribution sum rule for angle-resolved photoemission. *Phys. Rev. Lett.* **74**, 4951–4954 (1995)
18. Koralek, J.D., Douglas, J.F., Plumb, N.C., Sun, Z., Fedorov, A.V., Murnane, M.M., Kapteyn, H.C., Cundiff, S.T., Aiura, Y., Oka, K., Eisaki, H., Dessau, D.S.: Laser based angle-resolved photoemission, the sudden approximation, and quasiparticle-like spectral peaks in $\text{Bi}_2\text{Sr}_2\text{CaCu}_2\text{O}_{8+\delta}$. *Phys. Rev. Lett.* **96**, 017005 (2006)
19. Koralek, J.D., Douglas, J.F., Plumb, N.C., Griffith, J.D., Cundiff, S.T., Kapteyn, H.C., Murnane, M.M., Dessau, D.S.: Experimental setup for low-energy laser-based angle resolved photoemission spectroscopy. *Rev. Sci. Instrum.* **78**(5), 053905 (2007)

Chapter 3

ARPES Systems

ARPES, a powerful experimental tool to detect the electronic structures of materials, has been broadly used in the research on many advanced materials in the past several decades [1]. Direct evidence obtained by ARPES has been helping people to understand the exotic physical phenomena in materials. Meanwhile, progresses have also been made on the ARPES systems. Momentum resolution and spin resolution have been achieved in addition to the original energy resolution in photoemission spectroscopy (PES). The energy resolution has also been improved from tens of meVs to better than 1 meV with a momentum resolution better than 0.004 \AA^{-1} [2]. As for the detection efficiency, the earliest point detector was replaced by the analyzer with a slit which can measure a momentum cut at a time. The recent development of time-of-flight 2D detector has enabled the real-time measurement of a momentum area, which would greatly improve the efficiency of the measurement. Progresses have also been made in the light source of the ARPES system. Besides the synchrotron light source and gas discharge lamp, the newly developed laser has improved the ARPES data quality dramatically by its low bandwidth and high intensity. The first 7-eV vacuum ultraviolet laser-based angle-resolved photoemission system was developed by our group collaborated with Prof. Chen and Prof. Xu's groups [2]. After that, tunable laser-based angle-resolved photoemission system, laser-based spin-resolved ARPES system, and laser-based time-of-flight ARPES system have been developed. The research results to be presented in the following chapters were all performed on those newly developed systems, and the super-high resolution of the laser light source was key to the success of the research on cuprates. In this chapter, a general introduction of the typical ARPES systems will be given and the performance of the aforementioned laser-based ARPES systems will be described.

3.1 Constituents and Categories of ARPES Systems

3.1.1 *Constituents of a Typical ARPES System*

Angle-resolved photoemission spectroscopy (ARPES) system is a powerful experimental tool to study the electronic structures in the materials with exotic physical phenomena.

As described in the last chapter, the ARPES measurements are based on the photoemission process. Therefore, a suitable light source is a must for an ARPES system. Then, what are the criteria for a good light source? Firstly, the photon energy of the incident light should be larger than the work function of the material such that the excited electrons can get out of the material and be detected. Secondly, the line width of the light should be small, because the total energy resolution of the ARPES system is decided by the resolution of the electron analyzer convolved with the line width of the incident light. Since the best energy resolution achievable by the state-of-the-art electron analyzer is very good, the line width of the light works as the limit for the total energy resolution of the system. Thirdly, the flux of the light source should be optimized. On the one hand, if the flux is too low, the statistics of the data will be affected. On the other hand, if the flux is too high, especially for the pulsed light, the so-called space charge effect will appear which is not good for the measurement. This will be elaborated later in this chapter.

Besides the light source, another key constituent for the ARPES system is the vacuum. The ARPES measurement is based on the detection of intrinsic angle and energy of the photoelectrons. Therefore, the scattering of the photoelectrons by the atoms in the air should be avoided before the detection, and thus, a measurement in vacuum is needed. In the ARPES system, many different pumps are used to keep a low pressure in the measurement chamber. The typical pumps include turbopump, cryopump, ion pump, non-evaporable getters, titanium sublimation pump, and screw pump. The typical base pressure for the ARPES system is better than 5×10^{-11} mbar. In our newly developed systems, the best base pressure is lower than 5×10^{-12} mbar. Meanwhile, we do not want the photoelectrons to be affected by any magnetic field. Thus, a magnetically shielded measurement chamber is also important.

Since the measurement should be taken in vacuum and most of the samples are prepared in the air, a sample transferring system is needed in the ARPES system. However, the measurement chamber with a base pressure of $\sim 5 \times 10^{-11}$ mbar cannot be connected to the air directly. Otherwise, the base pressure cannot get back to 10^{-11} mbar in a short time. Therefore, a load lock and a preparation chamber are included in the ARPES system. The base pressure of the load lock is between 10^{-7} mbar and 10^{-8} mbar, which can be recovered very quickly from the normal pressure of the atmosphere after loading samples from the air. The preparation chamber is between load lock and measurement chamber with a base pressure of 10^{-9} – 10^{-10} mbar. The pressure of the preparation chamber will increase when it is connected to the load lock for sample transfer. However, it can get back to the normal value very quickly because the pressure difference between load lock and

preparation chamber is not much. The same is true for the sample transfer between preparation chamber and measurement chamber, such that the pressure of the measurement chamber can get back to the 10^{-11} mbar level and measurements can be carried out within a short time.

As for the measurements, an electron analyzer is necessary. The state-of-the-art electron analyzers are the so-called hemispheric analyzer in which a slit is used. Only the electrons passing through the slit can be captured. Different positions along the slit can be used to determine the emission angles of the electrons and calculate the corresponding momenta. The angle information of the photoelectrons will be recorded by the horizontal axis of the MCP in the detector. Meanwhile, the vertical axis of the MCP records the energy of the photoelectrons, because electrons with different velocities move in trajectories with different diameters in the electrically biased hemispheric analyzer. Spin-resolved analyzer has also been developed based on the current hemispheric analyzer, which can resolve spin, energy, and momentum of the photoelectrons. Besides the hemispheric analyzer, another type of electron analyzer has also been developed recently which looks like a cylinder. In this analyzer, the energy of a photoelectron is detected by the time it takes to fly from the sample surface to the detector and both horizontal and vertical axes of the MCP can be used to record the momenta of the electrons. Therefore, both K_x and K_y can be measured at the same time, and thus, the area detection in the momentum space is realized. This electron analyzer is the so-called angle-resolved time-of-flight (ARTOF) analyzer.

Low-temperature measurements are always very critical for many samples; therefore, a cryostat is very important for the ARPES system. Meanwhile, the acceptance angle of the electron analyzer is not large enough to cover the photoelectrons with large emission angles. Therefore, the rotational degrees of freedom are needed for the cryostat. These functions are realized in our six-axis cryostat of the ARPES system (shown in Fig. 3.1). By using liquid helium, whose boiling temperature is 4.2 K, the lowest temperature at the sample position is lower than 10 K. Meanwhile, free rotations along Φ , Θ , and Ω angles and free motions along X, Y, and Z directions are also realized in this cryostat. In order to further cool down the sample and improve the efficiency in using liquid helium, we made the second-generation six-axis cryostat, as shown in Fig. 3.2. The test of the new cryostat has been performed very recently.

3.1.2 Categories of ARPES Systems

ARPES systems can be divided into three categories by different light sources: synchrotron-based ARPES, gas discharge lamp-based ARPES, and laser-based ARPES. ARPES systems can also be labeled by different electron analyzers: one-dimensional ARPES, two-dimensional ARPES, time-of-flight (3D) ARPES, and spin-resolved ARPES. Besides, there are other ARPES systems with special functions. For example, time-resolved ARPES can be used to study the non-equilibrium dynamics in the material system and spatially resolved ARPES has the capability

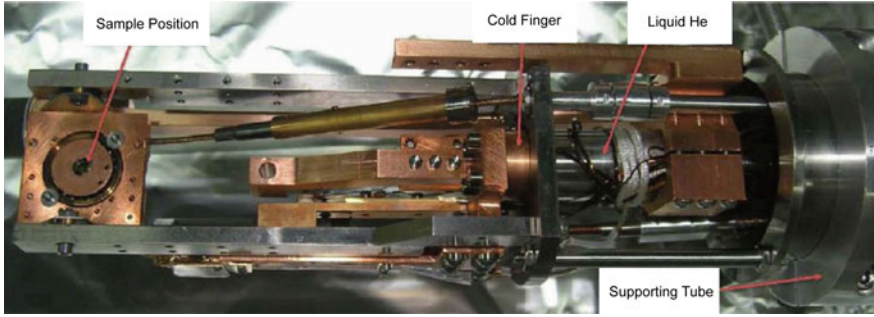


Fig. 3.1 Six-axis cryostat

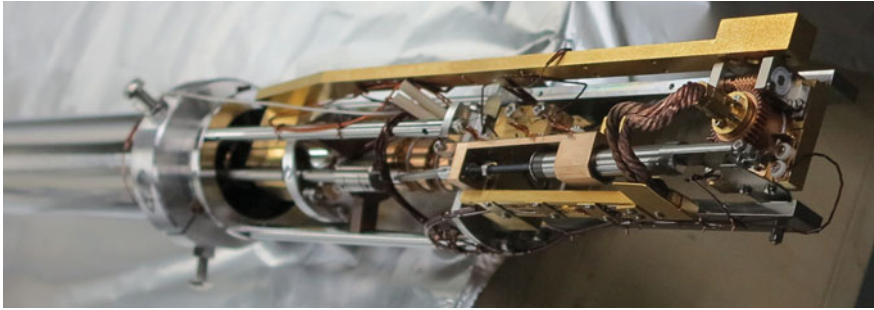


Fig. 3.2 Modified six-axis cryostat with better performance

to detect the electronic structure of the local region on the sample surface. In the following, details of the state-of-the-art ARPES systems developed by our group will be elaborated: 7-eV ultraviolet laser-based ARPES system, tunable laser-based ARPES system, laser-based spin-resolved ARPES system, and laser-based time-of-flight ARPES system (Fig. 3.3).

3.2 Vacuum Ultraviolet Laser-Based ARPES System

Laser with small bandwidth and high intensity has been proposed as an ideal light source for ARPES system for a long time. A key challenge is the photon energy. The Photon energy of the incident beam should be at least larger than the work function of the sample which is 4–5 eV in typical materials. However, the photon energy provided by the commercial laser source is smaller than 4 eV.

To solve this problem, an efficient way to double the frequency of the laser is needed. The KBBF crystal synthesized by Prof. Chen's group at the Technical Institute of Physics and Chemistry [3–6] has brought a new opportunity to us. With KBBF crystal (Fig. 3.4), the wavelength of the commercial laser (~ 355 nm) can be shortened

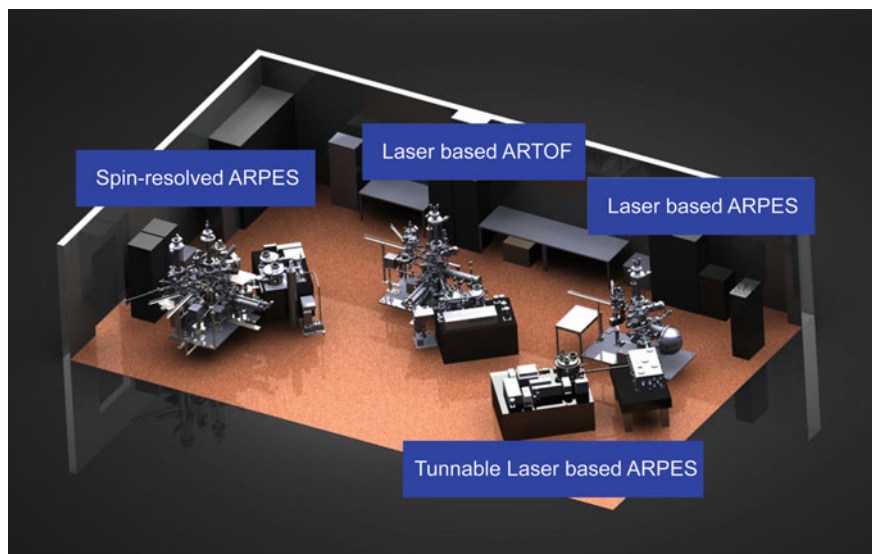


Fig. 3.3 Schematic of the laser-based ARPES systems

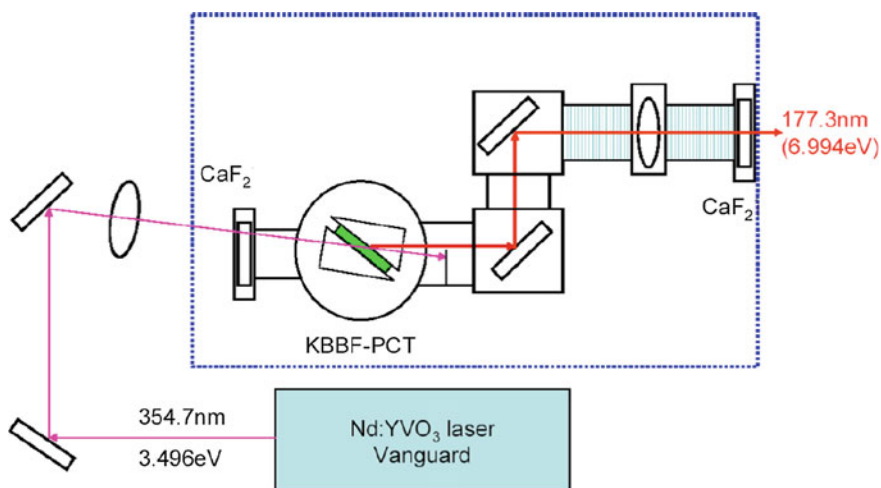


Fig. 3.4 A schematic layout of the VUV laser optical system [2]

into ~ 177 nm [7, 8] such that the photon energy of the laser reaches 6.994 eV, which is larger than the work function of the materials (~ 4 eV). Therefore, we have a ~ 3 eV energy window to detect the electronic structure below Fermi level. In practice, the electron analyzer may not work with its best performance for the electrons with a kinetic energy lower than 1 eV. However, the rest 2 eV energy window is still large enough, because the main electronic structure we care about is within several hundred



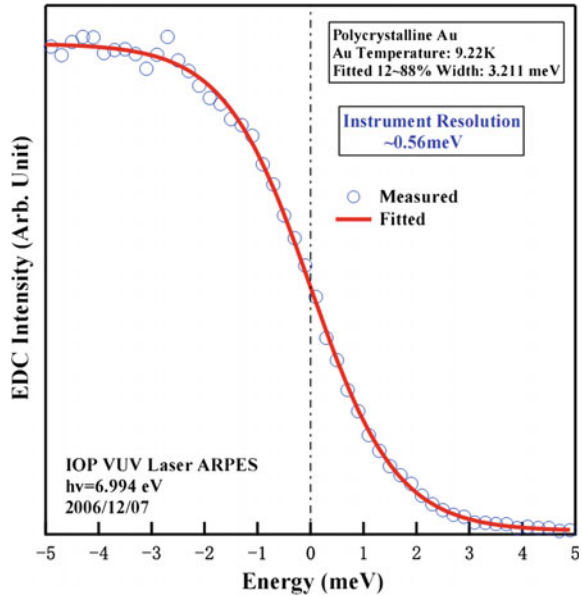
Fig. 3.5 The VUV laser ARPES system

meV below Fermi level. Meanwhile, due to the small bandwidth of the laser (~ 0.26 meV), the overall energy resolution of the system can be lower than 1 meV. Shown in Fig. 3.5 is the ultraviolet laser-based ARPES system developed in our laboratory. The details of the system and the related testing results will be presented below.

3.2.1 Energy Resolution of the System [2]

The direct way to calibrate the energy resolution of the system is to measure the Fermi edge of clean polycrystalline gold at low temperature. The overall width of the measured Fermi edge is composed of three main contributions: 1. energy resolution of the system, 2. temperature broadening, and 3. broadening from a contaminated surface of the gold. Therefore, a clean gold surface is very crucial for a correct calibration. This can be achieved by sputtering with an Ar gun and annealing with a heater installed in the preparation chamber. The upper limit of the energy resolution of the system can be obtained by subtracting the temperature broadening from the Fermi edge width, assuming a perfect sample surface of the gold (the real energy resolution of the system should be better since the surface of the gold cannot be

Fig. 3.6 Energy resolution test of the VUV laser ARPES system by measuring on clean polycrystalline gold. Reprinted with the permission from [2]. Copyright 2008, AIP Publishing LLC



perfect which still contributes to the overall width of the measured Fermi edge). The measurement was taken at 9.22 K with 2 eV pass energy and 0.1-mm slit of the electron analyzer. By fitting the Fermi edge with Fermi distribution function, the 12–88 % width is obtained to be 3.211 meV, as shown in Fig. 3.6. After subtracting the temperature broadening contribution of 3.162 meV, we obtain an overall energy resolution of the system: 0.56 meV [2].

As for the origin of this 0.56 meV energy resolution, there are three main contributions: 1. the line width of the laser (0.26 meV), 2. energy resolution of the analyzer (0.5 meV for 2 eV pass energy and 0.1-mm slit), and 3. contribution of the space charge effect. The convolution of them gives rise to the total resolution of the system. It is evident that by using the ultraviolet laser, the line width of the light source is no longer the bottleneck which limits the overall resolution of the system.

3.2.2 Space Charge Effect Test [2]

The first concern for the utilization of high-flux pulsed laser as the light source for photoemission is the space charge effect that may originate from its high flux and pulsed nature. Generally speaking, if too many photoelectrons are emitted into the vacuum at the same time, the Coulomb interaction between the electrons will change the original velocity of the photoelectrons. Naively, the electrons with larger kinetic energy will be accelerated, whereas those with smaller velocity will be decelerated. If the space charge effect is severe, not only the resolution of the system will be

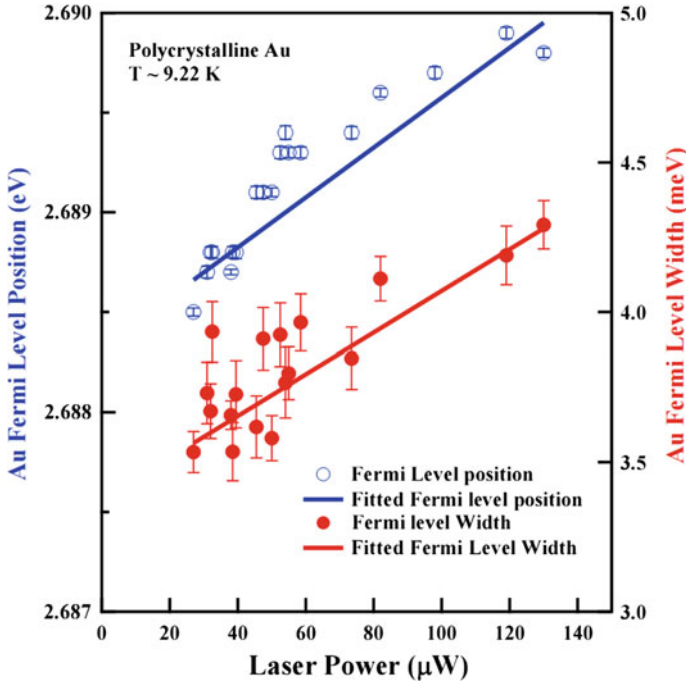


Fig. 3.7 Space charge effect test of the VUV laser ARPES system. Reprinted with the permission from [2]. Copyright 2008, AIP Publishing LLC

affected, but also the measured Fermi level will be shifted. To check on this effect in our laser-based ARPES system, the polycrystalline gold has been measured at a low temperature using different laser powers.

Shown in Fig. 3.7 is the measured Fermi-level position and width as a function of laser power. The Fermi level exhibits nearly 1.5 meV increase when the laser power on the sample goes up to 130 μW , while the corresponding Fermi-level width shows a broadening of less than 1 meV (the laser power of 130 μW corresponds to a photon flux of $\sim 1.1 \times 10^{14}$ photons/s). This clearly demonstrates that there is an observable space charge effect involved in laser photoemission process when the photon flux is high. However, we do not use a laser power of 130 μW for the real experiment. Instead, a laser power of 20–40 μW is typically used which is sufficient for high-quality data. As shown in Fig. 3.7, both the Fermi-level shift and the Fermi-level width broadening are less than 1 meV with this laser power. Therefore, the space charge effect does exist in our laser ARPES system, but it is very weak. In fact, it is much weaker than that observed in synchrotron case [9]. By comparing Fig. 3.7 with Fig. 3.8, we notice that the space charge effect in our laser system is one order of magnitude smaller than that measured with the synchrotron light source. The underlying reasons can be manifold. First, the repetition rate of the laser is very high (on the order of 80–100 MHz), which is essential for minimizing possible space

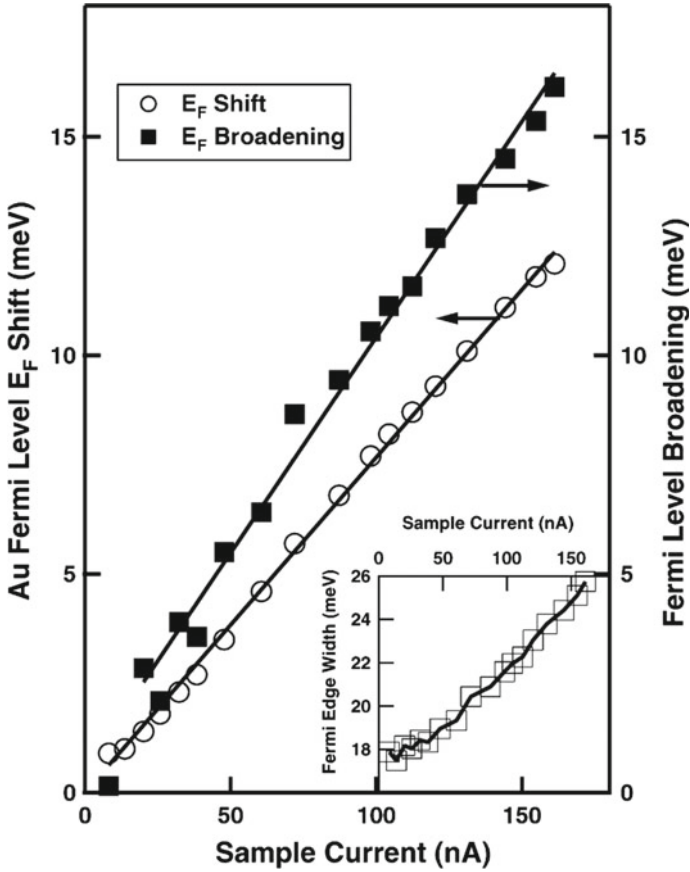


Fig. 3.8 Typical space charge effect of the synchrotron light source. Reprinted from Publication [9], Copyright 2005, with the permission from Elsevier

charge effects. Second, the space charge effect is directly related to the number of emitted electrons. The total number of photoelectrons ejected by the laser is much smaller than that ejected by high-energy synchrotron light source due to the reduced energy and secondary electrons. Third, the space charge effect is actually balanced by the mirror charge effect, and the combined effect relies on the duration of pulse [9]. As indicated in the simulation, the space charge effect and mirror charge effect nearly cancel each other in the range of 1 ~ 10 ps pulse duration, that is, the range of our ultraviolet laser (~10 ps) [9, 10].

3.2.3 Angular Mode and Momentum Resolution Test [2]

The performance of the angular mode is tested using a special “wire-and-slit” device which is composed of a thin wire and a set of slit. Electrons from an electron gun hit the wire, and the scattered electrons pass through the slit and are detected by the analyzer. The spacing between the adjacent two lines in the device is arranged to represent a known emission angle (in our case, 2.5°).

Shown in Fig. 3.9 is the tested result collected at 1, 2, and 5 eV pass energies, respectively, and 30° angular mode with 0.1 mm spot size. A constant dispersion was observed over a wide kinetic energy range, with the lowest limit of ~ 0.5 eV [2]. For the 6.994 eV laser, the highest kinetic energy of the photoelectrons is nearly 2.7 eV with a typical work function of 4.3 eV. As shown in the figure, a very good angular resolution can be constantly obtained for photoelectrons with a kinetic energy larger than 0.5 eV. Therefore, an energy window of ~ 2.2 eV can be used which is very suitable to probe the main electronic structure needed in our research, whose typical binding energy is within several hundred meV below Fermi level.

The angular resolution of the analyzer is also quantitatively tested by moving the wires with very fine steps. The smallest movement that can be resolved by the analyzer determines the best angular resolution. Note that the angular resolution is sensitive to the spot size: The smaller the spot size, the better the angular resolution. Our laser has a spot size of ~ 0.1 mm. However, it is impossible to do the angular resolution test for the 0.1 mm spot size using the same “wire-and-slit” scheme, because the diameter of the wire itself is 0.1 mm. For 0.8 mm spot size, the angular resolution is 0.3° for the 14° angular mode, while it is 0.8° for the 30° angular mode. As stated above, the exact angular resolution is not known for our 0.1 mm laser spot, although its upper limit is estimated to be much less than 0.8° for the 30° angular mode. As

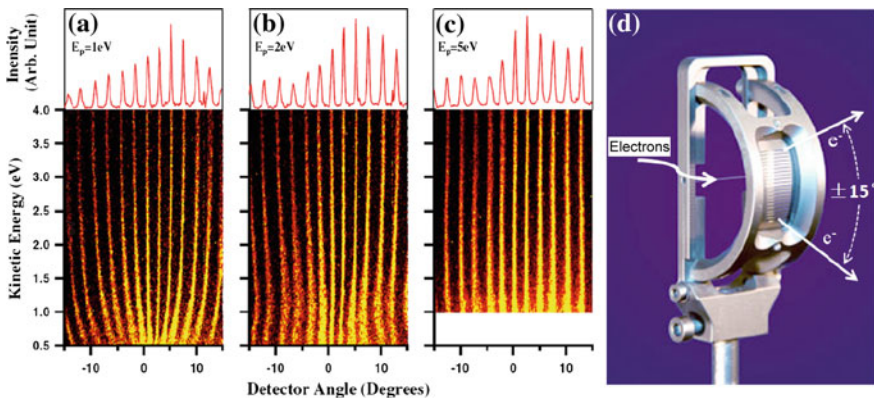


Fig. 3.9 Angle resolution test of the VUV laser ARPES system. The measurements were taken with pass energy of 1 eV (a), 2 eV (b), and 5 eV (c), respectively. d, the Scienta wire-and-slit device. Reprinted with permission from [2]. Copyright 2008, AIP Publishing LLC

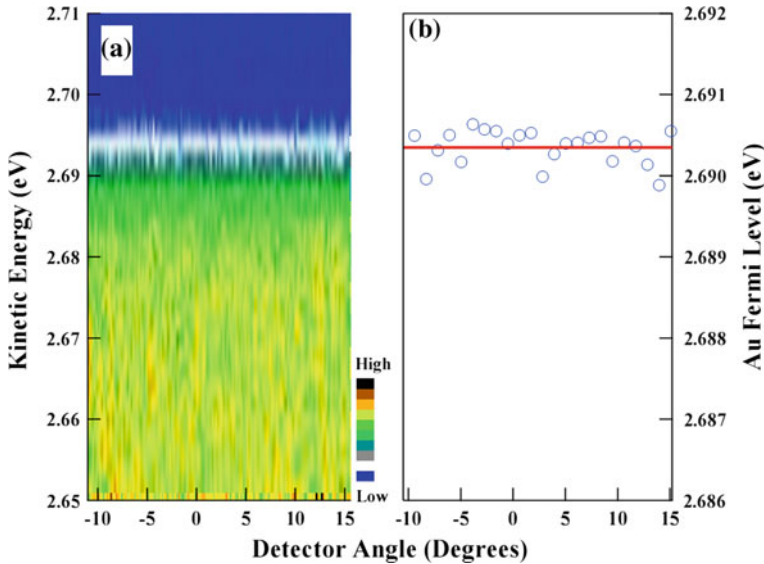


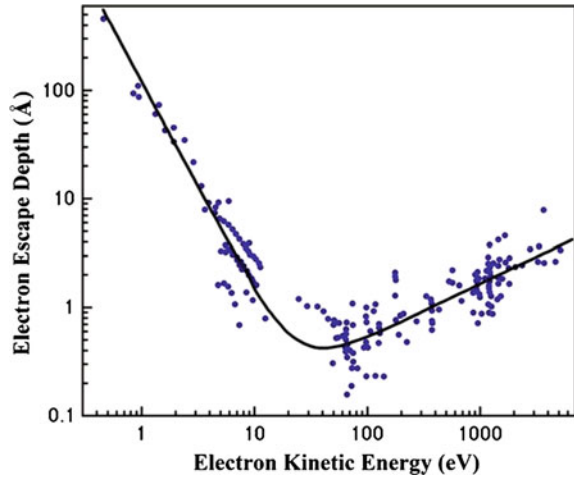
Fig. 3.10 Fermi-level uniformity test. Little variation in the Fermi-level position was found as a function of the detector angle. Reprinted with the permission from [2]. Copyright 2008, AIP Publishing LLC

for the momentum resolution, it is given by $\Delta k = 0.5118\sqrt{h\nu - \Phi} \cdot \cos\theta \Delta\theta$ near the Fermi level, where Δk is the momentum resolution, $\Delta\theta$ the angular resolution, $h\nu$ the photon energy, Φ the work function, and θ the angle with respect to the sample normal. Therefore, compared to most of the synchrotron light source, the low photon energy of the laser gives a better momentum resolution around the Fermi level even for the same angular resolution. Another concern is about the uniformity of the energy across the entire detector angle range. This is particularly important for small-energy-scale measurements which also determine the reliability of the angular mode. This has been examined by measuring the gold Fermi edge at low temperature. Since the photoemission intensity from the polycrystalline gold does not have any angle dependence, one would expect that the Fermi edge positions obtained at different detector angles are the same. Figure 3.10a shows the tested photoemission intensity image using 30° angular mode, and the fitted Fermi edge position as a function of the detector angle is given in Fig. 3.10b. The deviation of the Fermi edge from its average position is less than ± 0.3 meV over the entire angular window, demonstrating a perfect working condition of the angular mode [2].

3.2.4 Bulk Sensitivity Test of the 6.994 eV Laser ARPES [2]

The use of ~ 7 eV laser is expected to greatly enhance the bulk sensitivity in probing the electronic structure of solids. According to the “universal curve” for the

Fig. 3.11 Universal curve for the photoelectron mean free path in metals as a function of the electron kinetic energy [11]



photoelectron mean free path as a function of the electron kinetic energy [11] (Fig. 3.11), the photoelectron mean free path at the present photon energy of ~ 7 eV is larger than 30\AA , whereas an electron escape depth of $< 5\text{\AA}$ was given when using a light source with the photon energy of $20\text{--}50$ eV.

We note that this “universal curve” is for simple metal systems, and whether it is applicable to complex oxide compounds, such as high-temperature superconductors, is not clear yet. While the absolute value of the electron escape depth may vary, one should expect an overall enhancement of bulk sensitivity at lower photon energy. Since it is difficult to carry out quantitative measurement of the electron escape depth, we carried out a qualitative test by measuring $\text{Bi}_2\text{Sr}_2\text{CaCu}_2\text{O}_{8+\delta}$ (Bi2212) single-crystal sample treated at different environments. First, we measured a nearly optimally doped Bi2212 sample along the nodal direction with in situ sample cleavage in the ultrahigh vacuum (Fig. 3.12a). The same cleaved sample was then exposed under 1 atm N_2 for 1 h and remeasured along the same momentum cut, as shown in Fig. 3.12b. Then, the sample was exposed to the air for 1 h and measured again, and the result is shown in Fig. 3.12c. We notice that the three measurements were taken under the same vacuum condition and at the same temperature 17 K. It is clear that the signal becomes weaker when the sample surface becomes dirtier from the exposure to nitrogen and then air. However, the basic band dispersion can still be resolved which is not possible for high photon energy such as $20\text{--}50$ eV. Therefore, the use of ~ 7 eV laser does improve the bulk sensitivity of the measurement.

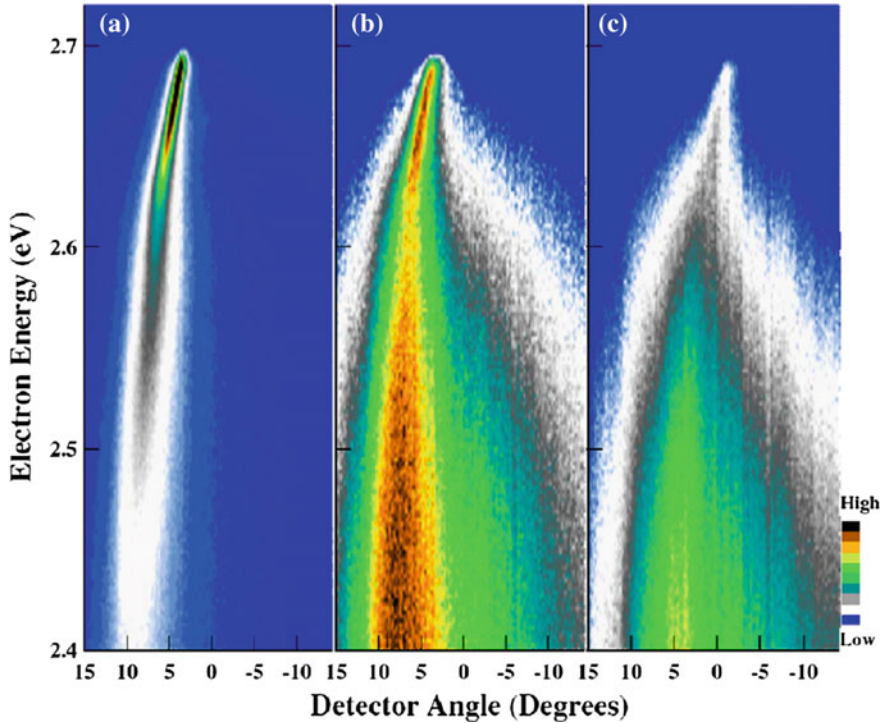


Fig. 3.12 Bulk sensitivity test on a typical Bi2212 sample. **a** The measurement on a Bi2212 sample cleaved in the vacuum. The same cleaved sample was exposed under 1 atm N_2 for 1 h (**b**) and exposed to the air for 1 h (**c**). Reprinted with the permission from [2]. Copyright 2008, AIP Publishing LLC

3.2.5 Modifications on the Helium Discharge Lamp of the ARPES System

As a complementary light source, a helium discharge lamp has been installed in the ARPES system (Fig. 3.13). Photons with two different energies can be produced with sufficient flux: 21.2 and 41.8 eV. However, the commercial helium lamp gives a large spot size with a diameter of ~ 2 mm. If the sample illuminated by the light is smaller than the spot size, then the flux of the incident beam cannot be fully used.

A joint effort has been made between our laboratory and the Scienta company to minimize the spot size without losing flux of the beam. By replacing the original cylindrical capillary (Fig. 3.14a) with the one with a cone shape (Fig. 3.14b), the beam spot is significantly reduced, which shows a diameter of ~ 0.5 mm. Tests performed before and after the modification clearly indicate a better focusing of the beam as well as $\sim 30\%$ improvement in electron counting without any other change. The efficiency of the helium lamp has been greatly improved which in turn guarantees a high quality of the experimental data.

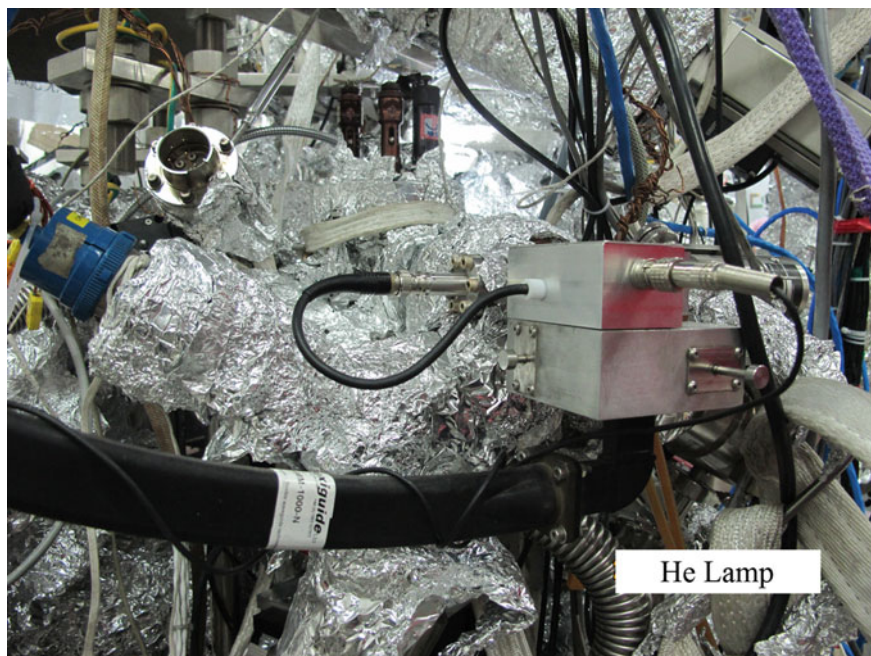


Fig. 3.13 Helium lamp for the ARPES system

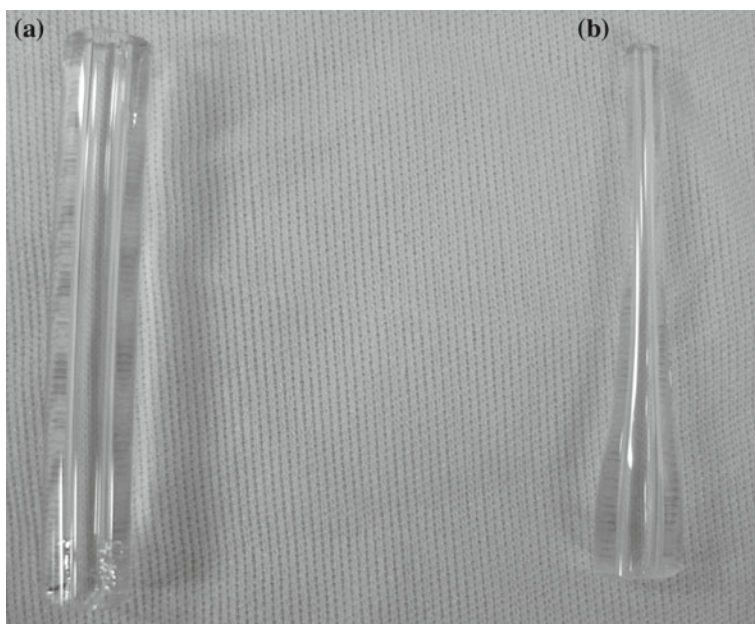


Fig. 3.14 **a** Traditional cylindrical capillary. **b** The modified capillary

3.3 Tunable Laser-Based ARPES System

The 7 eV laser has many advantages as a light source. It gives rise to high energy resolution, high momentum resolution, and high photon flux and enhances bulk sensitivity in probing the electronic structures. However, it also has disadvantages compared to the synchrotron light source. One major problem is the fixed photon energy, as elaborated in the last chapter that photons with different energies can probe the electronic band structures with different K_z in the material. When the material is not pure 2D, the measurement with a fixed photon energy cannot capture all the electronic bands. Moreover, the ARPES matrix element effect is also related to the photon energy. It is possible that some electronic structures cannot be detected by photons with a fixed energy due to the matrix element effect [12]. Therefore, a laser source with tunable photon energy will be very helpful. Collaborating with Prof. Chen and Prof. Xu's groups at the Technical Institute of Physics and Chemistry, we developed the first tunable vacuum ultraviolet laser-based ARPES system with a photon energy range of 5.90–7.09 eV (Fig. 3.15).

Shown in Fig. 3.16 are the testing results on a Bi2212 sample. The measurements were taken along the same momentum cut with different photon energies. With all the other conditions fixed, different bands were observed (or enhanced) by different photon energies. It has clearly demonstrated that new structures, which were not seen

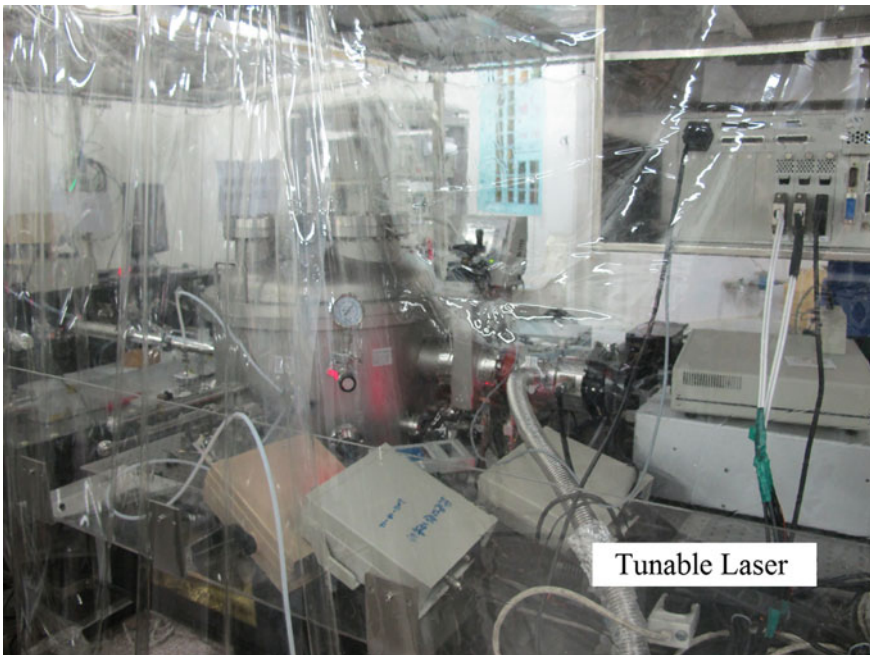


Fig. 3.15 Tunable laser ARPES system

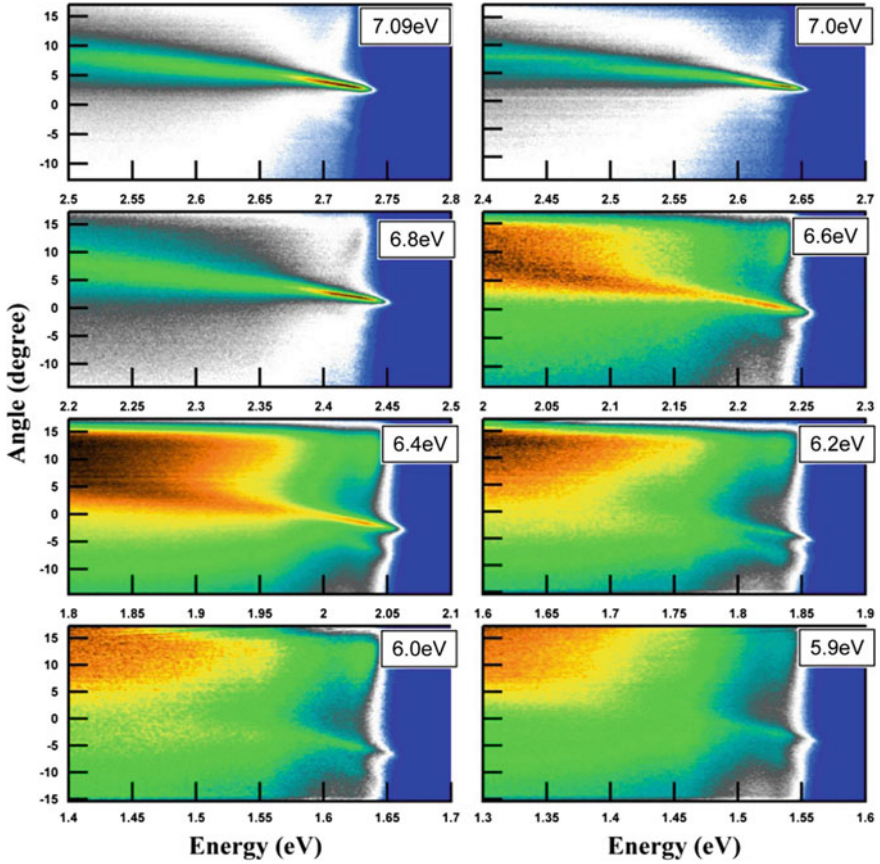


Fig. 3.16 Test measurement on Bi2212 with different photon energies

when utilizing 7 eV laser, can be clearly resolved when the photon energy is changed. The tunability of the laser source has added a significant piece to its application. In particular, it will be very useful when a broad characterization of the electronic structure is needed.

3.4 Spin-Resolved Laser-Based ARPES System

In quantum mechanics, the electron is fully described by energy ω , momentum k , and spin s . In the normal ARPES measurements, only the electron energy ω and momentum k can be detected. However, in some advanced materials, the spin plays a very important role which dictates the physical properties of the materials. For example, the Rashba splitting in the surface state of single-crystal metal [13] and the

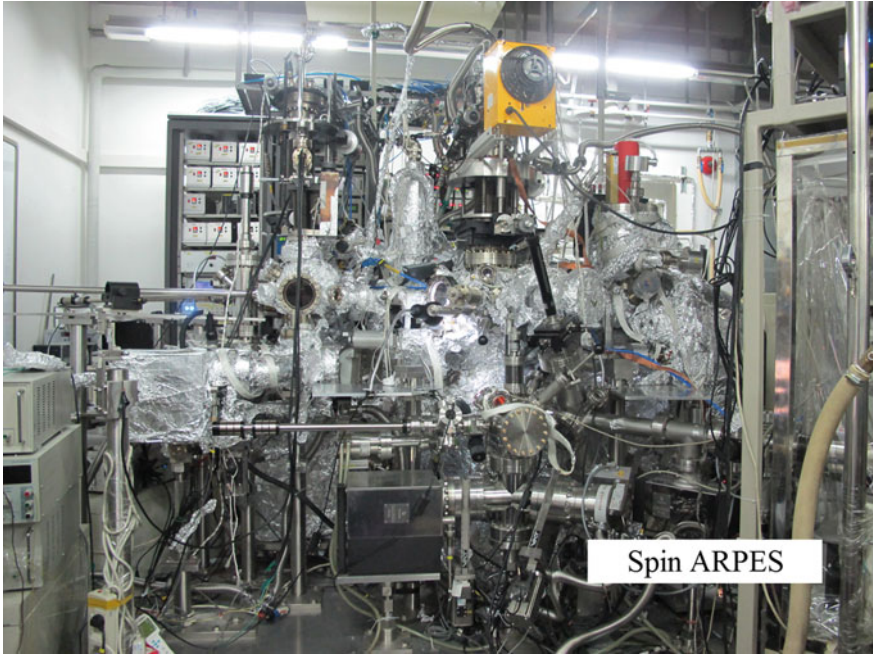


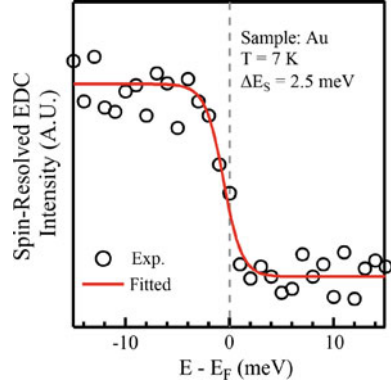
Fig. 3.17 Spin-resolved laser-based ARPES system

physical phenomena observed in the topological insulators [14] are closely related to the spin of the materials. Therefore, the spin-resolved ARPES is a very important experimental tool. However, the best energy resolution for the synchrotron-based spin-resolved ARPES is ~ 80 meV, which is not very good compared to that of the standard ARPES systems. A major reason is the low efficiency of the spin detector. In order to get the same intensity as that of the standard ARPES, the flux of the incident beam has to be greatly increased. However, this will in turn increase the line width of the synchrotron beam and thus limit the total resolution of the spin-resolved ARPES.

The laser light source shows its unique advantage in solving this problem. As a delta function in photon energy, the laser keeps its line width free from the change of photon flux. Therefore, the high photon flux does not limit the resolution of the laser. Meanwhile, as discussed earlier, the laser shows a smaller space charge effect than the synchrotron which is also very good for the application with high photon flux. Shown in Fig. 3.17 is the laser-based spin-resolved ARPES system developed in our laboratory. By using laser, the best energy resolution in our system is ~ 2.5 meV, as shown in Fig. 3.18, which is ~ 2 orders of magnitude better than the best energy resolution achievable in other spin-resolved systems.

Many different types of spin detectors have been developed in the past several decades. Most of them are based on Mott scattering [16–21], diffuse scattering

Fig. 3.18 Energy resolution of the spin-resolved ARPES system [15]



[22, 23], low-energy electron scattering [24], and spin-dependent scattering on the magnetic films. The spin detector used in our system is the Mott detector whose mechanism will be elaborated below.

Due to the spin-orbit coupling, the Mott scattering of electrons with different spins is asymmetric in space. By measuring this asymmetry, people can in turn detect the spin polarization of the materials. The scattering cross section $\sigma(\theta)$ of the incident electrons with the spin polarization \mathbf{P} can be written as follows:

$$\sigma(\theta) = I(\theta)[1 + S(\theta)\mathbf{P} \cdot \mathbf{n}] \quad (3.1)$$

where θ is the scattering angle, $I(\theta)$ is the scattering intensity without spin-orbit coupling, \mathbf{n} is the normal of the scattering plane, and $S(\theta)$ is called Sherman function which is related to the atomic number Z , the scattering angle θ , and the energy.

Shown in Fig. 3.19 is the Mott scattering process. The solid lines indicate the plain Coulomb potential of a nucleus, whereas the dashed lines show the spin-dependent potential due to the spin-orbit interaction [25]. Therefore, the polarization \mathbf{P} of the incident electron beam can be obtained by detecting the different intensities between the left and right channels:

$$\mathbf{P} = \frac{1}{S} \frac{I_R - I_L}{I_R + I_L} \quad (3.2)$$

where I_L and I_R are the scattered electron intensities on the left and right detectors, respectively.

In our spin-resolved ARPES system, double-Mott detectors are used which can give a full measurement of the spin polarizations. As shown in Fig. 3.20a, the incident electrons are split into two Mott detectors which are perpendicular to each other. Each Mott detector has four channeltrons and can therefore detect the polarization with respect to two axes independently. The detector installed along z-axis measures the polarization along x-axis (P_x) and y-axis (P_y), and the one installed along x-axis captures P_y and P_z . With the double-Mott detectors, people can measure P_y twice simultaneously. Consistent results of P_y from different detectors can be used to

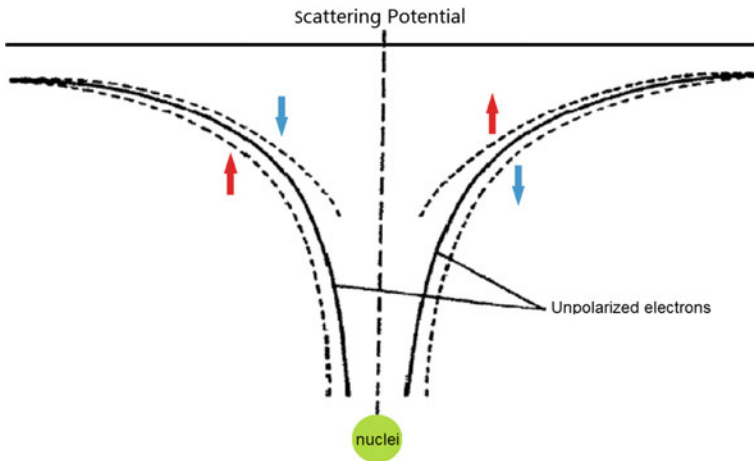


Fig. 3.19 Schematic of the Mott scattering

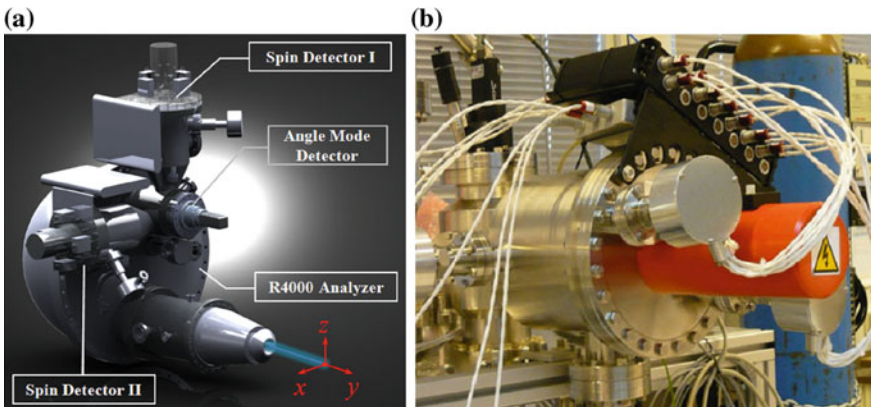


Fig. 3.20 Double-Mott detectors. **a** Schematic of the double-Mott detectors. **b** The Mott detector in the ARPES system

guarantee the solidity of the measurements. Shown in Fig. 3.20b is the Mott detector installed in our system.

The spin-resolving capability of our system is demonstrated by measuring a standard sample Au(111) (Fig. 3.21). Due to the Rashba effect, the surface state of Au(111) splits into two branches of bands with well-defined spin polarization. As shown in the left panel, the two branches are clearly observed. Simultaneous measurements by the four channeltrons in the spin detector give four spin-resolved photoemission spectra (EDCs) shown in the right panel for the momentum point marked by the dashed blue line. Two peaks are well resolved in our spin-resolved EDCs. The two EDCs from the left and right channels show obvious difference in their intensity

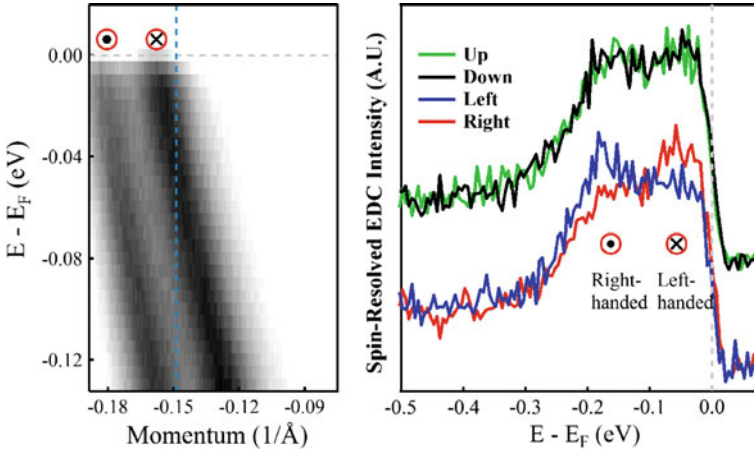


Fig. 3.21 Measurements on Au. *Left panel* the surface state of Au. *Right panel* the spin-resolved EDCs. The momentum point of the EDCs is marked by the *blue dashed line* in the *left panel* [15]

at two peak positions. Moreover, the relative intensity from these two channels is opposite for the two peaks which indicates that there is spin polarization in the plane of the Au(111) surface and the spin polarization directions for the two branches of bands are opposite. On the other hand, there is little difference between the two EDCs from the up and down channels (green and black curves), indicating a negligible spin polarization of the out-of-plane component. This is the first time that two peaks can be well resolved in the spin-resolved raw EDCs, due to much improved energy and angular resolutions. This direct observation has also enhanced the solidity of the experiment compared to the fitting procedure which was used to deduce the two peaks from a broad hump.

3.5 Time-of-Flight System

The second-generation hemispheric analyzer (e.g., R4000) measures a momentum line at a time by using a slit in front of the analyzer. Compared to the first-generation point detector, the second-generation analyzer has greatly improved the efficiency of the measurements. Moreover, the detection of a momentum line enables the analysis of momentum distribution curve (MDC) of the spectra, which has played an important role in the recent research. A natural expectation for the next generation of analyzer is a 3D detector which measures an area in the momentum space simultaneously. This has been first realized by the time-of-flight analyzer (ARTOF) produced by Scienta company in which the energy of the electron is characterized by the time it takes to fly from the sample surface to the detector. Therefore, the horizontal and vertical axes of the MCP at the end of the detector can be used to measure K_x and

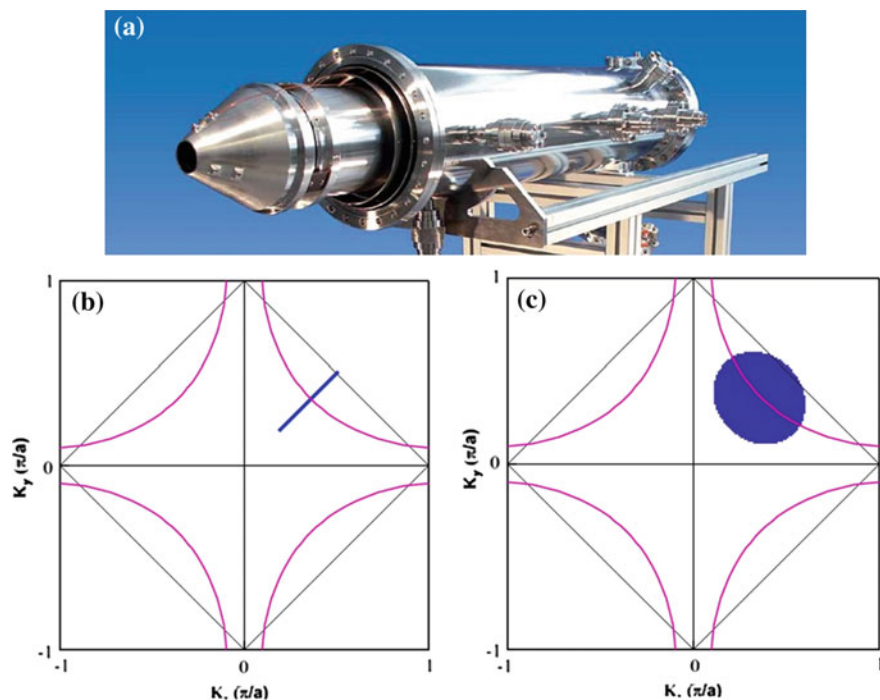


Fig. 3.22 ARTOF and the momentum region covered by different analyzers. **a** ARTOF analyzer. **b** R4000 measures one momentum cut at one time. **c** ARTOF covers an area in the momentum space

K_y , respectively, which enables the measurement of an area in the momentum space. As shown in Fig. 3.22, when the momentum area of one measurement is concerned, the efficiency of the ARTOF analyzer has been improved by 250 times compared to that of the typical R4000 analyzer.

Shown in Fig. 3.23 is the ARTOF system developed in our laboratory. A typical Bi2212 sample was measured to demonstrate the function of the system. The Fermi surface of the sample was obtained by real-time display (Fig. 3.24) which can never be realized by the second-generation detectors. The use of area detector has also reduced the ARPES matrix element effect. Meanwhile, ARTOF records each photoelectron as an event such that the nonlinear effect can be avoided.

Of course, ARTOF also has its disadvantages. Since the energy of the photoelectron is measured by the time it flies, a prerequisite for the measurement is that no photoelectron comes out before the earlier set of electrons reach the detector. This requires a pulsed light source and makes others (e.g., gas discharge lamp) incompatible with the system. Fortunately, our vacuum ultraviolet laser is a pulsed light source. A rough estimation by considering the photon energy (7 eV) and a work function of ~ 4 eV would give rise to ~ 3 eV kinetic energy for the photoelectrons. Since the distance between the sample and the ARTOF detector (MCP) is ~ 1 m, the

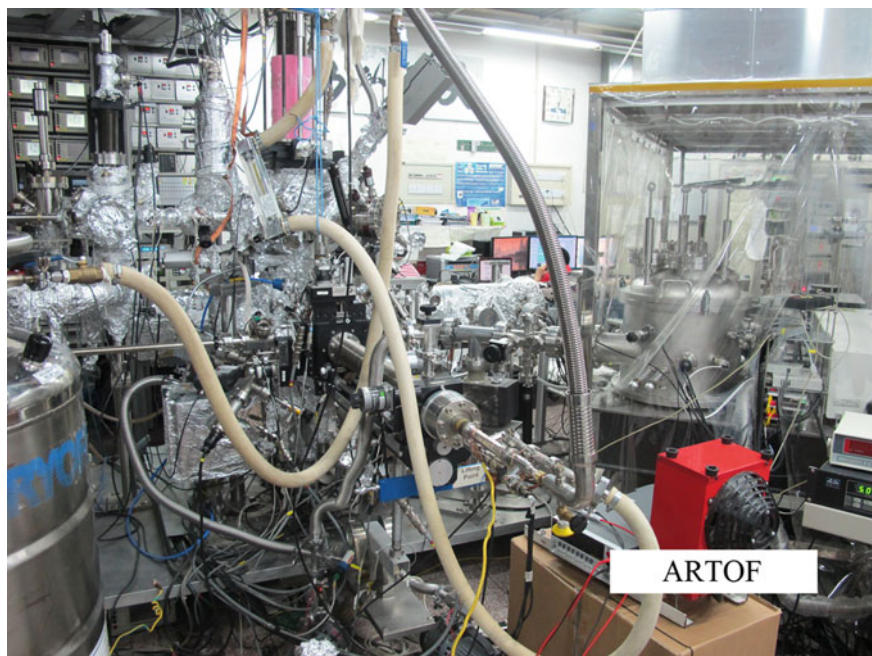
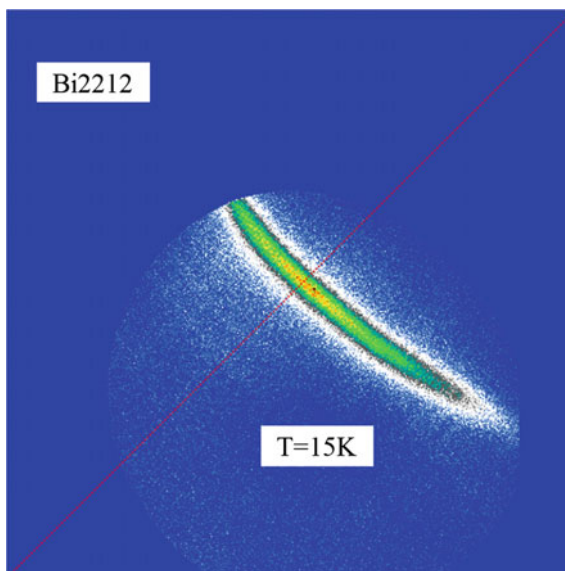


Fig. 3.23 ARTOF system

Fig. 3.24 Measurements on Bi2212 by ARTOF: The Fermi surface can be obtained by real-time display



flying time of the photoelectrons should be in the order of microsecond. Therefore, the repetition rate of the laser should be smaller than 1 MHz. If we keep the power of the laser as that of the 80 MHz laser used with R4000 analyzer, the total number of photons in each pulse has to be greatly improved. However, this number is limited by the space charge effect as described before. Although the space charge effect caused by the laser is generally smaller than that of the synchrotron, the increase of photons by ~ 100 time per pulse would induce considerable space charge effect. Therefore, the power of the laser used for ARTOF is actually lower than that for R4000 system, which of course reduces the efficiency of the measurement. Nevertheless, the 3D character of the ARTOF system is still appealing which will make it more popular in the future.

References

1. Damascelli, A., Hussain, Z., Shen, Z.-X.: Angle-resolved photoemission studies of the cuprate superconductors. *Rev. Mod. Phys.* **75**, 473–541 (2003)
2. Liu, G., Wang, G., Zhu, Y., Zhang, H., Zhang, G., Wang, X., Zhou, Y., Zhang, W., Liu, H., Zhao, L., Meng, J., Dong, X., Chen, C., Xu, Z., Zhou, X.J.: Development of a vacuum ultraviolet laser-based angle-resolved photoemission system with a superhigh energy resolution better than 1 meV. *Rev. Sci. Instrum.* **79**(2), 023105 (2008)
3. Chen, C., Xu, Z., Deng, D., Zhang, J., Wong, G.K.L., Wu, B., Ye, N., Tang, D.: The vacuum ultraviolet phase-matching characteristics of nonlinear optical $\text{KBe}_2\text{BO}_3\text{F}_2$ crystal. *Appl. Phys. Lett.* **68**(21), 2930–2932 (1996)
4. Chen, C., Lu, J., Togashi, T., Sugauma, T., Sekikawa, T., Watanabe, S., Xu, Z., Wang, J.: Second-harmonic generation from a $\text{KBe}_2\text{BO}_3\text{F}_2$ crystal in the deep ultraviolet. *Opt. Lett.* **27**(8), 637–639 (2002)
5. Togashi, T., Kanai, T., Sekikawa, T., Watanabe, S., Chen, C., Zhang, C., Xu, Z., Wang, J.: Generation of vacuum-ultraviolet light by an optically contacted, prism-coupled $\text{KBe}_2\text{BO}_3\text{F}_2$ crystal. *Opt. Lett.* **28**(4), 254–256 (2003)
6. Kanai, T., Kanda, T., Sekikawa, T., Watanabe, S., Togashi, T., Chen, C., Zhang, C., Xu, Z., Wang, J.: Generation of vacuum-ultraviolet light below 160 nm in a KBBF crystal by the fifth harmonic of a single-mode Ti: sapphire laser. *J. Opt. Soc. Am. B* **21**(2), 370–375 (2004)
7. Kiss, T., Kanetaka, F., Yokoya, T., Shimojima, T., Kanai, K., Shin, S., Onuki, Y., Togashi, T., Zhang, C., Chen, C.T., Watanabe, S.: Photoemission spectroscopic evidence of gap anisotropy in an f -electron superconductor. *Phys. Rev. Lett.* **94**, 057001 (2005)
8. Kiss, T., Shimojima, T., Kanetaka, F., Kanai, K., Yokoya, T., Shin, S., Onuki, Y., Togashi, T., Zhang, C.Q., Chen, C.T., Watanabe, S.: Ultrahigh-resolution photoemission spectroscopy of superconductors using a VUV laser. *J. Electron Spectrosc. Relat. Phenom.* **1**, 44–147, 953–956 (2005)
9. Zhou, X.J., Wannberg, B., Yang, W.L., Brouet, V., Sun, Z., Douglas, J.F., Dessau, D., Hussain, Z., Shen, Z.X.: Space charge effect and mirror charge effect in photoemission spectroscopy. *J. Electron Spectrosc. Relat. Phenom.* **142**(1), 27–38 (2005)
10. Zhang, W.T.: A study of $\text{Bi}_2\text{Sr}_2\text{CaCu}_2\text{O}_8$ by laser-based angle-resolved photoemission. Springer Theses Recognizing Outstanding Ph.D. Research. (2012). doi:[10.1007/978-3-642-32472-7](https://doi.org/10.1007/978-3-642-32472-7)
11. Seah, M.P., Dench, W.A.: Quantitative electron spectroscopy of surfaces: a standard data base for electron inelastic mean free paths in solids. *Surf. Interface Anal.* **1**(1), 2–11 (1979)
12. Iwasawa, H., Douglas, J.F., Sato, K., Masui, T., Yoshida, Y., Sun, Z., Eisaki, H., Bando, H., Ino, A., Arita, M., Shimada, K., Namatame, H., Taniguchi, M., Tajima, S., Uchida, S., Saitoh, T.,

- Dessau, D.S., Aiura, Y.: Isotopic fingerprint of electron-phonon coupling in high- T_c cuprates. *Phys. Rev. Lett.* **101**, 157005 (2008)
13. Bratkovsky, A.M.: Spintronic effects in metallic, semiconductor, metal-oxide and metal-semiconductor heterostructures. *Rep. Prog. Phys.* **71**(2), 026502 (2008)
 14. Hsieh, D., Xia, Y., Wray, L., Qian, D., Pal, A., Dil, J.H., Osterwalder, J., Meier, F., Bihlmayer, G., Kane, C.L., Hor, Y.S., Cava, R.J., Hasan, M.Z.: Observation of unconventional quantum spin textures in topological insulators. *Science* **323**(5916), 919–922 (2009)
 15. Xie, Z., He, S., Chen, C., Feng, Y., Yi, H., Liang, A., Zhao, L., Mou, D., He, J., Peng, Y., Liu, X., Liu, Y., Liu, G., Dong, X., Yu, L., Zhang, J., Zhang, S., Wang, Z., Zhang, F., Yang, F., Peng, Q., Wang, X., Chen, C., Xu, Z., Zhou, X.J.: Orbital-selective spin texture and its manipulation in a topological insulator. *Nat. Commun.* **5**, 3382 (2014)
 16. Kisker, E., Clauberg, R., Gudat, W.: Electron spectrometer for spin-polarized angle-and energy-resolved photoemission from ferromagnets. *Rev. Sci. Instrum.* **53**(8), 1137–1144 (1982)
 17. Gray, L.G., Hart, M.W., Dunning, F.B., Walters, G.K.: Simple, compact, medium-energy Mott polarization analyzer. *Rev. Sci. Instrum.* **55**(1), 88–91 (1984)
 18. Raue, R., Hopster, H., Kisker, E.: High-resolution spectrometer for spin-polarized electron spectroscopies of ferromagnetic materials. *Rev. Sci. Instrum.* **55**(3), 383–388 (1984)
 19. Tang, F.-C., Zhang, X., Dunning, F.B., Walters, G.K.: Compact low-energy Mott polarimeter for use in energy- and angle-resolved polarization studies. *Rev. Sci. Instrum.* **59**(3), 504–505 (1988)
 20. Gay, T.J., Dunning, F.B.: Mott electron polarimetry. *Rev. Sci. Instrum.* **63**(2), 1635–1651 (1992)
 21. Burnett, G.C., Monroe, T.J., Dunning, F.B.: High-efficiency retarding-potential Mott polarization analyzer. *Rev. Sci. Instrum.* **65**(6), 1893–1896 (1994)
 22. Scheinfein, M.R., Unguris, J., Kelley, M.H., Pierce, D.T., Celotta, R.J.: Scanning electron microscopy with polarization analysis (SEMPA). *Rev. Sci. Instrum.* **61**(10), 2501–2527 (1990)
 23. Klebanoff, L.E., Van Campen, D.G., Pouliot, R.J.: Electron spin detector for spin-resolved X-ray photoelectron spectroscopy. *Rev. Sci. Instrum.* **64**(10), 2863–2871 (1993)
 24. Sawler, J., Venus, D.: Electron polarimeter based on spin-polarized low-energy electron diffraction. *Rev. Sci. Instrum.* **62**(10), 2409–2418 (1991)
 25. Jozwiak, C.M.: A new spin on photoemission spectroscopy. Ph.D. thesis. University of California, Berkeley (2008)

Chapter 4

Coexistence of Two Sharp-Mode Couplings in $\text{Bi}_2\text{Sr}_2\text{CaCu}_2\text{O}_{8+\delta}$

By using the vacuum ultraviolet laser-based ARPES system, we have performed high-resolution angle-resolved photoemission measurements on $\text{Bi}_2\text{Sr}_2\text{CaCu}_2\text{O}_{8+\delta}$ (Bi2212) superconductors to investigate momentum dependence of electron coupling with collective excitations. Two coexisting energy scales are clearly revealed over a large momentum space for the first time in the superconducting state of the over-doped Bi2212 superconductor. Distinct momentum dependence has been identified for these two energy scales: One keeps its energy near 78 meV over a large momentum space while the other changes its energy from ~ 40 meV near the antinodal region to ~ 70 meV near the nodal region. These observations clearly indicate that electrons are coupled with two sharp modes simultaneously over a large momentum space in the superconducting states which naturally explains the relationship between the nodal and the antinodal kinks. The unusual momentum dependence of the two modes also poses a challenge to our current understanding of electron–mode coupling and its role for high-temperature superconductivity in cuprate superconductors.

4.1 Introduction

The physical properties of materials are determined by the electronic structure that relies on the many-body effects including the electron interactions with other excitations. In particular, the superconductivity of materials involves interaction between electrons which gives rise to electron pairing [1] and this electron–electron interaction might be directly or indirectly mediated by an exchange of a collective excitation. Understanding such many-body effects is key to unraveling the anomalous normal-state properties and superconductivity mechanism in high-temperature cuprate superconductors. Angle-resolved photoemission spectroscopy (ARPES), with its dramatically improved resolutions, has become a powerful tool to directly probe many-body effects in cuprate superconductors [2–4]. Among these observations is the prominent report of a dispersion kink along the $(0,0)–(\pi,\pi)$ nodal

direction. This nodal kink is found to be at ~ 70 meV which is ubiquitous in different materials, different doping levels and at temperatures both above and below the superconducting transition [5–10]. On the other hand, near the $(\pi, 0)$ antinodal region, a clear dispersion kink at ~ 40 meV has also been identified [11–15]. In addition to the origin of the nodal 70 meV kink and the antinodal 40 meV kink that remain under debate (magnetic, phononic, or others), a long-standing puzzle to be resolved is their relationship. In particular, how does the 70 meV nodal kink evolve into the antinodal 40 meV kink when the momentum gradually moves from the nodal to the antinodal regions? Therefore, investigation of the momentum dependence of the electron interaction is critical in understanding the electron pairing in high-temperature superconductors [16–18].

4.2 Materials and Methods

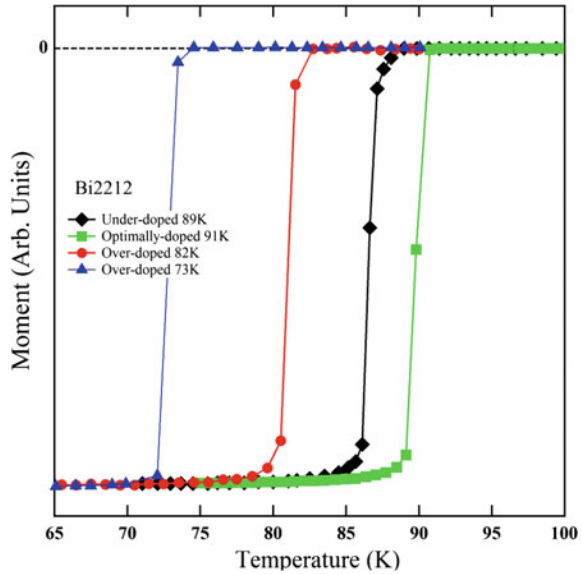
The angle-resolved photoemission measurements were carried out on our vacuum ultraviolet laser-based angle-resolved photoemission system [19]. The photon energy of the laser was 6.994 eV with a bandwidth of 0.26 meV and the energy resolution of the electron energy analyzer (Scienta R4000) was set at 1 meV, giving rise to an overall energy resolution of ~ 1.0 meV. The angular resolution was $\sim 0.3^\circ$, corresponding to a momentum resolution $\sim 0.004 \text{ \AA}^{-1}$ at the photon energy of 6.994 eV. The base pressure of the measurement chamber is better than $5 \times 10^{-11} \text{ Torr}$.

The high-quality $\text{Bi}_2\text{Sr}_2\text{CaCu}_2\text{O}_{8+\delta}$ (Bi2212) single crystals were all cleaved in vacuum right before the measurements. These samples include a slightly underdoped sample with a transition temperature of 89 K (for simplicity, we will call this sample as UD89K hereafter), an optimally doped sample with a transition temperature of 91 K (Opt91 K), and two overdoped samples with transition temperatures of 82 K (OD82K) and 73 K (OD73K), respectively. The optimally doped single-crystal sample was grown by the traveling solvent floating-zone method. The OD82K sample was prepared by annealing the optimally doped sample at 450 K in flowing oxygen atmosphere for two days. The OD73K sample was obtained by annealing in high-pressure oxygen. The annealing process was carried out in a special furnace with an oxygen pressure of 8.5 MPa. The annealing time has also been optimized (3 days) to get the best transition. The magnetic measurements are shown in Fig. 4.1 in which the sharp superconducting transition with a transition width of ~ 2 K can be clearly observed for all the samples.

4.3 Observation of Two Coexisting Energy Features

Figure 4.2 shows the photoemission data on the Bi2212 OD82K sample measured along an off-nodal momentum cut at 17 K. Due to the improved resolution of the laser ARPES, two coexisting features have been identified for the first time. Second-

Fig. 4.1 Magnetic measurements on Bi2212



derivative images (Fig. 4.2b for OD82K sample and Fig. 4.2c for OD73K sample) are used to enhance the visibility of band structures. Two discontinuities are clearly observed from the spectral weight distribution of the main band, accompanied by two white lines (spectral peaks) on both the left and right sides of the main band. Quantitative dispersion is obtained from fitting the momentum distribution curves (MDCs) as shown in Fig. 4.2e. By subtracting a straight line as an empirical bare band (red dashed line in Fig. 4.2e), we can get the effective real part of electron self-energy $\text{Re}\Sigma$ (Fig. 4.2f for both OD82K and OD73K). Two peaks emerge in $\text{Re}\Sigma$: one strong peak at ~ 50 meV and the other weak one near 78 meV.

Signatures of these two features can also be discerned from the corresponding MDC width which is proportional to the imaginary part of the electron self-energy. By subtracting a straight line, the two features in the MDC width can be clearly seen (Fig. 4.2g for OD82K sample). Meanwhile, the photoemission energy distribution curves (EDCs) (Fig. 4.2h, i for OD82K and OD73K samples, respectively) show clear multiple “peak-dip-hump” structure with two dips that are revealed for the first time. The peaks are 5–10 % of the background likely to be beyond any of its variation. For convenience, we call hereafter the feature at ~ 50 meV as the LW energy feature, while the other one at ~ 78 meV as the HI energy feature. It is evident that these two energy features exist in both samples although their relative intensity varies with doping that the HI energy feature is more obvious in the OD73K sample.

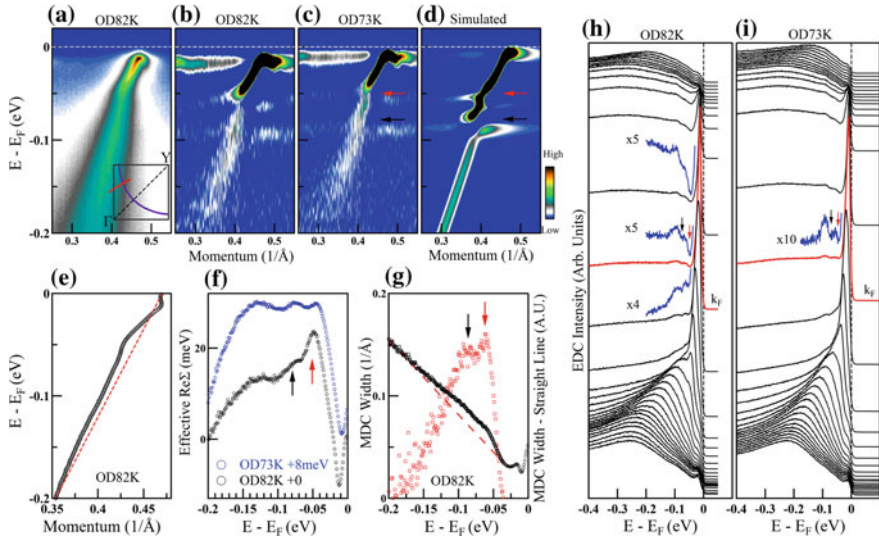


Fig. 4.2 Coexistence of two energy scales in Bi2212. **a** Photoemission image measured at 17 K for OD82K sample. Second-derivative image with respect to energy for OD82K (**b**) and OD73K (**c**). **d** Second-derivative image of the simulated spectra considering electron coupling with two Einstein bosonic modes at 50 and 78 meV. **e** Dispersion for OD82K sample. **f** Effective real part of the electron self-energy for OD82K and OD73K samples. **g** MDC width for OD82K sample and the corresponding difference by subtracting a straight line. Photoemission spectra (EDCs) for OD82K (**h**) and OD73K (**i**). Reprinted with the permission from [20]. Copyright 2013 by the American Physical Society

4.4 Momentum Dependence of the Energy Features

Detailed momentum-dependent ARPES measurements have been carried out on OD82K sample to investigate how the two energy features evolve from the nodal to antinodal regions. Figure 4.3a1–a5 shows the measured data along five momentum cuts; their corresponding EDC second-derivative data are shown in Fig. 4.3b1–b5. Except for the nodal cut 1 where the two energy features are too close to be distinguished (Fig. 4.3b1), the two coexisting energy features are clear in all the other images [Fig. 4.3b2–b5]. Two dip features are also clear in EDCs at the Fermi momenta for all the cuts except for the nodal one because the two energy features become too close (Fig. 4.3c). The two energy features can also be identified in the effective real part of electron self-energy (Fig. 4.3d). It is interesting that the LW and HI energy features exhibit different momentum dependences. Figure 4.3e summarizes the position of these two energy features determined from the peak position of the effective real part of electron self-energy ($\text{Re}\Sigma$) (Fig. 4.3d) and the dip position in the corresponding EDCs (Fig. 4.3c). The HI energy feature stays ~ 78 meV and varies little with momentum, while the LW energy feature varies obviously with momentum,

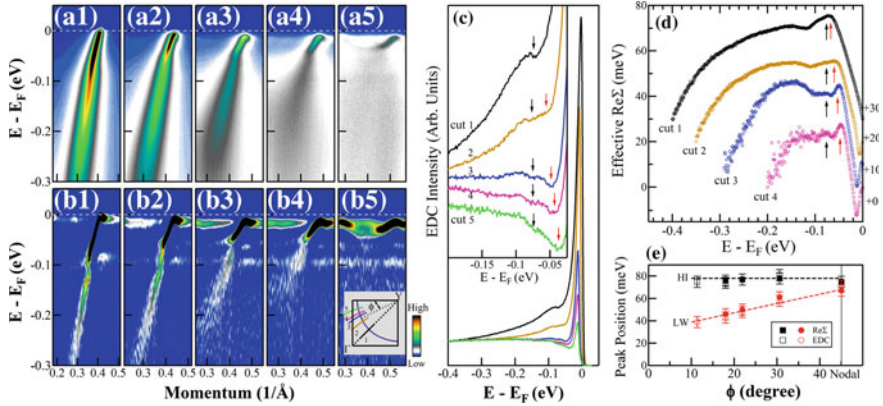


Fig. 4.3 Momentum dependence of the two energy features. **a1–a5** Photoemission images measured along five momentum cuts at 17 K. **b1–b5** Corresponding EDC second-derivative images. **c** EDCs at the Fermi momenta k_F of these five cuts. **d** Effective real part of electron self-energy of the cut 1 to cut 4. **e** Momentum dependence of the two energy features. Reprinted with the permission from [20]. Copyright 2013 by the American Physical Society

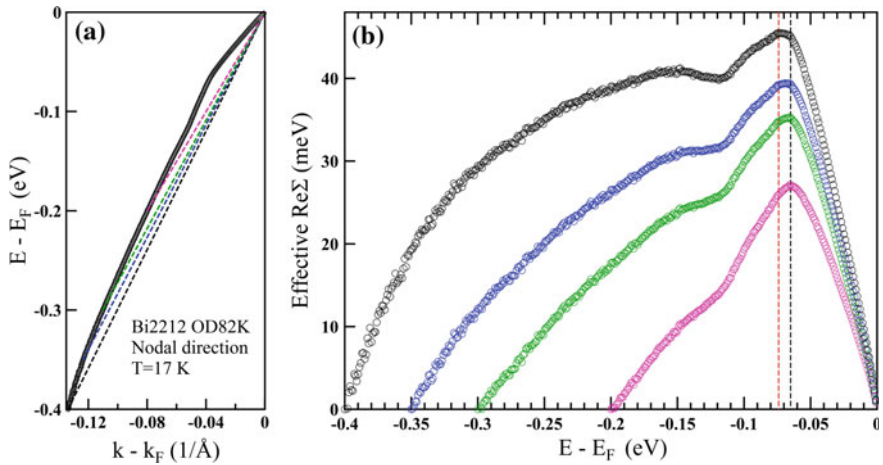


Fig. 4.4 Effect of the energy window selection of the bare band on the identification of energy scales in the real part of electron self-energy. **a** Different energy window selections of the bare band. **b** The corresponding real part of electron self-energy

dropping from ~ 67 meV for the nodal cut to ~ 40 meV (for $\Phi \sim 12^\circ$ cut) near the antinodal region.

Meanwhile, in order to check whether the selection of different bare bands would influence the identification of energy features in electron self-energy, we chose several bare bands with different energy windows for a nodal measurement for the Bi2212 OD82K sample, as shown in Fig. 4.4a. The corresponding effective real part

of electron self-energy is plotted in Fig. 4.4b. Although different bare bands make some slight changes on the line shape of the curves, the energy features which represent discontinuities in electron self-energy persist and sit at the similar energy positions.

4.5 Temperature Dependence of the Energy Features

The distinct behaviors of the two energy features are further resolved by the temperature-dependent measurements. Shown in Fig. 4.5 is the effective real part of the electron self-energy measured at different temperatures for three typical momentum cuts. It is evident that both the LW and the HI energy features exhibit dramatic superconductivity-induced electron self-energy change upon entering the superconducting state. However, their temperature-dependent behaviors are very different.

First, the coupling strength of the two energy features exhibits strong momentum dependence, as evidenced by the temperature-induced self-energy change [Fig. 4.5g–i]. For the cut 3 near the antinodal region, the superconductivity-induced self-energy change is mainly dominated by the LW energy feature (Fig. 4.5i). When moving to the cut 2, the development of both energy features is clear, but the cou-

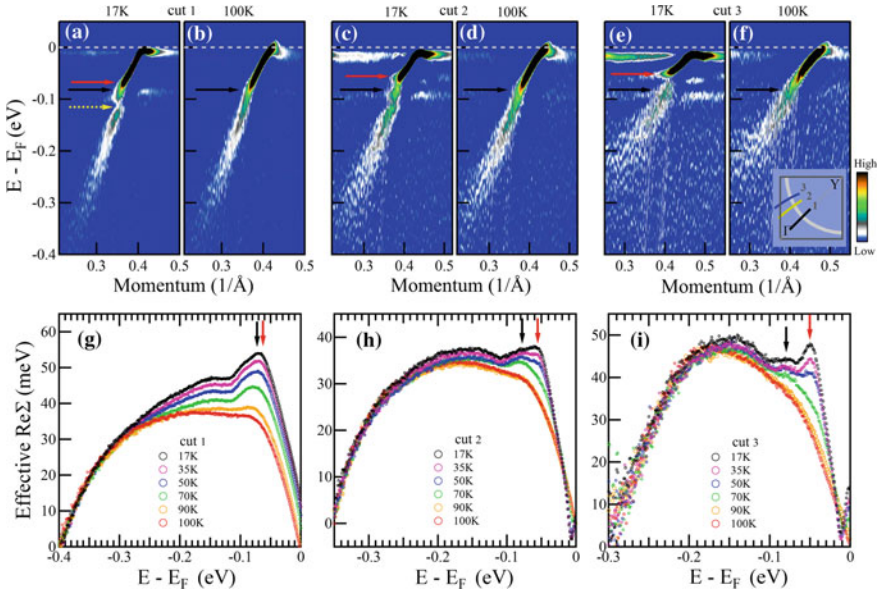


Fig. 4.5 Temperature dependence of the two energy features. EDC second-derivative images of cut 1 measured at 17 K (a) and 100 K (b). c, d and e, f are the same measurements for cut 2 and 3, respectively. g, h and i are the corresponding effective real parts of electron self-energy. Reprinted with the permission from [20]. Copyright 2013 by the American Physical Society

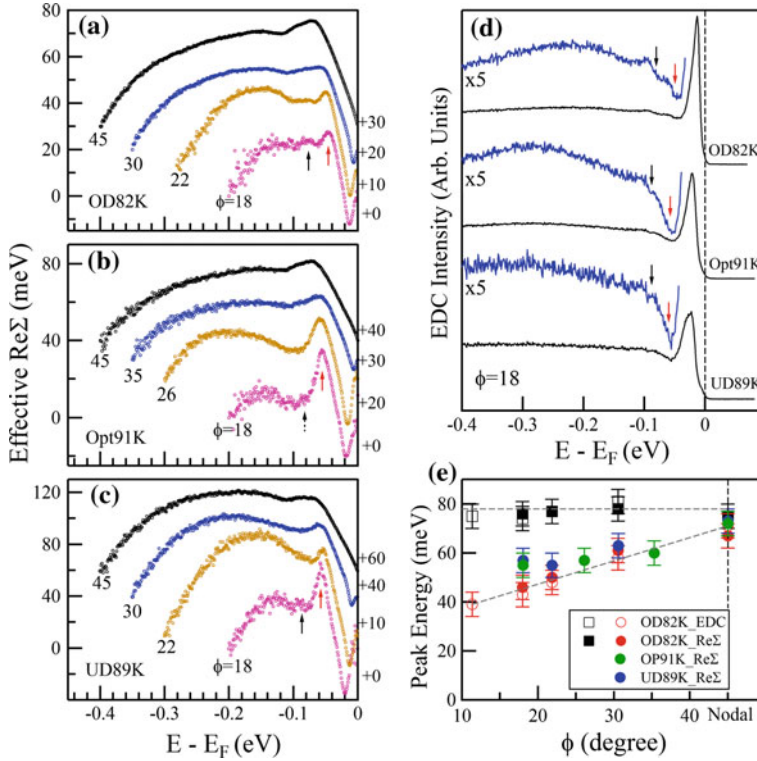


Fig. 4.6 Doping dependence of the two energy features. Effective real part of electron self-energy for OD82K sample (a) Opt91K sample (b) and UD89K sample (c). **d** EDCs at the Fermi momentum k_F along the cut $\Phi = 18^\circ$ for samples with different doping levels. **e** Summary of the momentum dependence of the two energy features. Reprinted with the permission from [20]. Copyright 2013 by the American Physical Society

pling strength of the LW energy feature appears to get weaker when the momentum moves from the antinodal toward the nodal regions. For the cut 1, there is a large superconductivity-induced self-energy change and an apparent existence of the HI energy feature in the normal state. But it is difficult to disentangle whether such a change is caused by HI or LW energy features because they are too close in energy.

Second, these two energy features show different temperature dependence across T_c . It is clear from Fig. 4.5g, h that the HI energy feature can be observed at both below and above T_c . The temperature-induced self-energy change takes off even above T_c , which indicates that the HI energy feature might be caused by a ~ 70 meV phonon. In contrast, the obvious self-energy enhancement of the LW energy feature occurs well into the superconducting state (such as the data at 50 K and below).

4.6 Doping Dependence of the Energy Features

Doping dependence of the two energy features may also provide key information to understand their origin. Shown in Fig. 4.6a–c is the effective real part of electron self-energy along several momentum cuts of Bi2212 OD82, Opt91, and UD89K samples. The EDCs at k_F along a typical momentum cut ($\Phi=18$ degree) of these samples are shown in Fig. 4.6d.

The LW energy feature is clearly observed in the Opt91K (Fig. 4.6b) and UD89K (Fig. 4.6c) samples, and its momentum dependence is also similar to that in the OD82K sample (Fig. 4.6a) which drops in energy when moving from the nodal region to the antinodal region (Fig. 4.6e). On the other hand, the signature of the HI energy feature appears rather weak in the Opt91 and UD89K samples, but hint of its existence is discernable. In particular, double-dip signature in the EDCs of the Opt91 and UD89K samples is observed (Fig. 4.6d) which indicates that HI feature may extend into the underdoped region. We note that the relative intensity of the HI feature is doping dependent which is enhanced in the overdoped region.

4.7 The Possible Origin of the Coexisting Energy Features

Since the two coexisting energy features are clearly resolved for the first time, a natural question to ask is their origin. In particular, how many sharp modes are involved to produce these two features. It has been demonstrated earlier that the electron coupling with one sharp boson mode (with an energy Ω_0) plus a van Hove singularity near the antinodal $(\pi,0)$ region at an energy position of $E(\pi,0)$ can generate two discontinuities in the electron self-energy at $\Omega_0 + E(\pi,0)$ and $\Omega_0 + \Delta_0$ (with Δ_0 being a superconducting gap) [21]. In this scenario, one mode can produce two energy features in the electronic structures which looks superficially similar to the experimental observations. However, the two energy scales from the boson mode plus a van Hove singularity picture are expected to be momentum-independent. Therefore, their energy difference, $E(\pi,0) - \Delta_0$, is expected to be a constant. However, our observations of different momentum dependence of the two energy features are inconsistent with this expectation and thus make this one-mode scenario unlikely.

On the other hand, our results are more consistent with a two-mode picture: The electrons are coupled with two prominent sharp modes. This idea can be illustrated by a simple simulation of the single-particle spectral function for the electron coupling with two sharp Einstein bosons (details of the simulation will be presented below). EDC second-derivative analysis has been performed on the simulated (Fig. 4.2d) and measured (Fig. 4.2c) spectra to enhance the energy features. It is amazing that with such a simple model, the similarity between the simulation and the experiment is very obvious. This similarity in turn demonstrated the solidity to extract energy scales from the peak position of the real part of electron self-energy and dip position in EDCs.

4.8 Simulation of the Electron–Boson Coupling

The electron–boson coupling has been simulated in which two Einstein modes are considered for simplicity. The spectral weight function used here follows the format that described in [22]:

when $|p_0| < \omega$,

$$\frac{1}{\pi} |ImG| = \delta[p_0 - \epsilon_p + (g^2 N/2\omega) \ln|(p_0 + \omega)/(p_0 - \omega)|] \quad (4.1)$$

when $|p_0| > \omega$,

$$\frac{1}{\pi} |ImG| = \frac{g^2 N/2\omega}{[p_0 - \epsilon_p + (g^2 N/2\omega) \ln|(p_0 + \omega)/(p_0 - \omega)|]^2 + |g^2 N\pi/2\omega|^2} \quad (4.2)$$

where p_0 represents the energy of the electron and ω is the energy of the coupling mode. In Ref. [22], only a single Einstein mode was considered. In our case, two modes are included with an energy of 50 and 78 meV, respectively. To best fit the experiment, a constant spectral broadening of 15 meV has been added for the 50 meV mode coupling, whereas a broadening of 20 meV has been added for the 78 meV mode coupling. $g^2 N$, which is a combination of coupling constant and electron density of state, was set to be 0.0008 (eV)^2 for both couplings. The results are shown in Fig. 4.7. The raw spectral intensity, EDC second-derivative image, EDCs, and the effective real part of the electron self-energy are also obtained from the simulation to make a full comparison with the experiment. It is clearly shown that the peak

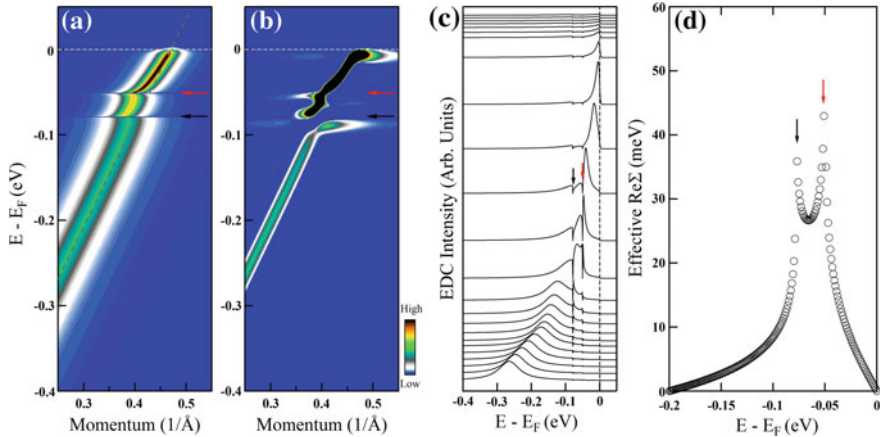


Fig. 4.7 Simulations for electron coupling with two sharp bosonic modes. **a** Simulated spectra. **b** EDC second-derivative image of **a**. **c** EDCs of the simulated spectra. **d** The effective real part of electron self-energy from the simulated spectra

positions in the real part of the electron self-energy, the dip positions in the EDCs, and the break points in the second-derivative images all correspond to the two known bosonic mode energies. This simulation not only provides support for the two-mode scenario, but also illustrates the solidity of the ways we used to deduce the energy features in our experiments.

4.9 Challenge to the Conventional Understanding

The new observations in the current work pose a challenge to our understanding of mode coupling in the superconducting state of cuprate superconductors. In a conventional picture, the electron–boson coupling is nearly momentum-independent. As stated in Ref. [21] that if there is a mode coupling at an energy of Ω in the normal state, its energy is expected to be simply shifted to $\Omega + \Delta_0$ in the superconducting state, where Δ_0 is the largest superconducting gap of this material. This isotropic coupling picture will generate an energy shift Δ_0 over the entire Fermi surface, including the nodal region where the local superconducting gap is zero in a d -wave superconductor such as cuprates [21]. However, this picture is apparently not consistent with our experiments. As shown in Fig. 4.5g–i, the HI energy feature appears above T_c at ~ 78 meV. It does not shift to 103 meV (with an energy gap of $\Delta_0 \sim 25$ meV for the OD82K Bi2212) as expected by the above scenario, but stays nearly at the same energy upon cooling into the superconducting state. While arguments for the solidity of this conventional picture have been raised [23], alternative explanations for this non-energy shift puzzle of the nodal 70 meV kink have involved a strong momentum-dependent coupling in which small q forward scattering was considered as a key player [24]. This scenario has also been applied to explain the ~ 10 meV nodal kink observed recently [2–4] where the energy of the kink was found to be smaller than the largest superconducting gap which directly invalidated the $\Omega + \Delta_0$ conventional picture. In the small q forward-scattering picture, electron scattering only occurs in a small local momentum space such that the shift of the mode energy is determined by the local energy gap $\Delta(\mathbf{k})$ upon entering the superconducting state [25]. While the forward-scattering picture [24, 25] seems to solve the non-shift puzzle of the nodal energy scale across T_c because the local gap near the nodal region is zero, it predicts that the mode energy shift will increase from the nodal to the antinodal regions due to the local gap increase in a d -wave superconductor. Unfortunately, this prediction is not consistent with our current observation that the HI energy scale changes little in energy over a large momentum space.

The LW energy scale is even more anomalous whose energy scale changes from 40 meV near the antinodal region to 70 meV near the nodal region. This is not only different from a momentum-independent mode that is expected from the conventional coupling picture, but is just opposite to what the forward-scattering picture predicted. These observations pose a challenge to the understanding of the electron–mode coupling in the superconducting state of Bi2212 and further theoretical efforts are needed to explain these unusual effects.

4.10 Summary

In summary, we have identified two coexisting sharp mode couplings in the superconducting state of Bi2212 for the first time. These two modes coexist over a large momentum space with distinct momentum dependence: The HI mode keeps its energy near 78 meV over a large momentum space while the LW mode changes its energy from ~ 40 meV near the antinodal region to ~ 70 meV near the nodal region. This momentum dependence cannot be understood by known theories and poses new challenges to the current understanding of electron–boson coupling in the superconducting state of Bi2212. Although our present work does not imply that the two modes are solely responsible for electron pairing in the cuprate superconductors, it solves a long-standing puzzle about the momentum evolution between nodal kink and antinodal kink. Moreover, the strong coupling of these modes in the superconducting state as well as their unusual momentum and temperature dependence has added a significant piece to the current understanding of the many-body effects in cuprates and should be considered in the electron-pairing mechanism.

References

1. Anderson, P.W.: Is there glue in cuprate superconductors? *Science* **316**(5832), 1705–1707 (2007)
2. Dong Wei Lu, X., Wen, J.S., Xu, Z.J., Gu, G.D., Sasagawa, T., Wang, G., Zhu, Y., Zhang, H., Zhou, Y., Wang, X., Zhao, Z., Chen, C., Xu, Z., Zhou, X.J., Zhang, W., Liu, G., Zhao, L., Liu, H., Meng, J.: Identification of a new form of electron coupling in the $\text{Bi}_2\text{Sr}_2\text{CaCu}_2\text{O}_8$ superconductor by laser-based angle-resolved photoemission spectroscopy. *Phys. Rev. Lett.* **100**, 107002 (2008)
3. Vishik, I.M., Lee, W.S., Schmitt, F., Moritz, B., Sasagawa, T., Uchida, S., Fujita, K., Ishida, S., Zhang, C., Devereaux, T.P., Shen, Z.X.: Doping-dependent nodal Fermi velocity of the high-temperature superconductor $\text{Bi}_2\text{Sr}_2\text{CaCu}_2\text{O}_{8+\delta}$ revealed using high-resolution angle-resolved photoemission spectroscopy. *Phys. Rev. Lett.* **104**(20), 207002 (2010)
4. Plumb, N.C., Reber, T.J., Koralek, J.D., Sun, Z., Douglas, J.F., Aiura, Y., Oka, K., Eisaki, H., Dessau, D.S.: Low-energy ($\ll 10$ meV) feature in the nodal electron self-energy and strong temperature dependence of the Fermi velocity in $\text{Bi}_2\text{Sr}_2\text{CaCu}_2\text{O}_{8+\delta}$. *Phys. Rev. Lett.* **105**(4), 046402 (2010)
5. Bogdanov, P.V., Lanzara, A., Kellar, S.A., Zhou, X.J., Lu, E.D., Zheng, W.J., Gu, G., Shimoyama, J.-I., Kishio, K., Ikeda, H., Yoshizaki, R., Hussain, Z., Shen, Z.X.: Evidence for an energy scale for quasiparticle dispersion in $\text{Bi}_2\text{Sr}_2\text{CaCu}_2\text{O}_8$. *Phys. Rev. Lett.* **85**, 2581–2584 (2000)
6. Johnson, P.D., Valla, T., Fedorov, A.V., Yusof, Z., Wells, B.O., Li, Q., Moodenbaugh, A.R., Gu, G.D., Koshizuka, N., Kendziora, C., Jian, S., Hinks, D.G.: Doping and temperature dependence of the mass enhancement observed in the cuprate $\text{Bi}_2\text{Sr}_2\text{CaCu}_2\text{O}_{8+\delta}$. *Phys. Rev. Lett.* **87**, 177007 (2001)
7. Kaminski, A., Randeria, M., Campuzano, J.C., Norman, M.R., Fretwell, H., Mesot, J., Sato, T., Takahashi, T., Kadowaki, K.: Renormalization of spectral line shape and dispersion below T_c in $\text{Bi}_2\text{Sr}_2\text{CaCu}_2\text{O}_{8+\delta}$. *Phys. Rev. Lett.* **86**, 1070–1073 (2001)
8. Lanzara, A., Bogdanov, P.V., Zhou, X.J., Kellar, S.A., Feng, D.L., Lu, E.D., Yoshida, T., Eisaki, H., Fujimori, A., Kishio, K., Shimoyama, J.-I., Noda, T., Uchida, S., Hussain, Z., Shen, Z.-X.:

- Evidence for ubiquitous strong electron-phonon coupling in high-temperature superconductors. *Nature (London)* **412**(6846), 510–514 (2001)
9. Zhou, X.J., Yoshida, T., Lanzara, A., Bogdanov, P.V., Kellar, S.A., Shen, K.M., Yang, W.L., Ronning, F., Sasagawa, T., Kakeshita, T., Noda, T., Eisaki, H., Uchida, S., Lin, C.T., Zhou, F., Xiong, J.W., Ti, W.X., Zhao, Z.X., Fujimori, A., Hussain, Z., Shen, Z.-X.: High-temperature superconductors: universal nodal Fermi velocity. *Nature (London)* **423**(6938), 398 (2003)
 10. Kordyuk, A.A., Borisenko, S.V., Zabolotnyy, V.B., Geck, J., Knupfer, M., Fink, J., Büchner, B., Lin, C.T., Keimer, B., Berger, H., Pan, A.V., Komiya, S., Ando, Y.: Constituents of the quasiparticle spectrum along the nodal direction of high-T_c cuprates. *Phys. Rev. Lett.* **97**, 017002 (2006)
 11. Gromko, A.D., Fedorov, A.V., Chuang, Y.-D., Koralek, J.D., Aiura, Y., Yamaguchi, Y., Oka, K., Ando, Y., Dessau, D.S.: Mass-renormalized electronic excitations at (π , 0) in the superconducting state of Bi₂Sr₂CaCu₂O_{8+ δ} . *Phys. Rev. B* **68**, 174520 (2003)
 12. Kim, T.K., Kordyuk, A.A., Borisenko, S.V., Koitzsch, A., Knupfer, M., Berger, H., Fink, J.: Doping dependence of the mass enhancement in (Pb, Bi)₂Sr₂CaCu₂O₈ at the antinodal point in the superconducting and normal states. *Phys. Rev. Lett.* **91**, 167002 (2003)
 13. Sato, T., Matsui, H., Takahashi, T., Ding, H., Yang, H.B., Wang, S.C., Fujii, T., Watanabe, T., Matsuda, A., Terashima, T., Kadowaki, K.: Observation of band renormalization effects in hole-doped high-T_c superconductors. *Phys. Rev. Lett.* **91**(15), 157003 (2003)
 14. Cuk, T., Baumberger, F., Lu, D.H., Ingle, N., Zhou, X.J., Eisaki, H., Kaneko, N., Hussain, Z., Devereaux, T.P., Nagaosa, N., Shen, Z.-X.: Coupling of the b_{1g} phonon to the antinodal electronic states of Bi₂Sr₂Ca_{0.92}Y_{0.08}Cu₂O_{8+ δ} . *Phys. Rev. Lett.* **93**, 117003 (2004)
 15. Devereaux, T.P., Cuk, T., Shen, Z.-X., Nagaosa, N.: Anisotropic electron-phonon interaction in the cuprates. *Phys. Rev. Lett.* **93**(11), 117004 (2004)
 16. Kamimura, H., Matsuno, S., Suwa, Y., Ushio, H.: Occurrence of d-wave pairing in the phonon-mediated mechanism of high temperature superconductivity in cuprates. *Phys. Rev. Lett.* **77**(4), 723 (1996)
 17. Krahl, H.C., Müller, J.A., Wetterich, C.: Generation of d-wave coupling in the two-dimensional Hubbard model from functional renormalization. *Phys. Rev. B* **79**(9), 094526 (2009)
 18. Choi, H.Y., Varma, C.M., Zhou, X.J.: Superconductivity in the cuprates: deduction of mechanism for d-wave pairing through analysis of ARPES. *Front. Phys.* **6**(4), 440–449 (2011)
 19. Liu, G., Wang, G., Zhu, Y., Zhang, H., Zhang, G., Wang, X., Zhou, Y., Zhang, W., Liu, H., Zhao, L., Meng, J., Dong, X., Chen, C., Xu, Z., Zhou, X.J.: Development of a vacuum ultraviolet laser-based angle-resolved photoemission system with a superhigh energy resolution better than 1 meV. *Rev. Sci. Instrum.* **79**(2), 023105 (2008)
 20. He, J., Zhang, W., Bok, J.M., Mou, D., Zhao, L., Peng, Y., He, S., Liu, G., Dong, X., Zhang, J., Wen, J.S., Xu, Z.J., Gu, G.D., Wang, X., Peng, Q., Wang, Z., Zhang, S., Yang, F., Chen, C., Xu, Z., Choi, H.-Y., Varma, C.M., Zhou, X.J.: Coexistence of two sharp-mode couplings and their unusual momentum dependence in the superconducting state of Bi₂Sr₂CaCu₂O_{8+ δ} revealed by laser-based angle-resolved photoemission. *Phys. Rev. Lett.* **111**(10), 107005 (2013)
 21. Sandvik, A.W., Scalapino, D.J., Bickers, N.E.: Effect of an electron-phonon interaction on the one-electron spectral weight of a d-wave superconductor. *Phys. Rev. B* **69**, 094523 (2004)
 22. Engelsberg, S., Schrieffer, J.R.: Coupled electron-phonon system. *Phys. Rev.* **131**, 993–1008 (1963)
 23. Lee, W.S., Meevasana, W., Johnston, S., Lu, D.H., Vishik, I.M., Moore, R.G., Eisaki, H., Kaneko, N., Devereaux, T.P., Shen, Z.X.: Superconductivity-induced self-energy evolution of the nodal electron of optimally doped Bi₂Sr₂Ca_{0.92}Y_{0.08}Cu₂O_{8+ δ} . *Phys. Rev. B* **77**, 140504(R) (2008)
 24. Kulic, M.L., Dolgov, O.V.: Dominance of the electron-phonon interaction with forward scattering peak in high-T_c superconductors: theoretical explanation of the ARPES kink. *Phys. Rev. B* **71**(9), 092505 (2005)
 25. Johnston, S., Vishik, I.M., Lee, W.S., Schmitt, F., Uchida, S., Fujita, K., Ishida, S., Nagaosa, N., Shen, Z.-X., Devereaux, T.P.: Evidence for the importance of extended Coulomb interactions and forward scattering in cuprate superconductors. *Phys. Rev. Lett.* **108**(16), 166404 (2012)

Chapter 5

Similar Energy Features in $\text{Bi}_2\text{Sr}_2\text{CaCu}_2\text{O}_{8+\delta}$ and Pb

A direct experimental demonstration of the BCS theory in conventional superconductor was realized by the tunneling experiment on Pb in which the phonon spectra were deduced from the fine energy features observed in the electron density of states. This experiment directly illustrated that the electron pairing is mediated by the phonon. However, the success of this experiment was directly related to the improvement of the experimental resolution such that the fine energy features from electron–phonon coupling were finally observed. In high-temperature cuprate superconductors, experimental efforts have also been spent in looking for these energy features. Considering its d wave character, momentum-dependent electron density of states is needed. By using high-resolution laser-based angle-resolved photoemission, we have measured the electron density of states along the underlying Fermi surface of the high-temperature $\text{Bi}_2\text{Sr}_2\text{CaCu}_2\text{O}_{8+\delta}$ superconductor. Fine energy features are observed in the momentum-dependent electron density of states, which are similar to those observed in Pb by tunneling. The first observation of those energy features and the characterization of their momentum dependence by ARPES will prove key information in unraveling the pairing mechanism in the d wave cuprate superconductors.

5.1 Introduction

The BCS theory has achieved great success in explaining the mechanism of conventional superconductors. Its solidity has been tested by many experiments among which is the famous report of tunneling spectra measured on Pb. By subtracting the phonon spectra from the electron density of states, the electron–phonon interaction described in BCS theory was directly demonstrated as the glue for electron pairing. However, this key experiment was actually stimulated by the observation of some fine energy features in the electron density of states which deviated from the standard BCS theory. In the simplified BCS model, the electron density of states as a function of energy in the superconducting phase, $N_T(\omega)$, is always larger than that

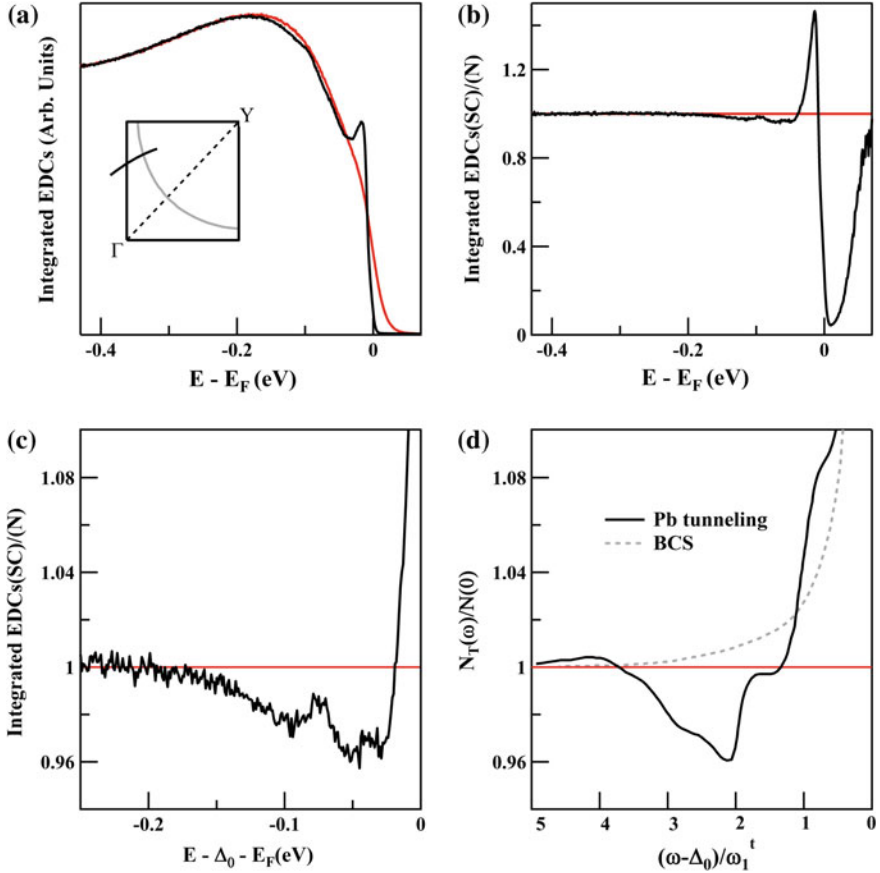


Fig. 5.1 Fine structures in the ARPES spectra on Bi2212. **a** Integrated spectra for an overdoped 82 K sample at 17 K (black curve) and 100 K (red curve) along the momentum cut shown in the inset. **b** Integrated spectra normalized by the 100 K data. **c** The fine structures shown in an expanded scale. **d** Tunneling measurements on Pb [3]

in its normal state, except for the gapped region where no electronic state exists in the superconducting state. As shown in Fig. 5.1d, the ratio between $N_T(\omega)$ and $N(0)$ (normal phase electron density of states at the Fermi energy) is always larger than 1 although it decreases with higher binding energy. This prediction is generally consistent with the experimental results. However, when the tunneling experiment with improved energy resolution was first carried out by Giaever et al. some fine energy features were observed in the superconducting electron density of states which produce an energy region where $N_T(\omega)/N(0)$ has a value smaller than 1 [1]. Stimulated by this observation, careful measurements with even higher resolution were carried out by Rowell et al. and those fine structures were quantitatively resolved [2]. Theoretical simulation [3] and McMillan–Rowell inversion [4] have finally addressed the

origin since the boson spectra deduced from those fine structures are identical to the phonon spectra observed in the same material.

The tunneling experiment, which pinned down the pairing mechanism of conventional superconductors, has also been proposed and tested in high-temperature cuprate superconductors [5]. However, the d wave character makes cuprate more complicated than the s wave superconductors. While momentum dependence is the key information needed for unraveling the mechanism of d wave superconductors, momentum resolution is not achievable by the traditional tunneling measurements. ARPES, known as a powerful tool to resolve the momentum-dependent electronic structures, has been considered as a candidate for this purpose. However, the energy resolution of ARPES is not as good as that of tunneling which makes the observation of fine energy features difficult. The application of vacuum ultraviolet laser in our ARPES system has greatly improved the energy resolution of the system which makes the above measurements possible.

5.2 Observation of the Fine Structures

The total electron density of states along a momentum line in the Brillouin zone can be obtained by integrating the photoemission intensity over the angles. As shown in Fig. 5.1a, the black and red curves represent the angle-integrated electron density of states for an off-nodal cut of the overdoped $\text{Bi}_2\text{Sr}_2\text{CaCu}_2\text{O}_{8+\delta}$ ($T_c = 82\text{K}$) sample at 17 and 100 K, respectively. The momentum location of the cut is shown in the inset. We notice that the high energy region of the two curves overlaps perfectly with each other. The ratio between the variation and background is smaller than 0.5 % which was not achievable in earlier ARPES experiments. This was not only from the much improved energy resolution and statistics by using laser ARPES, but also from the stability of the system which did not induce any systematic error with the temperature change. This super-high experimental accuracy is also the basis to observe the fine energy features to be elaborated below, since they are in the order of 2 ~ 5 % comparing to the intensity of the background.

As shown in Fig. 5.1a, the major difference between the low-temperature (17 K) and high-temperature (100 K) data is the coherent peak which presents in the superconducting state and disappears in the normal state. The spectral weight distribution change due to the temperature broadening of Fermi distribution function can also be clearly seen in the plot. These differences are consistent with the theoretical expectation and earlier ARPES observations. More interesting findings come out with a careful examination of the spectra at the low binding energy region ($<0.2\text{ eV}$). While the 100 K data show a smooth evolution as a function of energy, some fine features can be recognized in the spectra at 17 K. In order to enhance the differences, the data analysis similar to that of the tunneling experiment has been performed. As plotted in Fig. 5.1b, the low-temperature (superconducting state) curve is divided by the high-temperature (normal state) one. A special energy region is clearly observed in which the ratio between low- and high-temperature curves is smaller than 1. Moreover,

fine energy features show up in this energy region. This is different from the smooth curve predicted by the simplified BCS theory (the dashed line in Fig. 5.1d). On the other hand, the current observations are very similar to the tunneling results on Pb where the fine features in the special energy region reflect the relative strong electron correlation which causes the deviation from standard BCS simulation. As elaborated earlier that these fine features (solid line in Fig. 5.1d) were proven as the fingerprint of the electron–phonon coupling which mediates the electron pairing in the system. The special energy region in Fig. 5.1b is plotted in an expanded scale in Fig. 5.1c to show the fine features. Two small peaks are clearly resolved with an energy of 50 and 100 meV, respectively. We note that these fine features might be related to the coexisted coupling modes reported in the last chapter since they are similar in energy. If that is the case, it will be much more complicated than the electron–phonon coupling observed in Pb. While more theoretical efforts are needed to pin down the origin of the fine structures, the amazing similarities between the current observations on Bi2212 (Fig. 5.1c) and the earlier results on Pb (Fig. 5.1d) have shed new light on the pairing mechanism of the cuprates.

5.3 Temperature Dependence of the Fine Structures

Detailed temperature dependence of the fine structures is shown in Fig. 5.2. The solidity of the results can be recognized by the following facts: First, the high energy region (>0.25 eV) of the angle-integrated spectra obtained at various temperatures (17, 35, 50, 70, 90, and 100 K) is perfectly overlapped (Fig. 5.2a). Second, although the fine structures are very small, their evolution as a function of temperature shows clear self-consistency. To perform a systematic temperature-dependent analysis, the angle-integrated spectra at various temperatures have been divided by the 100 K data (Fig. 5.2b). Two coherent peaks have been clearly observed below and above Fermi level symmetrically at a temperature of 50 K which is well below the superconducting transition temperature but high enough to include sufficient spectral weight above the Fermi level. These superconducting coherent peaks disappear above T_c (e.g., when the 90 K data is divided by the 100 K one). The above results have not only demonstrated the particle–hole symmetry expected in the superconducting state of the material but also proven the high quality of our experimental data.

Now, we will turn to the key point of our current finding: the temperature dependence of the fine energy features. As shown in Fig. 5.2b, the fine features are very obvious below 50 K (e.g., the black curve for 17 K, pink curve for 35 K, and blue curve for 50 K). However, the intensities of the structures start to decrease dramatically when the temperature is approaching T_c (e.g., green curve for 70 K) and disappear above T_c (e.g., orange curve for 90 K). We note that the energy structures which are induced or enhanced by superconductivity should be enhanced when they are divided by the 100 K data. On the other hand, the possible features which are insensitive to superconductivity and persist above 100 K might be suppressed in our analysis. Therefore, the disappearance of fine features in the 90 K data does not

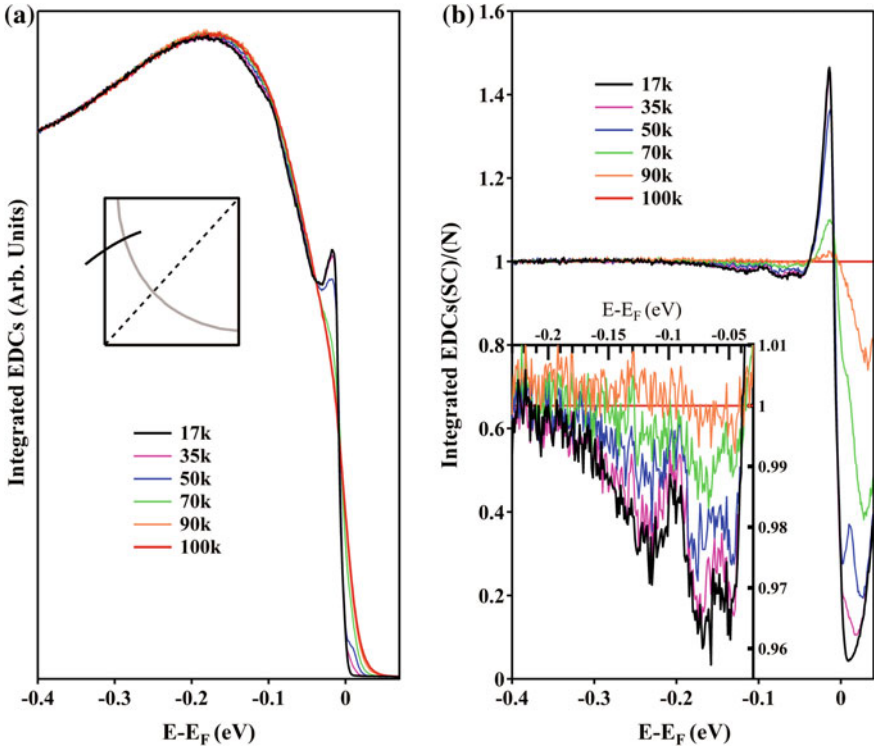


Fig. 5.2 Temperature dependence of the fine structures. **a** Temperature dependence of the integrated spectra. **b** Integrated spectra normalized by the 100 K data at various temperatures

provide sufficient evidence to conclude that the onset temperature of these features is at T_c . However, the enhancement from superconductivity is very obvious.

Regardless of the accurate onset temperature for the fine features, their existence in a special energy region of the angle-integrated electron density of states is clearly established by our experiments. Their consistent evolution with temperature has confirmed the solidity of the observation.

5.4 Momentum Dependence of the Fine Structures

A special advantage of ARPES measurements is the momentum resolution. As is known to all that cuprates are d wave high-temperature superconductors. Both the superconducting energy gap and electron self-energy of cuprates show obvious momentum dependence. Therefore, if the fine energy features we observed are related to the pairing glue in cuprate superconductors, similar to those observed in Pb by

tunneling, then the momentum dependence of these fine features is very critical to understanding the pairing mechanism.

The photoemission intensity images along several momentum cuts are shown in Fig. 5.3a–e, and their corresponding angle-integrated spectra at 17 and 100 K are normalized by the 100 K data and plotted in Fig. 5.3f–j. The momentum locations of the cuts are indicated in the inset of Fig. 5.3f. First, a special energy region has been clearly revealed over a large momentum space. In this energy region, the superconducting electron density of states becomes lower than that of the normal state due to electron correlation. Second, the energy onset of this energy region shows momentum dependence which changes its binding energy from 0.3 eV near the nodal region to ~ 0.1 eV near the antinodal region. This change is more obvious when we plot the special energy region of the spectra in an expanded scale in Fig. 5.4. Third, the fine features also widely exist in the large momentum region we covered (Fig. 5.4).

Key information for the d wave superconducting pairing mechanism should be contained in the above observations, provided that the special energy region and fine features are the fingerprint of the pairing glue similar to the case of Pb. In particular, the change of the special energy region with momentum indicates that the energy cutoff for the electrons involved in the pairing process is momentum dependent. Moreover, we notice that a similar momentum dependence is observed for the bottom of the conduction band. Therefore, it is reasonable to conclude that a large portion

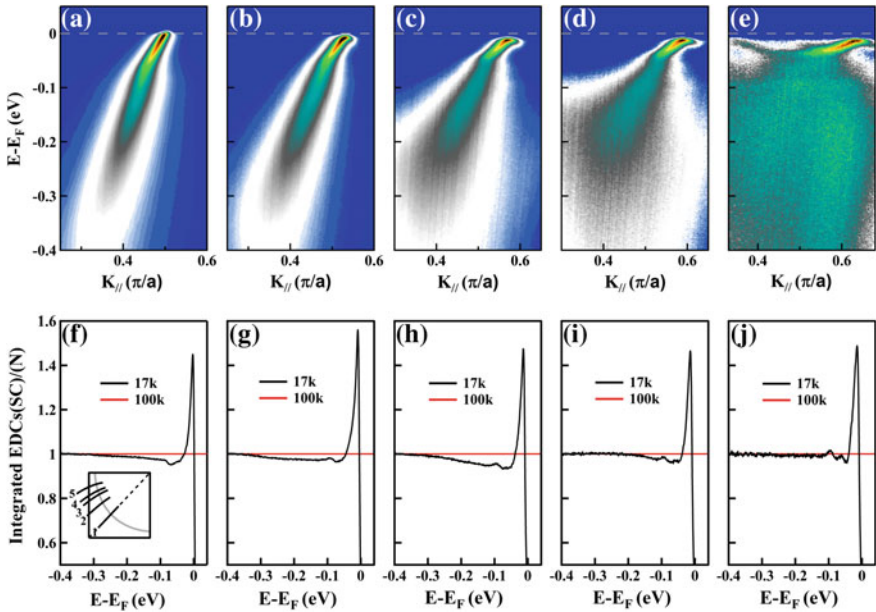


Fig. 5.3 Momentum dependence of the fine structures. **a–e** Raw photoemission intensity plots along different momentum cuts. **f–j** The corresponding normalized integrated spectra. The momentum locations of the cuts are shown in the inset of **f**

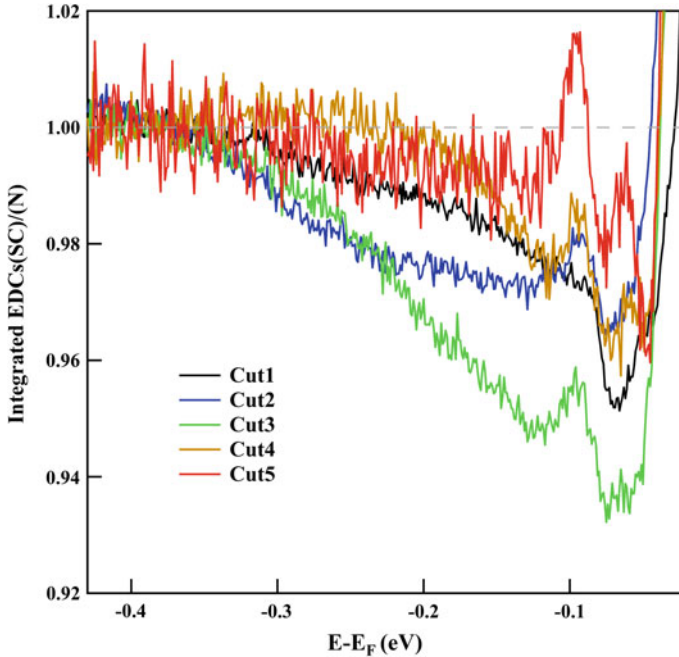


Fig. 5.4 Momentum dependence of the fine structures shown in an expanded scale

of the electrons in the conduction band are involved in the superconducting pairing process. This is different from the isotropic BCS picture that only the electrons in a small energy window near Fermi surface contribute to the superconductivity, and the electrons with higher binding energies stay unaffected. Even in Pb where the correlation effect was considered, the highest energy cutoff is not higher than that of the Debye temperature [1]. The fact that high-energy electrons are involved in the electron pairing in Bi2212 has in turn demonstrated the strong correlation in this system, and the special momentum dependence of the energy cutoff has shed new light on the understanding of the superconducting mechanism.

Figure 5.5 shows the momentum dependence of the fine structures measured at various temperatures. First, although the onset energy of the special region shows momentum dependence, it does not change with temperature. This can be clearly seen in the inset of Fig. 5.5a–e, in which expanded energy scales are used. Second, the fine features along different momentum cuts are all clearly observed in the superconducting state. Third, a “peak–dip–shoulder” feature is observed near the nodal region with the peak locating at $\sim 100\text{meV}$ and the dip at $\sim 70\text{meV}$. The shoulder locates at a smaller binding energy and gets enhanced when the momentum cut moves toward antinodal region. It becomes a well-defined peak in the measurement along cut 5 (Fig. 5.5e), and the “peak–dip–shoulder” feature changes into double “peak–dip” structures. Although further analysis is needed, the momentum and temperature

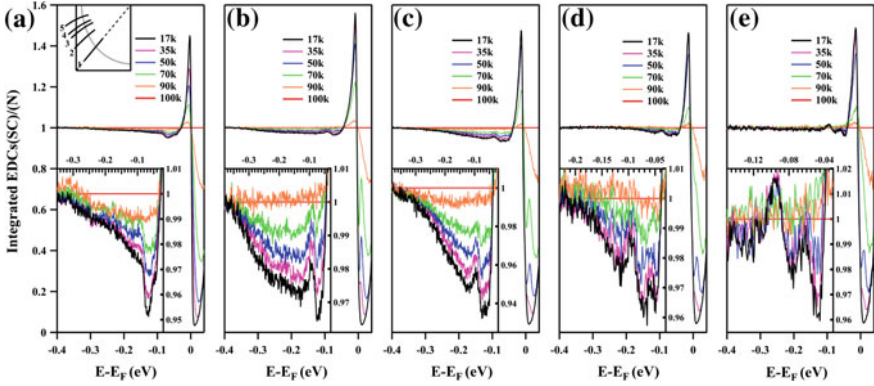


Fig. 5.5 Momentum and temperature dependence of the fine structures. **a–e** Temperature dependence of the normalized angle-integrated spectra along five different momentum cuts

dependence of these fine features are consistent with that of the sharp mode couplings reported in the last chapter.

5.5 Summary

Super-high-resolution angle-resolved photoemission spectroscopy measurements have been carried out on an overdoped Bi2212 sample with a transition temperature of $T_c = 82$ K. Momentum-dependent electron density of states are obtained by the angle-integrated photoemission intensity along different momentum cuts from nodal to near antinodal region. The ratio between the electron density of states in superconducting state and normal state is calculated from the temperature-dependent measurements performed both above and below T_c . A special energy region is observed in which the ratio is smaller than 1, and fine energy features are revealed in this energy region at various momentum locations. This is very similar to the case of the tunneling measurements on Pb and we note that those fine features in Pb were proven to be the fingerprints of the pairing glue.

Detailed momentum-dependent measurements have also been carried out. We note that the special energy region extends over a large momentum area, although its energy onset changes from 0.3 eV near the nodal region to ~ 0.1 eV near the antinodal region. This indicates that a large portion of the electrons in the conduction band are affected by the occurrence of superconductivity. Moreover, the fine features also exhibit momentum dependence which changes from the “peak–dip–shoulder” near the nodal region to double “peak–dip” structures near the antinodal region. These observations might be closely related to the pairing glue and thus will shed new light on the mechanism of the d wave superconductors.

References

1. Giaever, I., Hart, H.R., Megerle, K.: Tunneling into superconductors at temperatures below 1° K. *Phys. Rev.* **126**, 941–948 (1962)
2. Rowell, J.M., Anderson, P.W., Thomas, D.E.: Image of the phonon spectrum in the tunneling characteristic between superconductors. *Phys. Rev. Lett.* **10**, 334–336 (1963)
3. Schrieffer, J.R., Scalapino, D.J., Wilkins, J.W.: Effective tunneling density of states in superconductors. *Phys. Rev. Lett.* **10**, 336–339 (1963)
4. McMillan, W.L., Rowell, J.M.: Lead phonon spectrum calculated from superconducting density of states. *Phys. Rev. Lett.* **14**, 108–112 (1965)
5. Fischer, Φ ., Kugler, M., Maggio-Aprile, I., Berthod, C., Renner, C.: Scanning tunneling spectroscopy of high-temperature superconductors. *Rev. Mod. Phys.* **79**(1), 353 (2007)
6. unjić.: Excitation energy dependence of core-level X-ray-photoemissionspectra line shapes in metals. *Phys. Rev. B* **12**, 524–530 (1975)

Chapter 6

Electronic Structures of the Superconducting Single-Layer FeSe/SrTiO₃ Films

Much attention has been attracted by the recent discovery of iron-based high-temperature superconductors. Nevertheless, two prominent issues are yet to be addressed. The first one is to find out a way to further increase the superconducting transition temperature (T_c) in iron-based superconductors, and the second one is to understand the superconductivity mechanism. Recently, possible high T_c superconductivity has been reported in a single-layer FeSe/SrTiO₃ film. The observation of a high transition temperature in a material with the simplest crystal structure provides an ideal platform to study the above important issues. We have performed investigations of the electronic structure and superconducting gap of the single-layer FeSe superconductor. Its Fermi surface is distinct from other iron-based superconductors, consisting only of electron-like pockets near the zone corner without indication of any Fermi surface around the zone center. The superconducting gap is nearly isotropic, and the temperature dependence of the superconducting gap gives a transition temperature $T_c \sim 55$ K for this superconducting film. Our results have established a clear case that high T_c superconductivity in iron-based superconductors can be realized with such a simple electronic structure.

6.1 Introduction

Signature of high-temperature superconductivity has been reported in single-layer FeSe films grown on SrTiO₃ substrate recently [1]. The significance of this observation lies in the high superconducting transition temperature of the films which might break the record of the existing iron-based superconductors [2–6]. Shown in Fig. 6.1 is the STM topography image and the tunneling spectrum of the single-layer film [1]. In fact, a high T_c is unexpected in the FeSe system because the bulk FeSe exhibits a T_c of only 8 K at ambient pressure [5] although it can be enhanced to 36.7 K under high pressure [7]. Another related material is the intercalated FeSe system $A_x\text{Fe}_{2-y}\text{Se}_2$ ($A = \text{K, Cs, Rb and Tl}$), which shows a T_c of 32 K at ambient pressure [8, 9] and possible T_c near 48 K under high pressure [10]. The superconducting single-layer FeSe film

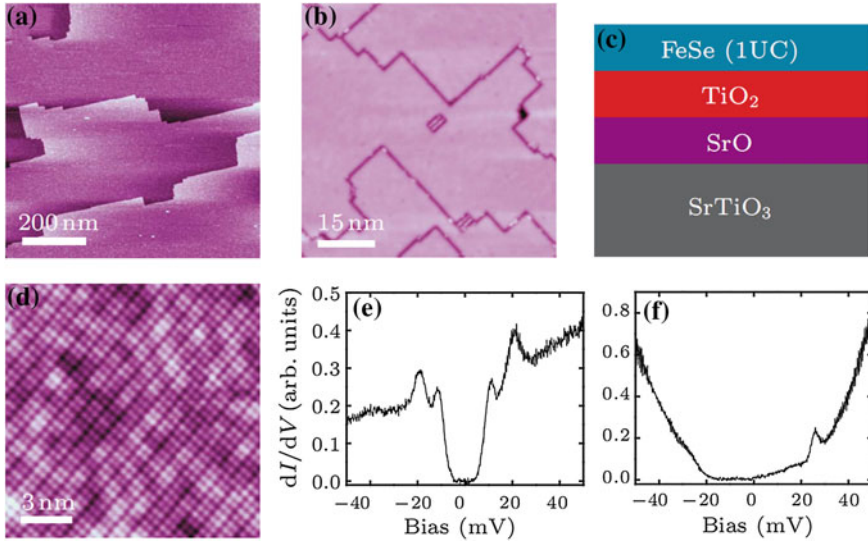


Fig. 6.1 STM topography. **a** STM topography of STO(001). **b** STM topography of the FeSe film on STO substrate. **c** Schematic of the FeSe film on STO substrate. **d** Atomically resolved STM topography. **e** Tunneling spectrum on single-layer film. **f** Tunneling spectrum on double-layer film. Reprinted with the permission from [1]

presents a T_c higher than all the other FeSe-related systems. Unraveling the origin of high-temperature superconductivity in such a simple system [1] is crucial to understanding the superconductivity mechanism in the Fe-based superconductors. It can also provide key insights on designing new superconductors with higher transition temperatures.

Specifically, single-layer FeSe superconductor shows advantages in a number of aspects. First, it has the simplest crystal structure among all the Fe-based superconductors [2–6]. Only one FeSe layer is contained, which represents the essential building block for superconductivity in the Fe-based compounds. Second, single-layer FeSe, composed of a Se–Fe–Se stack along the c -axis with a thickness of 5.5 Å, is a strictly two-dimensional (2D) system which provides a clear case to study the electronic structure of the material without complications of k_z . This is much simpler than the earlier case with bulk compounds: The k_z dependence of the band dispersion makes it hard to pin down or rule out an electronic property of the material (e.g., the existence of a gap node in the superconducting state) before the complete electronic structure covering all the three-dimensional (3D) momentum space is obtained, which is not only time-consuming but also difficult [11]. Third, the superconducting phase in the FeSe film is pure compared to the $A_x\text{Fe}_{2-y}\text{Se}_2$ ($A = \text{K}, \text{Cs}, \text{Rb}, \text{Tl}, \text{etc.}$) superconducting system [8, 9, 12] where the real superconducting phase is yet to be identified due to phase inhomogeneity.

Therefore, the discovery of high T_c superconductivity in the single-layer FeSe [1] provides a unique platform to sort out the key components in achieving high-temperature superconductivity in the Fe-based compounds, and the measured electronic structure to be presented in this chapter is the most direct evidence toward understanding its superconducting origin.

6.2 Method

6.2.1 *Preparation and Post-Annealing of the Single-Layer FeSe Films*

The single-layer FeSe thin films were grown on SrTiO₃(001) substrate by the molecular beam epitaxy (MBE) method and were characterized by scanning tunneling microscope and transport measurements. The details of the sample growth can be found in [1]. An amorphous Se capping layer was used to cover the prepared superconducting thin film in order to transfer the sample from the MBE preparation chamber to a different ARPES measurement chamber. The sample was then heated up to 400°C for 2 h in the ARPES chamber such that the Se layer was desorbed from the sample surface and intrinsic electronic structure of the single-layer FeSe film can be probed.

6.2.2 *Calibration of the Sample Temperature*

The FeSe thin film was grown on SrTiO₃ substrate and mounted on the cold finger of the cryostat in a way different from that of the usual cleaved single-crystal samples. At the same temperature of the cold finger, the existence of substrate and poorer thermal contact make the temperature on the FeSe thin film higher than that of the usual cleaved sample. Therefore, the usual sample temperature sets a lower limit to the temperature of the FeSe thin film. In order to accurately monitor the temperature of the FeSe thin film, we measure the Fermi level of a piece of polycrystalline gold foil glued on a similar SrTiO₃ substrate using our high-resolution laser photoemission. By fitting the gold Fermi-level width with the Fermi distribution function, we can estimate the temperature of gold on SrTiO₃. We note that the Fermi-level width contains a couple of contributions including the temperature broadening, instrumental resolution, and cleanliness of gold. Therefore, the estimated temperature sets an upper limit to the gold temperature which is close to the temperature of FeSe thin film on SrTiO₃. We found the temperature measured from this gold reference is higher than the nominal usual sample temperature by ~ 10 K. Therefore, the real temperature of the FeSe thin film lies in between the lower and upper temperature limits, with an error bar of ± 5 K.

6.2.3 High-Resolution ARPES Measurements

High-resolution angle-resolved photoemission measurements were taken on our laboratory system [13]. Helium discharge lamp, with a photon energy of $h\nu = 21.218$ eV, was used as the light source. The energy resolution was set at 10 meV for the Fermi surface mapping and band structure measurements and at 4 meV for the superconducting gap measurements. The angular resolution was $\sim 0.3^\circ$. The Fermi level was obtained by measuring a polycrystalline gold piece electrically connected to the sample. The base pressure for the measurements was better than 5×10^{-11} Torr.

6.3 Fermi Surface and Band Structure

Figure 6.2a shows the Fermi surface of the single-layer FeSe thin film covering multiple Brillouin zones. Fermi surface of $(\text{Tl, Rb})_x\text{Fe}_{2-y}\text{Se}_2$ superconductor ($T_c = 32$ K) (Fig. 6.2b) [15–18] and $(\text{Ba}_{1.6}\text{K}_{0.4})\text{Fe}_2\text{As}_2$ ($T_c = 35$ K) (Fig. 6.2c) [19–22], and the calculated Fermi surface of FeSe (Fig. 6.2d) [23] are presented for comparison. For the single-layer FeSe superconductor, only an electron-like Fermi surface around M (π, π) (denoted as γ hereafter) was observed (Fig. 6.2a), and no indication of Fermi surface was found near the Γ (0,0) point. The γ Fermi surface is nearly circular with a Fermi momentum (k_F) of 0.25 in a unit of π/a (lattice constant $a = 3.90$ Å), which is significantly smaller than $0.35 \pi/a$ found in $(\text{Tl,Rb})_x\text{Fe}_{2-y}\text{Se}_2$ superconductor [16]. By assuming that the Fermi surface around M consists of two degenerate Fermi surface sheets (Fig. 6.2d), an electron counting of 0.10 electrons/Fe can be obtained from the Fermi surface area. This is considerably smaller than that in $(\text{Tl,Rb})_x\text{Fe}_{2-y}\text{Se}_2$ superconductor (0.18 electrons/Fe). On the other hand, it is closer to the optimal doping level in electron-doped Ba $(\text{Fe}_{1-x}\text{Co}_x)\text{As}_2$ ($x \sim 0.07$) [24].

The band structure of the single-layer FeSe thin film along different cuts is shown in Fig. 6.3a and c with the corresponding momentum location of the cuts in Fig. 6.3d. The energy distribution curves (EDCs) of Fig. 6.3a are shown in Fig. 6.3b. It is clear that the γ band bottom lies at 60 meV below the Fermi level which is slightly deeper than the 50 meV in $(\text{Tl,Rb})_x\text{Fe}_{2-y}\text{Se}_2$ superconductor [16]. By considering the Fermi surface size and the bandwidth, an effective electron mass of $2.7 m_e$ (m_e is the free electron mass) can be obtained in the single-layer FeSe and $6.1 m_e$ in $(\text{Tl, Rb})_x\text{Fe}_{2-y}\text{Se}_2$ superconductor. This might indicate that the electrons in single-layer FeSe are lighter than those in $(\text{Tl, Rb})_x\text{Fe}_{2-y}\text{Se}_2$ superconductor.

The observed Fermi surface of the single-layer FeSe superconductor only consists of electron-like Fermi surface sheets around M, which is distinct from all the other Fe-based superconductors. Majority of the Fe-based superconductors (e.g., $(\text{Ba, K})\text{Fe}_2\text{As}_2$) show a holelike Fermi surface sheets around the Γ point according to theoretical calculations [25, 26] and ARPES measurements (Fig. 6.2c) [19–22]. While the holelike Fermi surface sheet is absent in the $\text{A}_x\text{Fe}_{1-y}\text{Se}_2$ superconduc-

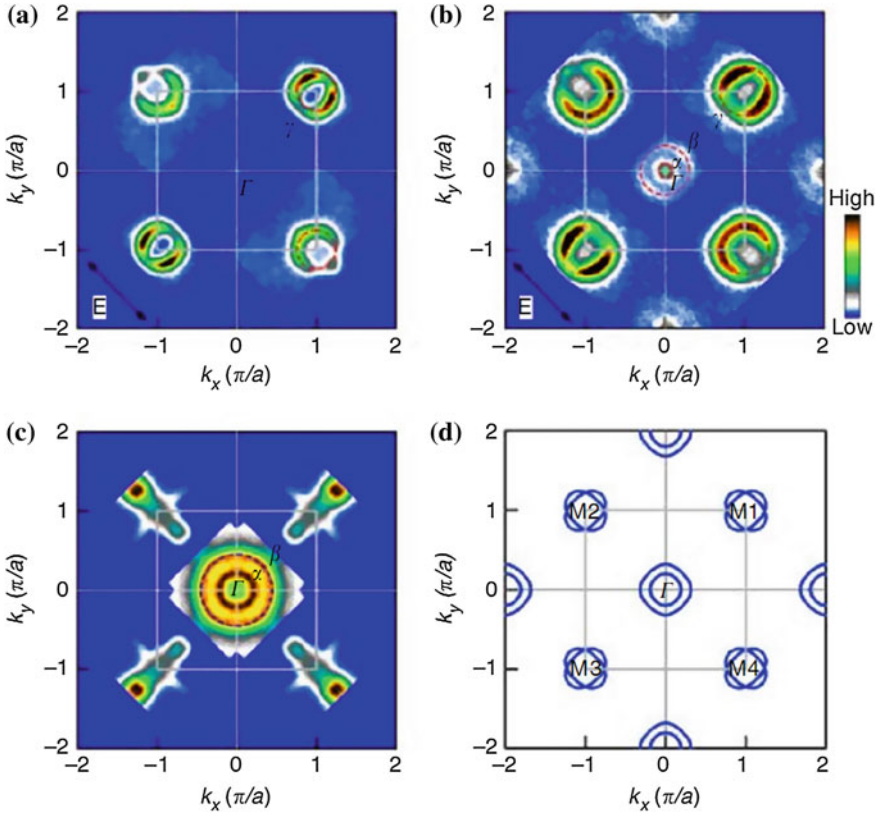


Fig. 6.2 Distinct Fermi surface of the single-layer FeSe superconductor. **a** Fermi surface mapping of the FeSe film on STO substrate. **b** Fermi surface mapping of $(\text{Tl, Rb})_x\text{Fe}_{2-y}\text{Se}_2$ superconductor. **c** Fermi surface mapping of $(\text{Ba}_{1.6}\text{K}_{0.4})\text{Fe}_2\text{As}_2$ superconductor. **d** Fermi surface of β -FeSe by band structure calculations for $k_z = 0$ [14]

tors [15–18], electron-like Fermi surface sheets remain present around the Γ point (Fig. 6.2b).

The band structure of single-layer FeSe is also different from that of the other compounds which cannot be explained by a simple rigid shift from the bands of $(\text{Tl, Rb})_x\text{Fe}_{2-y}\text{Se}_2$ superconductors. First, as mentioned above, the γ band shape near M is significantly different leading to a lighter effective mass. Second, if it is a rigid band shift, the lower electron doping in FeSe superconductor should shift the bands toward the Fermi level when compared with the bands in $(\text{Tl, Rb})_x\text{Fe}_{2-y}\text{Se}_2$ superconductors. However, we notice that the top of the holelike α band near Γ point in FeSe superconductor (Fig. 6.3a, left panel) locates at 80 meV below the Fermi level which is similar to that in $(\text{Tl, Rb})_x\text{Fe}_{2-y}\text{Se}_2$ superconductor [16]. Moreover, the bottom of the electron-like γ band near M in FeSe (Fig. 6.3a, right panel) locates

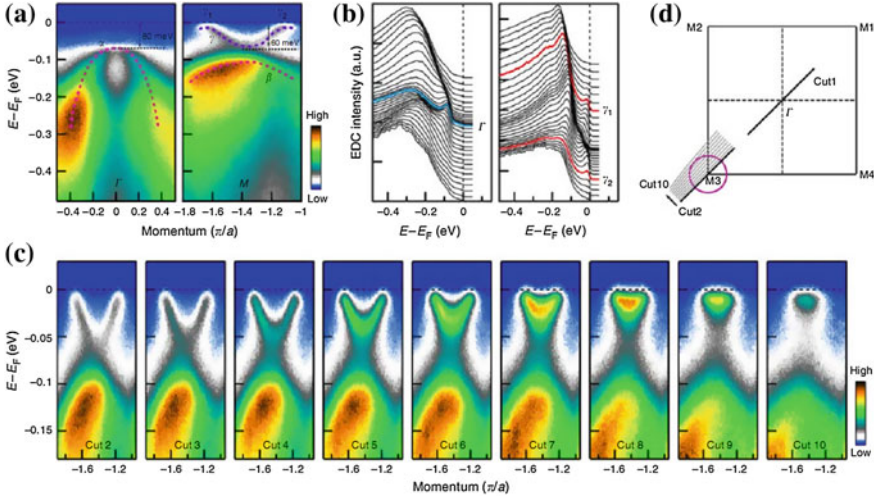


Fig. 6.3 Band structure of the single-layer FeSe superconductor. **a** Band structure along high-symmetry directions crossing the Γ point and the M3 point. **b** The corresponding EDCs. **c** Detailed band structure evolution near the M3. **d** The locations of the momentum cuts [14]

at 60 meV below the Fermi level which is even deeper than that in $(\text{Tl, Rb})_x\text{Fe}_{2-y}\text{Se}_2$ superconductor (~ 50 meV below the Fermi level) [16].

6.4 Temperature Dependence of the Superconducting Gap

The accurate determination of the superconducting gap requires a clear observation of the quasi-particle peak along the underlying Fermi surface of the material. This criterion has been satisfied by the current measurement as evidenced by the coherent superconducting peak (Fig. 6.4b) and a clear underlying γ Fermi surface sheet near M point (Fig. 6.2a). In order to establish the superconducting transition temperature, we first examine the temperature dependence of the superconducting gap. Figure 6.4a shows the photoemission intensity plots of the momentum cut near M3 (momentum location of the cut is shown in Fig. 6.4e) at various temperatures. The Fermi distribution function has been divided such that the opening of a superconducting gap at low temperature can be visually inspected. The corresponding energy distribution curves (EDCs) at the Fermi momentum are shown in Fig. 6.2b. The sharp coherent peak is obvious at low temperature (e.g., 20 K). A commonly used symmetrization procedure was carried out on the original EDCs to remove the effect of Fermi distribution function near the Fermi level [27] such that a gap opening can be visually inspected as a dip in the Fermi energy in the symmetrized EDCs (e.g., 20 K in Fig. 6.2c). This spectral dip in Fermi energy is gradually filled up with increasing temperature and disappears near 50 ~ 55 K. In Fe-based superconductors, the typical

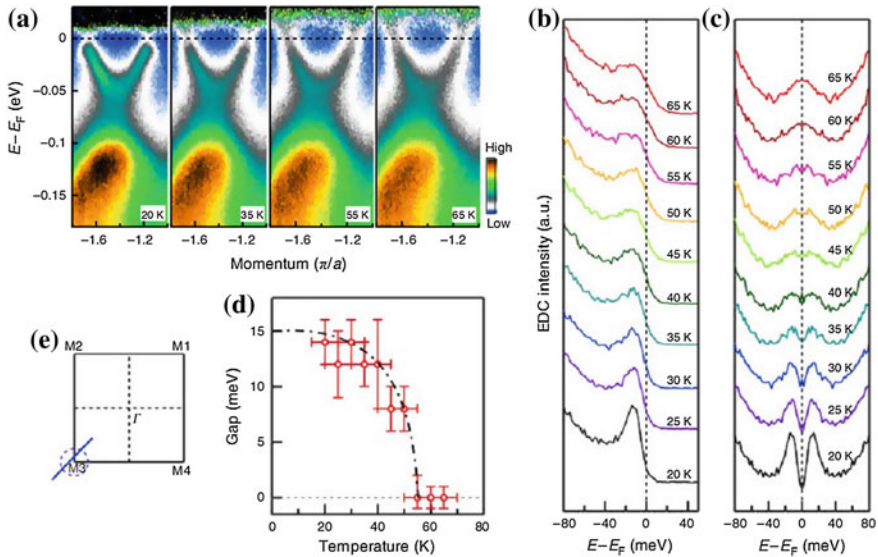


Fig. 6.4 The temperature dependence of the superconducting gap in single-layer FeSe films. **a** Photoemission images along the momentum cut near the M3 point measured at different temperatures. **b** Raw EDCs (**b**) and symmetrized EDCs (**c**) at the Fermi momenta measured at different temperatures. **d** Temperature dependence of the superconducting gap. **e** Location of the momentum cut [14]

ARPES measurements have shown that the energy gap closes at the superconducting transition temperature [16, 19]. Therefore, the temperature-dependent measurement in Fig. 6.4 indicates that this single-layer FeSe sample has a T_c around $(55 \pm 5 \text{ K})$. This gap-closing temperature value is reproducible with an independent measurement on another sample prepared with similar growth and annealing conditions. It is interesting to note that the temperature dependence of the superconducting gap size (Fig. 6.4d) follows the BCS form with the largest gap size of $\sim 15 \text{ meV}$ at the lowest temperature we measured (20 K). In the $(\text{Ti, Rb})_x\text{Fe}_{2-y}\text{Se}_2$ superconductor ($T_c = 32 \text{ K}$), high-resolution ARPES measurements have revealed a gap size of $\sim 9.7 \text{ meV}$ [12]. If we assume the same ratio between the superconducting gap size and T_c , the $\sim 15\text{-meV}$ gap in the current superconducting FeSe sample would give a T_c of $\sim 50 \text{ K}$ which is similar to the value obtained from the temperature-dependent measurement (Fig. 6.4d).

6.5 Momentum Dependence of the Superconducting Gap

Besides the superconducting transition temperature, another key parameter to be obtained from experiments is the symmetry of the superconducting gap. Momentum-dependent measurement by ARPES could provide the direct information for the

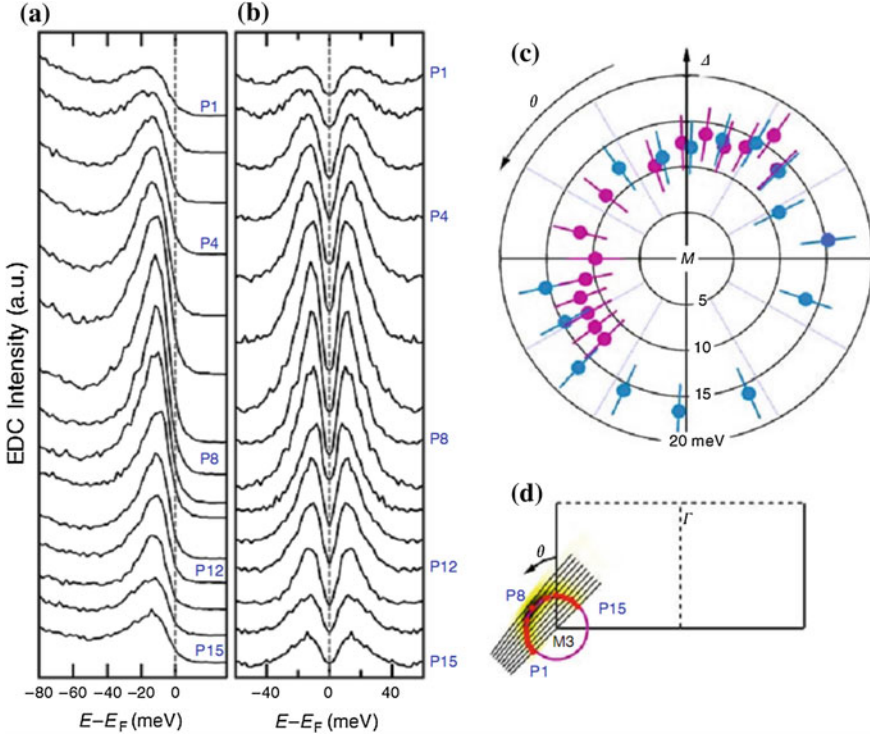


Fig. 6.5 Momentum dependence of superconducting gap. EDCs along the Fermi surface (a) and their corresponding symmetrized EDCs (b) measured at 20 K. c Momentum dependence of the superconducting gap. d The locations of the momentum cuts [14]

superconducting gap function. High-resolution Fermi surface mapping (energy resolution of 4 meV) has been performed around the γ pocket at M (Fig. 6.5d). Figure 6.5a shows EDCs along the underlying γ Fermi surface measured in the superconducting state ($T = 20$ K). The corresponding symmetrized EDCs are shown in Fig. 6.5b. Two independent measurements have been taken on two samples prepared with similar growth and annealing conditions. The extracted superconducting gap for both samples is nearly isotropic, and no indication of zero gap is observed around the γ Fermi surface. The single-layer FeSe films are strictly two-dimensional in nature. Therefore, complications from 3D Fermi surface associated with bulk materials have been avoided in our case. These results have unambiguously established that there is no node in the superconducting gap of single-layer FeSe (Fig. 6.5c). We note that there is a slight difference in the gap size obtained from the two samples: The sample #1 shows a superconducting gap of (13 ± 2) meV, whereas the sample #2 has a gap of (15 ± 2) meV. This is related to the slight variation in the sample preparation and annealing conditions, since the carrier concentration of the FeSe film is very sensitive

to those processes. A detailed doping (carrier concentration)-dependent study of the single-layer FeSe films and the related phase diagram will be presented in the next chapter.

6.6 Discussion

While the electronic structure of the FeSe single-layer films bears some resemblances to that of $A_x\text{Fe}_{2-y}\text{Se}_2$ superconductors [15–18], the spectroscopic identification of high T_c superconductivity in the single-layer FeSe system is both interesting and profound. The observed distinct Fermi surface topology and nearly isotropic nodeless superconducting gap have provided decisive information on understanding the physics and superconductivity mechanism of Fe-based superconductors. First, in $A_x\text{Fe}_{2-y}\text{Se}_2$ superconductors, the coexistence of many different phases makes it controversial to determine which phase is truly superconducting [12]. The identification of superconductivity in the single-layer FeSe system provides a clear-cut case that the Fe vacancy-free FeSe phase is supportive of high-temperature superconductivity. Second, the distinct Fermi surface topology in single-layer FeSe, in particular the complete absence of Fermi surface around the Γ point, removes any scattering channel between the Γ Fermi surface sheet and M-point Fermi surface sheet. This makes it more straightforward than that in $A_x\text{Fe}_{2-y}\text{Se}_2$ superconductors where Fermi surface sheets are still present around Γ point albeit being electron-like. Third, the 2D nature of the single-layer FeSe makes it free from the k_z complication [11]. Therefore, the observed nearly isotropic nodeless superconducting gap provides solid evidence that there is no node in this FeSe system.

The present observations have provided clear constraints and important implications on the pairing mechanism in Fe-based superconductors. Earlier experiments on Fe-based superconductors (mainly on iron arsenides) have revealed that all five Fe $3d$ orbitals contribute to the near E_F electronic structure, forming multiple Fermi surface sheets: holelike Fermi surface sheets around Γ and electron-like ones around M [25, 26]. The interband scattering between the holelike bands near Γ and the electron-like bands near M has been proposed to be responsible for electron pairing and superconductivity [26, 28–33]. However, in the current case, there is no Fermi crossing of the band near Γ point. The top of the valence band at Γ lies well below the Fermi energy (80 meV below E_F). The absence of Fermi surface around Γ point in the single-layer FeSe superconductor completely rules out the electron scattering possibility across the Fermi surface sheets between the Γ and M points. If the interband scattering scenario is still at work, electrons can only scatter across the Fermi surface sheets between M points which are predicted to result in d -wave superconducting gap [26, 34–36]. It is argued that two Fermi surface sheets around a given M point with opposite phases can give rise to gap nodes around the Fermi surface [37]. However, nodeless superconducting gap has been unambiguously identified in our 2D FeSe case, which does not favor such a scheme of electron scattering across M-point Fermi surface sheets as the pairing mechanism in the Fe-based supercon-

ductors. This is different from the low- T_c FeSe case ($T_c = 8$ K) where an indication of nodes in the superconducting gap has been observed [38]. Our current observations indicate that alternative pictures, such as the interaction of local Fe magnetic moment [39–43] or orbital fluctuations [44, 45], need to be invoked to understand the high-temperature superconductivity in single-layer FeSe superconductors.

While electronic structure of the superconducting single-layer FeSe films has been clearly resolved in the above ARPES results, a couple of intriguing issues still need to be addressed. First, there is a disagreement in the superconducting gap measurement between the previous tunneling results [1] and the present ARPES data. While two peaks (at 20.1 and 9.0 meV) were observed in the tunneling spectrum [1], no two-gap structure was revealed in the momentum-resolved ARPES measurements. Moreover, with the identification of only one Fermi surface near M, and a nearly isotropic superconducting gap, the observation of two gaps cannot be explained by multiple gaps on different Fermi surface sheets, as found in other Fe-based superconductors like (Ba, K)Fe₂Se₂ [19, 20]. We also notice that tunneling is a local probe; therefore, it is unlikely that two peaks can be attributed to phase separation on such a small scale. Second, the 20.1 meV superconducting gap in the tunneling spectrum is also much larger than the maximum superconducting gap obtained by ARPES measurements on the current two samples. A major reason for this gap size difference is related to the carrier concentration of the FeSe sample, as will be elaborated in the next chapter that the superconducting gap size can be tuned by careful control of the carrier concentration. Third is whether the observed superconductivity is due to FeSe itself or the interface between the FeSe and the SrTiO₃ substrate. This is a critical issue to be addressed since the T_c of the single-layer film is much higher than its bulk counterpart. We notice that the overall electronic structure of the single-layer FeSe is similar to that of A_xFe_{2–y}Se₂ superconductors. In particular, the electron-like γ Fermi surface is consistent with the band structure calculations of FeSe, and the energy gap on this particular Fermi surface closes at high temperature. On the other hand, we do not see signature of possible two-dimensional electron gas from the interface, since no electron-like Fermi surface around the Γ point is observed. These observations seem to favor the attribution of superconductivity to the FeSe layer. Nevertheless, the interface should have played a key role in realizing the high T_c superconductivity. We notice that the lattice constant for bulk FeSe is $a = 3.76$ Å and for SrTiO₃, it is $a = 3.905$ Å. Therefore, an apparent lattice mismatch between FeSe and SrTiO₃ is expected to exert a strong tensile strain on the FeSe layer when FeSe is epitaxially grown on SrTiO₃(001) substrate. Such a tensile pressure on FeSe layer may play an important role, as it has been shown that superconductivity in FeSe is rather sensitive to high pressure [7, 10]. Meanwhile, charge transfer might also take place from SrTiO₃ substrate to the FeSe film through the interface, which would then change the carrier density of the single-layer FeSe films. Nevertheless, we cannot fully rule out interface superconductivity in this system, and one conjecture related to the two superconducting gaps is that both the FeSe thin film and the interface between FeSe and SrTiO₃ become superconducting with different gap sizes. Further studies to address these questions will definitely provide more crucial information on achieving and designing new superconductors with even higher T_c .

References

1. Wang, Q., Li, Z., Zhang, W., Zhang, Z., Zhang, J., Li, W., Ding, H., Ou, Y., Deng, P., Chang, K., Wen, J., Song, C., He, K., Jia, J., Ji, S., Wang, Y., Wang, L., Chen, X., Ma, X., Xue, Q.-K.: Interface-induced high-temperature superconductivity in single unit-cell FeSe films on SrTiO₃. *Chin. Phys. Lett.* **29**(3), 037402 (2012)
2. Kamihara, Y., Watanabe, T., Hirano, M., Hosono, H.: Iron-based layered superconductor LaO_{1-x}F_xFeAs ($x = 0.05-0.12$) with $T_c = 26$ K. *J. Am. Chem. Soc.* **130**(11), 32963297 (2008)
3. Ren, Z.-A., Lu, W., Yang, J., Yi, W., Shen, X.-L., Li, Z.-C., Che, G.-C., Dong, X.-L., Sun, L.-L., Zhou, F., Zhao, Z.-X.: Superconductivity at 55 K in iron-based f-doped layered quaternary compound SmO_{1-x}F_xFeAs. *Chin. Phys. Lett.* **25**(6), 2215 (2008)
4. Rotter, M., Tegel, M., Johrendt, D.: Superconductivity at 38 K in the iron arsenide (Ba_{1-x}K_x)Fe₂As₂. *Phys. Rev. Lett.* **101**(10), 107006 (2008)
5. Hsu, F.C., Luo, J.Y., Yeh, K.W., Chen, T.K., Huang, T.W., Wu, P.M., Lee, Y.C., Huang, Y.L., Chu, Y.Y., Yan, D.C., Wu, M.K.: Superconductivity in the PbO-type structure α -FeSe. *Proc. Natl. Acad. Sci. USA* **105**(38), 14262-14264 (2008)
6. Wang, X.C., Liu, Q.Q., Lv, Y.X., Gao, W.B., Yang, L.X., Yu, R.C., Li, F.Y., Jin, C.Q.: The superconductivity at 18 K in LiFeAs system. *Solid State Commun.* **148**(11), 538-540 (2008)
7. Medvedev, S., McQueen, T.M., Troyan, I.A., Palasyuk, T., Eremets, M.I., Cava, R.J., Naghavi, S., Casper, F., Ksenofontov, V., Wortmann, G., Felser, C.: Electronic and magnetic phase diagram of β -Fe_{1.01}Se with superconductivity at 36.7 K under pressure. *Nat. Mater.* **8**(8), 630-633 (2009)
8. Guo, J., Jin, S., Wang, G., Wang, S., Zhu, K., Zhou, T., He, M., Chen, X.: Superconductivity in the iron selenide K_xFe₂Se₂ ($0 \leq x \leq 1.0$). *Phys. Rev. B* **82**(18), 180520(R) (2010)
9. Fang, M.H., Wang, H.D., Dong, C.H., Li, Z.J., Feng, C.M., Chen, J., Yuan, H.Q.: Fe-based superconductivity with $T_c = 31$ K bordering an antiferromagnetic insulator in (Tl, K)Fe_xSe₂. *Europhys. Lett.* **94**(2), 27009 (2011)
10. Sun, L., Chen, X.J., Guo, J., Gao, P., Huang, Q.Z., Wang, H., Fang, M., Chen, X., Chen, G., Zhang, C., Gu, D., Dong, X., Wang, L., Yang, K., Li, A., Dai, X., Mao, H., Zhao, Z.-X.: Re-emerging superconductivity at 48 k in iron chalcogenides. *Nature* **483**(7387), 67-69 (2012)
11. Zhang, Y., Ye, Z.R., Ge, Q.Q., Chen, F., Jiang, J., Xu, M., Xie, B.P., Feng, D.L.: Nodal superconducting-gap structure in ferropnictide superconductor BaFe₂(As_{0.7}P_{0.3})₂. *Nat. Phys.* **8**(5), 371-375 (2012)
12. Mou, D.X., Zhao, L., Zhou, X.J.: Structural, magnetic and electronic properties of the iron-chalcogenide A_xFe_{2-y}Se₂ (A = K, Cs, Rb, and Tl, etc.) superconductors. *Front. Phys.* **6**(4), 410-428 (2011)
13. Liu, G., Wang, G., Zhu, Y., Zhang, H., Zhang, G., Wang, X., Zhou, Y., Zhang, W., Liu, H., Zhao, L., Meng, J., Dong, X., Chen, C., Xu, Z., Zhou, X.J.: Development of a vacuum ultraviolet laser-based angle-resolved photoemission system with a superhigh energy resolution better than 1 meV. *Rev. Sci. Instrum.* **79**(2), 023105 (2008)
14. Liu, D., Zhang, W., Mou, D., He, J., Ou, Y.B., Wang, Q.Y., Li, Z., Wang, L., Zhao, L., He, S., Peng, Y., Liu, X., Chen, C., Yu, L., Liu, G., Dong, X., Zhang, J., Chen, C., Xu, Z., Hu, J., Chen, X., Ma, X., Xue, Q., Zhou, X.J.: Electronic origin of high-temperature superconductivity in single-layer FeSe superconductor. *Nat. Commun.* **3**, 931 (2012)
15. Zhang, Y., Yang, L.X., Xu, M., Ye, Z.R., Chen, F., He, C., Xu, H.C., Jiang, J., Xie, B.P., Ying, J.J., Wang, X.F., Chen, X.H., Hu, J.P., Matsunami, M., Kimura, S., Feng, D.L.: Nodeless superconducting gap in A_xFe₂Se₂ (A = K, Cs) revealed by angle-resolved photoemission spectroscopy. *Nat. Mater.* **10**(4), 273-277 (2011)
16. Mou, D., Liu, S., Jia, X., He, J., Peng, Y., Zhao, L., Yu, L., Liu, G., He, S., Dong, X., Zhang, J., Wang, H., Dong, C., Fang, M., Wang, X., Peng, Q., Wang, Z., Zhang, S., Yang, F., Xu, Z., Chen, C., Zhou, X.J.: Distinct Fermi surface topology and nodeless superconducting gap in a (Tl_{0.58}Rb_{0.42})Fe_{1.72}Se₂ superconductor. *Phys. Rev. Lett.* **106**(10), 107001 (2011)

17. Zhao, L., Mou, D., Liu, S., Jia, X., He, J., Peng, Y., Yu, L., Liu, X., Liu, G., He, S., Dong, X., Zhang, J., He, J.B., Wang, D.M., Chen, G.F., Guo, J.G., Chen, X.L., Wang, X., Peng, Q., Wang, Z., Zhang, S., Yang, F., Xu, Z., Chen, C., Zhou, X.J.: Common Fermi-surface topology and nodeless superconducting gap of K_{0.68}Fe_{1.79}Se₂ and (Tl_{0.45}K_{0.34})Fe_{1.84}Se₂ superconductors revealed via angle-resolved photoemission. *Phys. Rev. B* **83**(14), 140508(R) (2011)
18. Qian, T., Wang, X.P., Jin, W.C., Zhang, P., Richard, P., Xu, G., Dai, X., Fang, Z., Guo, J.-G., Chen, X.-L., Ding, H.: Absence of a holelike Fermi surface for the iron-based K_{0.8}Fe_{1.7}Se₂ superconductor revealed by angle-resolved photoemission spectroscopy. *Phys. Rev. Lett.* **106**(18), 187001 (2011)
19. Zhao, L., Liu, H., Zhang, W., Meng, J., Jia, X., Liu, G., Dong, X., Chen, G., Luo, J., Wang, N., Lu, W., Wang, G., Zhou, Y., Zhu, Y., Wang, X., Xu, Z., Chen, C., Zhou, X.J.: Multiple nodeless superconducting gaps in (Ba_{0.6}K_{0.4})Fe₂As₂ superconductor from angle-resolved photoemission spectroscopy. *Chin. Phys. Lett.* **25**(12), 4402 (2008)
20. Ding, H., Richard, P., Nakayama, K., Sugawara, K., Arakane, T., Sekiba, Y., Takayama, A., Souma, S., Sato, T., Takahashi, T., Wang, Z., Dai, X., Fang, Z., Chen, G.F., Luo, J.L., Wang, N.L.: Observation of Fermi-surface-dependent nodeless superconducting gaps in Ba_{0.6}K_{0.4}Fe₂As₂. *Europhys. Lett.* **83**(4), 47001 (2008)
21. Evtushinsky, D.V., Inosov, D.S., Zabolotnyy, V.B., Koitzsch, A., Knupfer, M., Büchner, B., Viazovska, M.S., Sun, G.L., Hinkov, V., Boris, A.V., Lin, C.T., Keimer, B., Varykhalov, A., Kordyuk, A.A., Borisenko, S.V.: Momentum dependence of the superconducting gap in Ba_{1-x}K_xFe₂As₂. *Phys. Rev. B* **79**(5), 054517 (2009)
22. Wray, L., Qian, D., Hsieh, D., Xia, Y., Li, L., Checkelsky, J.G., Pasupathy, A., Gomes, K.K., Parker, C.V., Fedorov, A.V., Chen, G.F., Luo, J.L., Yazdani, A., Ong, N.P., Wang, N.L., Hasan, M.Z.: Momentum dependence of superconducting gap, strong-coupling dispersion kink, and tightly bound Cooper pairs in the high-T_c (Sr, Ba)_{1-x}(K, Na)_xFe₂As₂ superconductors. *Phys. Rev. B* **78**(18), 184508 (2008)
23. Tamai, A., Ganin, A.Y., Rozbicki, E., Bacsá, J., Meevasana, W., King, P.D.C., Caffio, M., Schaub, R., Margadonna, S., Prassides, K., Rosseinsky, M.J., Baumberger, F.: Strong electron correlations in the normal state of the iron-based FeSe_{0.42}Te_{0.58} superconductor observed by angle-resolved photoemission spectroscopy. *Phys. Rev. Lett.* **104**(9), 097002 (2010)
24. Ni, N., Tillman, M.E., Yan, J.Q., Kracher, A., Hannahs, S.T., Bud'ko, S.L., Canfield, P.C.: Effects of Co substitution on thermodynamic and transport properties and anisotropic H_{c2} in Ba(Fe_{1-x}Co_x)₂As₂ single crystals. *Phys. Rev. B* **78**(21), 214515 (2008)
25. Singh, D.J., Du, M.H.: Density functional study of LaFeAsO_{1-x}F_x: a low carrier density superconductor near itinerant magnetism. *Phys. Rev. Lett.* **100**(23), 237003 (2008)
26. Kuroki, K., Onari, S., Arita, R., Usui, H., Tanaka, Y., Kontani, H., Aoki, H.: Unconventional pairing originating from the disconnected Fermi surfaces of superconducting LaFeAsO_{1-x}F_x. *Phys. Rev. Lett.* **101**(8), 087004 (2008)
27. Norman, M.R., Randeria, M., Ding, H., Campuzano, J.C.: Phenomenology of the low-energy spectral function in high-T_c superconductors. *Phys. Rev. B* **57**, 11093–11096(R) (1998)
28. Mazin, I.I., Singh, D.J., Johannes, M.D., Du, M.H.: Unconventional superconductivity with a sign reversal in the order parameter of LaFeAsO_{1-x}F_x. *Phys. Rev. Lett.* **101**(5), 057003 (2008)
29. Mazin, I.I., Johannes, M.D.: A key role for unusual spin dynamics in ferropnictides. *Nat. Phys.* **5**(2), 141–145 (2009)
30. Wang, F., Zhai, H., Lee, D.H.: Antiferromagnetic correlation and the pairing mechanism of the cuprates and iron pnictides: a view from the functional renormalization group studies. *Europhys. Lett.* **85**(3), 37005 (2009)
31. Wang, F., Zhai, H., Ran, Y., Vishwanath, A., Lee, D.H.: Functional renormalization-group study of the pairing symmetry and pairing mechanism of the FeAs-based high-temperature superconductor. *Phys. Rev. Lett.* **102**(4), 047005 (2009)
32. Chubukov, A.V., Efremov, D.V., Eremin, I.: Magnetism, superconductivity, and pairing symmetry in iron-based superconductors. *Phys. Rev. B* **78**(13), 134512 (2008)
33. Stanev, V., Kang, J., Tesanovic, Z.: Spin fluctuation dynamics and multiband superconductivity in iron pnictides. *Phys. Rev. B* **78**, 184509 (2008)

34. Maier, T.A., Graser, S., Hirschfeld, P.J., Scalapino, D.J.: *d*-wave pairing from spin fluctuations in the $K_x\text{Fe}_{2-y}\text{Se}_2$ superconductors. *Phys. Rev. B* **83**(10), 100515(R) (2011)
35. Wang, F., Yang, F., Gao, M., Lu, Z.Y., Xiang, T., Lee, D.H.: The electron pairing of $K_x\text{Fe}_{2-y}\text{Se}_2$. *Europhys. Lett.* **93**(5), 57003 (2011)
36. Das, T., Balatsky, A.V.: Stripes, spin resonance, and nodeless d-wave pairing symmetry in Fe_2Se_2 -based layered superconductors. *Phys. Rev. B* **84**(1), 014521 (2011)
37. Mazin, I.I.: Symmetry analysis of possible superconducting states in $K_x\text{Fe}_y\text{Se}_2$ superconductors. *Phys. Rev. B* **84**(2), 024529 (2011)
38. Song, C.L., Wang, Y.L., Cheng, P., Jiang, Y.P., Li, W., Zhang, T., Li, Z., He, K., Wang, L., Jia, J.-F., Hung, H.-H., Wu, C., Ma, X., Chen, X., Xue, Q.-K.: Direct observation of nodes and twofold symmetry in FeSe superconductor. *Science* **332**(6036), 1410–1413 (2011)
39. Yildirim, T.: Origin of the 150-K anomaly in LaFeAsO: competing antiferromagnetic interactions, frustration, and a structural phase transition. *Phys. Rev. Lett.* **101**(5), 057010 (2008)
40. Si, Q., Abrahams, E.: Strong correlations and magnetic frustration in the high T_c iron pnictides. *Phys. Rev. Lett.* **101**(7), 076401 (2008)
41. Wu, J., Phillips, P., Neto, A.C.: Theory of the magnetic moment in iron pnictides. *Phys. Rev. Lett.* **101**(12), 126401 (2008)
42. Fang, C., Yao, H., Tsai, W.F., Hu, J., Kivelson, S.A.: Theory of electron nematic order in LaFeAsO. *Phys. Rev. B* **77**(22), 224509 (2008)
43. Xu, C., Müller, M., Sachdev, S.: Ising and spin orders in the iron-based superconductors. *Phys. Rev. B* **78**(2), 020501(R) (2008)
44. Saito, T., Onari, S., Kontani, H.: Emergence of fully gapped s_{++} -wave and nodal d-wave states mediated by orbital and spin fluctuations in a ten-orbital model of KFe_2Se_2 . *Phys. Rev. B* **83**(14), 140512 (2011)
45. Lv, W., Lee, W.C., Phillips, P.: Vacancy-driven orbital and magnetic order in $(\text{K}, \text{Tl}, \text{Cs})_y\text{Fe}_{2-x}\text{Se}_2$. *Phys. Rev. B* **84**(15), 155107 (2011)

Chapter 7

Phase Diagram and High T_c Superconductivity in Single-Layer FeSe Films

Much recent interest has been generated by the discovery of high temperature superconductivity in the single-layer FeSe films [1, 2]. While theoretical attempts have been made to understand its origin [3, 5], it is crucial to experimentally identify how the superconductivity appears in this system. It has been established that, in both high temperature cuprate superconductors [4, 6] and Fe-based superconductors [7–11], superconductivity is induced by doping charge carriers into the parent compound to suppress the antiferromagnetic state. Moreover, the superconducting transition temperature (T_c) can be optimized by tuning the carrier concentration. Therefore, it is important to identify whether the superconductivity in the single-layer FeSe film is realized by suppressing another competing phase and whether the T_c can be enhanced by optimized carrier concentration.

In this chapter, we will present an electronic phase diagram for the single-layer FeSe film grown on SrTiO₃ substrate. The charge carrier concentration has been tuned over a wide range through an extensive annealing procedure. Two distinct phases that compete during the annealing process have been clearly identified. For clarity, we call the electronic phase at low doping as N phase in which no superconductivity is observed. The electronic structure of the N phase bears some resemblances to that of the antiferromagnetic parent compound of the Fe-based superconductors. Another phase (S phase) appears with the increase of carrier concentration and the suppression of the N phase. S phase shows distinct electronic band structure from that of the N phase, on which superconductivity is observed when the carrier concentration reaches a critical value. The superconducting transition temperature T_c is also tunable with carrier concentration. A maximum T_c of 65 ± 5 K was found at the optimal doping.

7.1 Introduction

Superconductivity in cuprates is realized by doping charge carriers into the parent Mott insulator, which concomitantly suppresses the antiferromagnetic state [6]. Understanding the phase diagram of cuprates has been believed to be a prerequisite

to unravel the origin of high-temperature superconductivity. In the doping process, multiple phases with distinct physical properties have emerged (e.g., from an antiferromagnetic insulator, to a superconductor and eventually to a non-superconducting normal metal). Moreover, the transition temperature T_c can be tuned by the carrier concentration in the superconducting region, which initially goes up with the increasing doping, reaches a maximum at an optimal doping, and then goes down with further doping [6]. Such a rich phase diagram and doping evolution not only provide a handle to tune the physical properties in a dramatic way, but also give clues and constraints in understanding the origin of the high- T_c superconductivity. A similar phase diagram is observed in Fe-based superconductors where the superconductivity is achieved by doping the parent magnetic compounds [12, 13]. The superconducting transition temperature has also been found tunable with a maximum at the optimal doping. Again, this rich doping evolution is key to understand the origin of high-temperature superconductivity in Fe-based superconductors.

The recent discovery of high-temperature superconductivity in single-layer FeSe films [1, 2] has attracted much interest for a couple of reasons. First, the high T_c observed in this material may break the T_c record (~ 55 K) in the bulk Fe-based superconductors [7–11, 14]. Second, the T_c in the single-layer FeSe film is incredibly high compared to its bulk counterpart which shows a T_c of 8 K [10] at normal pressure and 36.7 K under high pressure [15]. Third, the single-layer FeSe film provides an ideal system to investigate the origin of high-temperature superconductivity. On one hand, this system consists of only a single-layer FeSe, which represents the simplest building block of FeSe-based superconductors with a strict two-dimensionality. Its simple electronic structure may provide the key insight and constraint on the superconducting mechanism in Fe-based compounds [2]. On the other hand, the interface between the single-layer FeSe film and the SrTiO₃ substrate may play an important role in this system which points to a unique pathway toward interface induced or enhanced high- T_c superconductivity [1].

Similar to the research in cuprates and other Fe-based superconductors, exploring the electronic phase diagram versus carrier concentration in single-layer FeSe system can provide key information in understanding this system. In this chapter, the doping-dependent phase diagram of single-layer FeSe film will be presented. The superconducting transition temperature has also been optimized by carrier doping with a maximum T_c at (65 ± 5) K.

7.2 Materials and Methods

7.2.1 Thin Film Preparation and Post-Annealing

The single-layer FeSe thin films used in this study were grown on SrTiO₃(001) substrate by the molecular beam epitaxy (MBE) method. The scanning tunneling microscope was used to characterize the as-grown thin films. Details for the sample

preparation are similar to those reported in [1]. An amorphous Se capping layer was deposited on the sample surface in order to transfer the single-layer FeSe thin film from the MBE chamber to a different sample treatment chamber which is directly connected to the ARPES measurement chamber. Sample annealing was carried out in the treatment chamber in ultrahigh vacuum. In order to keep track of the evolution of the electronic structure, the annealing was split into many steps at different temperatures and for different times. ARPES measurements on the band structure, Fermi surface, and the energy gap were carried out after each annealing.

Shown in Fig. 7.1 are the annealing conditions for two typical single-layer FeSe film samples. Each bar represents an annealing sequence. Different colors represent different annealing temperatures, and the height of the bar marks the annealing time. The annealing process was carried out sequentially on each sample, and each ARPES measurement represents an accumulative effect to the sample by all the annealing sequences before that measurement. For example, the sample #1 has been annealed nine times, denoted as nine annealing sequences 1–9 in Fig. 7.1. For the annealing sequence 1, the as-grown film was annealed at 190 °C for half an hour to remove the amorphous Se capping. After the annealing sequence 9, the film sample #1 has been annealed in vacuum altogether at 190 °C for 13.3 hours and at 250 °C for 13.5 h. The same is true for the sample #2. It has been annealed for 6 times, denoted as sequences from 10 to 15. For the annealing sequence 10, the film was first annealed at 190 °C for 2 h and then at 250 °C for another 2 h. After the last sequence 15, the sample #2 has been annealed altogether at 190 °C for 2 h, at 250 °C for 2 h, at 190 °C for 10 h, at 360 °C for 2 h, and finally at 400 °C for 7.7 h.

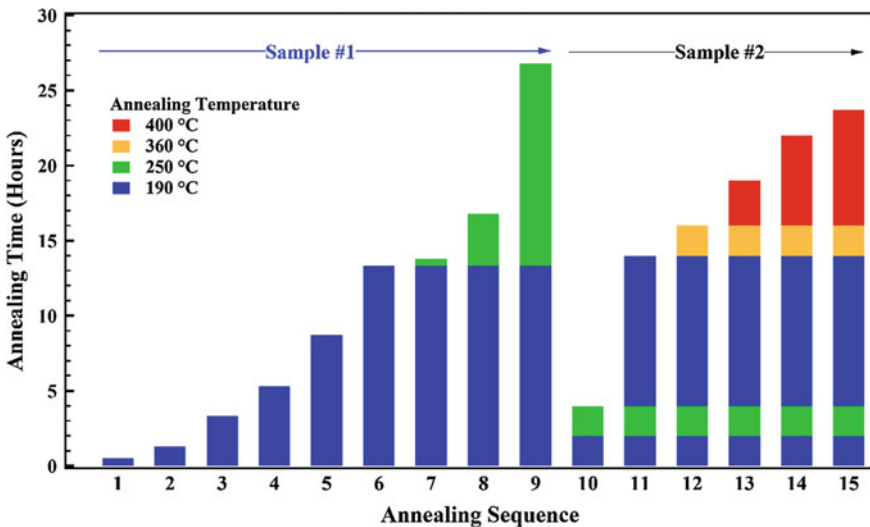


Fig. 7.1 Annealing conditions for the single-layer FeSe thin films

7.2.2 *Sample Temperature Calibration*

Similar to the case described in the last chapter, the thermal conductivity between the single-layer FeSe film and the sample holder was weakened by the SrTiO₃ substrate that was tightened on the sample holder by copper pads. Therefore, the usual sample temperature, which was calibrated for the sample directly glued on the sample holder, can only set a lower limit to the temperature of the FeSe film. The upper limit of the film temperature was determined by measuring a piece of polycrystalline gold foil glued on a similar SrTiO₃ substrate and mounted in the sampler holder using the same way. The temperature of the gold can be obtained by fitting the gold Fermi edge broadening with the Fermi distribution function. Since the Fermi edge width contains a couple of contributions including the temperature broadening, instrumental resolution, and cleanliness of gold, this method sets an upper limit to the gold temperature which represents the real temperature of the FeSe film grown on SrTiO₃. A difference of ~ 10 K was observed between the lower and upper temperature limits. Therefore, it is reasonable to believe that the real temperature of the FeSe thin film lies in between, with an error bar of ± 5 K.

7.2.3 *High-Resolution ARPES Methods*

The angle-resolved photoemission measurements were carried out on our ARPES system with a high resolution. Helium discharge lamp was used as the light source with the photon energy of 21.218 eV. The energy resolution of the Scienta R4000 electron energy analyzer was set at $10 \sim 20$ meV for the Fermi surface mapping and band structure measurements and at $4 \sim 10$ meV for the superconducting gap measurements. The angular resolution was ~ 0.3 degree. The Fermi level of the FeSe thin films was referenced to that of a clean polycrystalline gold electrically connected to the sample. The base pressure for the measurement chamber was better than 5×10^{-11} Torr.

7.3 Coexistence and Evolution of Two Competing Phases

7.3.1 *Observation of Two Competing Phases and Their Evolution with Carrier Concentration*

In fact, the as-prepared single-layer FeSe film grown at relatively low temperature is non-superconducting. Superconductivity is only realized by annealing in vacuum at a relatively high temperature for a certain amount of time. In order to study the evolution of the electronic structure during the annealing process, small annealing

steps were used with gradually increased temperature and time, as shown in Fig. 7.1 and discussed in the Materials and Methods section. ARPES measurements on the band structure, Fermi surface, and energy gap were carried out after each in situ annealing. It is interesting to note that the starting point of the electronic structure may vary between samples due to slight variation in the SrTiO₃ substrates and the initial preparation conditions of the single-layer FeSe thin films. However, the annealing process for all the samples follows the same trend. The typical evolution of the Fermi surface (or constant energy map) and band structure is shown in Figs. 7.2 and 7.3, respectively. We have worked on many samples, and the results are highly reproducible. Nevertheless, we also notice that the thin-film quality might get worse after extensive annealing sequences. Therefore, two typical samples (#1 and #2) with different starting points are presented to cover the entire annealing process with good data quality.

Figure 7.2 shows the Fermi surface evolution of the two single-layer FeSe samples at different annealing stages. The corresponding band structures are shown in Fig. 7.3. For convenience, we denote different samples after different annealing conditions by the annealing sequences hereafter. The exact annealing condition for each sequence can be found in Fig. 7.1 in the Materials and Methods section. Dramatic changes can be clearly seen in both the Fermi surface and the band structure during the annealing process. Before we move forward and discuss the possible origins behind, a direct question to address is the possible signal from the SrTiO₃ substrate since the thin film is only one layer and an annealing process is supposed to be a key step to see

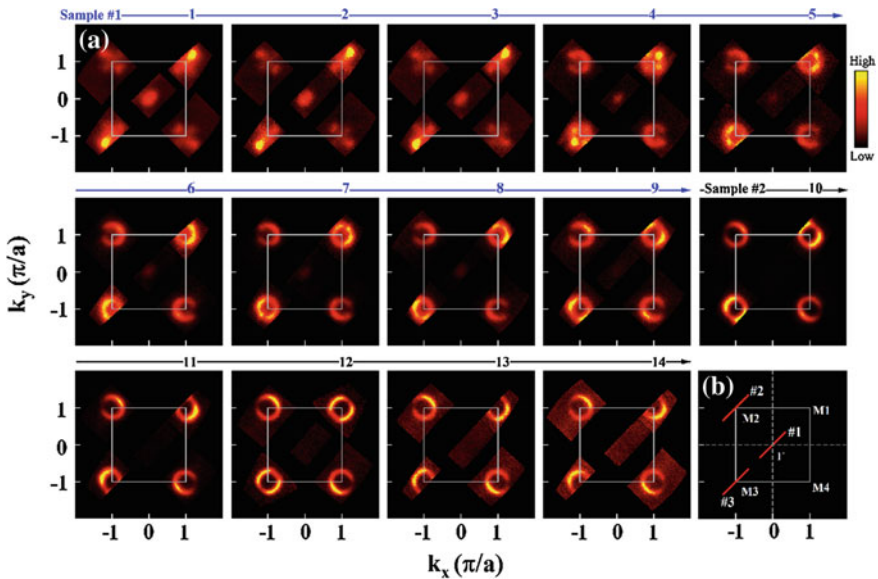


Fig. 7.2 **a** Fermi surface evolution of the single-layer FeSe film during annealing. **b** The locations of the high symmetry cuts [16]

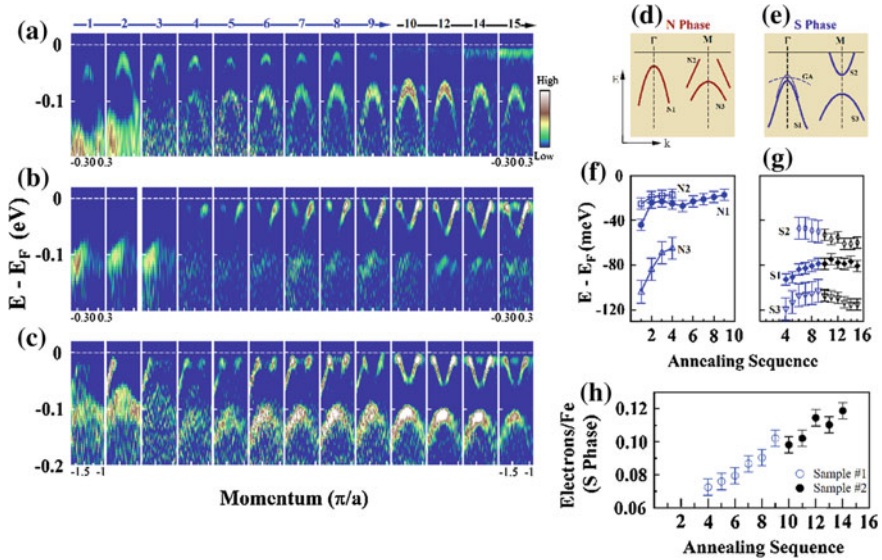


Fig. 7.3 Band structure evolution during annealing. **a** Evolution of band structure (second derivative image) for the cut near Γ . **b** Evolution of band structure (second derivative image) for the cut near M2. **c** Evolution of band structure (second derivative image) for the cut near M3. Schematic band structure of the N phase (**d**) and S phase (**e**). Evolution of band *top* and *bottom* of N phase (**f**) and S phase (**g**). **h** Electron concentration estimated from the Fermi surface in the S phase [16]

clear bands when SrTiO₃ single crystal was directly measured. In order to check on this point, a SrTiO₃ substrate was prepared using the same procedure as that in making single-layer FeSe thin films, and then annealed by the similar process as used for the FeSe films. Careful ARPES measurements on this SrTiO₃ substrate clearly indicate that none of the electronic bands presented in this book was from the SrTiO₃ substrate. The evolution of these bands represents the intrinsic change of the electronic structure in the FeSe thin films.

As shown in Figs. 7.2 and 7.3, two distinct phases can be clearly identified during the annealing process. The electronic structure is similar in the initial stage (sequences 1–3) which represents a pure phase distinct from the superconducting phase reported in the last chapter. For simplicity, we call it N phase hereafter. The schematic band structure of the N phase is shown in Fig. 7.3d. The momentum dependence of the spectral weight distribution near Fermi level is mainly characterized by two “strong spots” near M point. We notice that some spectral weight can also be seen near Γ point in the N phase constant energy map near Fermi level (spectral weight integration over the energy window $[-0.03$ eV, -0.01 eV]; Fig. 7.2 sequences 1–3). This is because the valence band top is close to the Fermi level at Γ (N1 band in Fig. 7.3d). Another set of bands start to appear from the sequence 4 and get more and more

pronounced with annealing. Meanwhile, the bands corresponding to the N phase decrease in intensity and completely disappear after the sequence 10 (Fig. 7.3a–c). The electronic band structure for the sequence 10 and thereafter is similar to that of the superconducting phase presented in the last chapter. The schematic band structure is shown in Fig. 7.3e, and we call it S phase hereafter. The Fermi surface of the S phase is characterized by electron-like pockets around the M point (Fig. 7.2) [2]. The band structure of the S phase (Fig. 7.3) bears a clear resemblance to that of $A_x\text{Fe}_{2-y}\text{Se}_2$ superconductors [17–20]. It seems that the N phase is stable when the annealing temperature is relatively low and the annealing time is relatively short. On the contrary, the S phase becomes dominant after extensive annealing with relatively high annealing temperature. We notice that the band structure in the intermediate stage is a mixture of the N phase and S phase and the corresponding Fermi surface also contains both “strong spots” and electron-like pockets near the M point. While further investigations are needed to pin down the origin of the intermediate state, it is possible that there is a real space phase separation on the single-layer film during the N to S phase transition. Alternatively, it is also possible that there are isolated double-layer islands on the thin film which remains in the N phase when the major single-layer region enters S phase, because it is known that the double-layer films are harder to be doped by annealing. If this scenario is at work, it is natural to ask whether the N phase only belongs to double-layer islands, and the single-layer region can only show S phase. However, this possibility can be ruled out by the pure N phase (without any signal from S phase) observed in sequences 1 to 3, because the STM measurements have demonstrated that the major region of the film is single-layer FeSe. Therefore, both N phase and S phase are intrinsic for the single-layer FeSe film grown on SrTiO_3 .

The phase transition from N phase to S phase is characterized by two sets of distinct bands. For a given phase, the number and overall shape of the electronic bands are the same. Nevertheless, when a quantitative analysis is performed on each band versus annealing, a moderate change of the band structure can be clearly resolved (Fig. 7.3a–c), signaling a change of the carrier concentration in these two phases. As shown in Fig. 7.3f and g, the change of the bands shows different trends and magnitudes which indicates that the doping-induced change is not a rigid-band shift. In S phase, the Fermi surface size can be well characterized by calculating the area of the two degenerate electron-like Fermi pockets near M, such that the doping level can be obtained. Shown in Fig. 7.3h is the estimated doping versus annealing, which confirms that electrons are indeed doped into the single-layer FeSe film with doping. On the other hand, the effective mass for the electron-like band near M is around $3 m_e$ (where m_e represents a static mass of an electron) and shows little change with doping, as determined from its band width and Fermi momentum.

7.3.2 Electronic Structure for the N Phase, the S Phase, and the Intermediate State

Photoemission intensity plot, EDC second derivative, and raw spectra (EDCs) along three high symmetry cuts are shown in Fig. 7.4 to present the detailed band structure for the N phase (the sequence 2 of the sample #1), which dominates the initial stage of the annealing process. The momentum locations of the cuts are marked in the bottom-right inset. The electronic structure around the Γ is characterized by a hole-like band [denoted as N1 band in Figs. 7.3d and 7.4a and b]. The band structure near M3 is characterized by a hole-like band denoted as N2 band and another hole-like band denoted as N3, as shown in Fig. 7.3d. An interesting finding is that the hole-like N2 band does not cross the Fermi level but terminates below the Fermi level without showing a band top for the first few annealing sequences (sequences 1 to 3). We notice that the N2 band is very weak and is on top of a high background. Further investigations are needed to pin down the origin for the band termination.

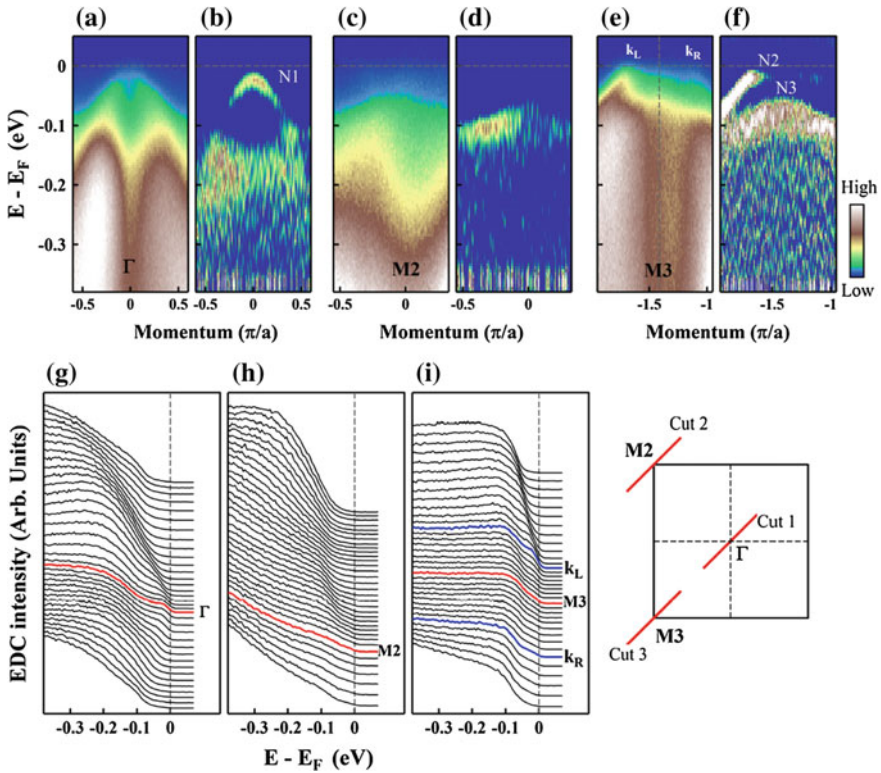


Fig. 7.4 Detailed band structure for the N phase. Photoemission intensity plot (a), the corresponding second derivative image (b), and EDCs (g) for cut1 crossing Γ . c, d, and h are the same but for cut2 crossing M2. e, f, and i for cut3 crossing M3

In particular, whether there is a band back-bending, whether the gap opening is due to a special electronic order, and how the gap changes with temperature are of potential interest.

The pure S phase dominates the final stage of the annealing process (e.g., annealing sequences of 10–15 for the sample #2). Photoemission intensity plot, EDC second derivative, and raw spectra (EDCs) for the S phase are also presented along the same high symmetry cuts as those for the N phase. Figure 7.5 shows the typical S phase band structure for the sequence 10 of the sample #2. The band structure around Γ is dominated by the S1 band, as denoted in Fig. 7.3e. Some other fine structures also present in the spectra; for example, a flat band labeled as GA is shown in Fig. 7.5b, the top of the S1 band is split into two sub-bands, and several other bands can be seen at high binding energy above 0.2 eV. This band structure is very similar to that observed in $K_xFe_{2-y}Se_2$. The electronic structure around M for the S phase is mainly characterized by an electron-like band S2 and a hole-like band S3. It is interesting to notice that another hole-like band S4 is also observed which shows a similar dispersion as that of S3 but locates 100 meV lower in energy (Fig. 7.5g).

In the intermediate stage of annealing (e.g., the sequences of 4–9 for the sample #1), the band structure contains components from both the N phase and S phase.

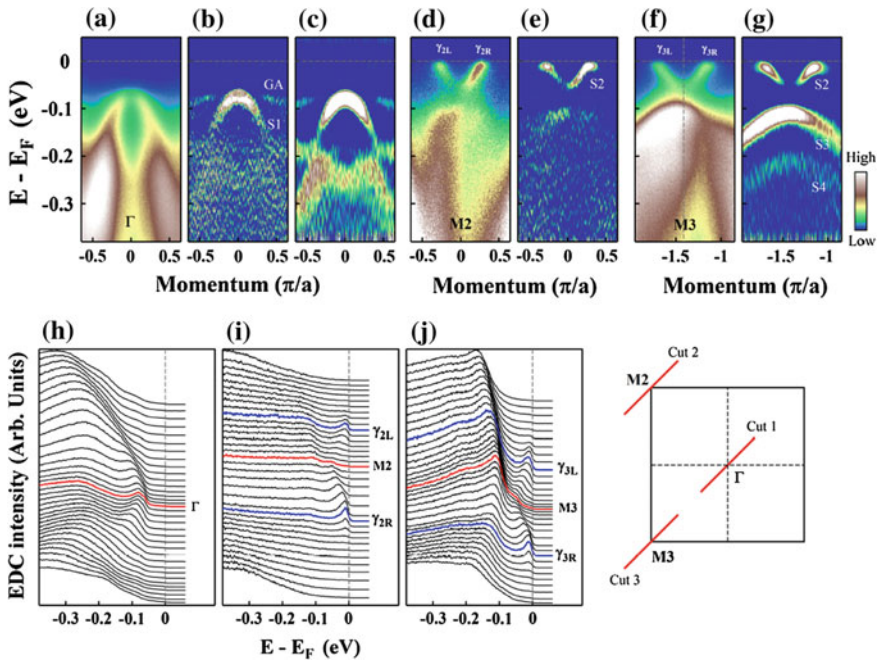


Fig. 7.5 Detailed band structure for the S phase. Photoemission intensity plot (a), the corresponding second derivative image (b and c, different smooth times), and EDCs (h) for cut1 crossing Γ . d, e, and i are the photoemission intensity plot, second derivative image, and EDCs for cut2 crossing M2. f, g, and j are the same but for cut3 crossing M3

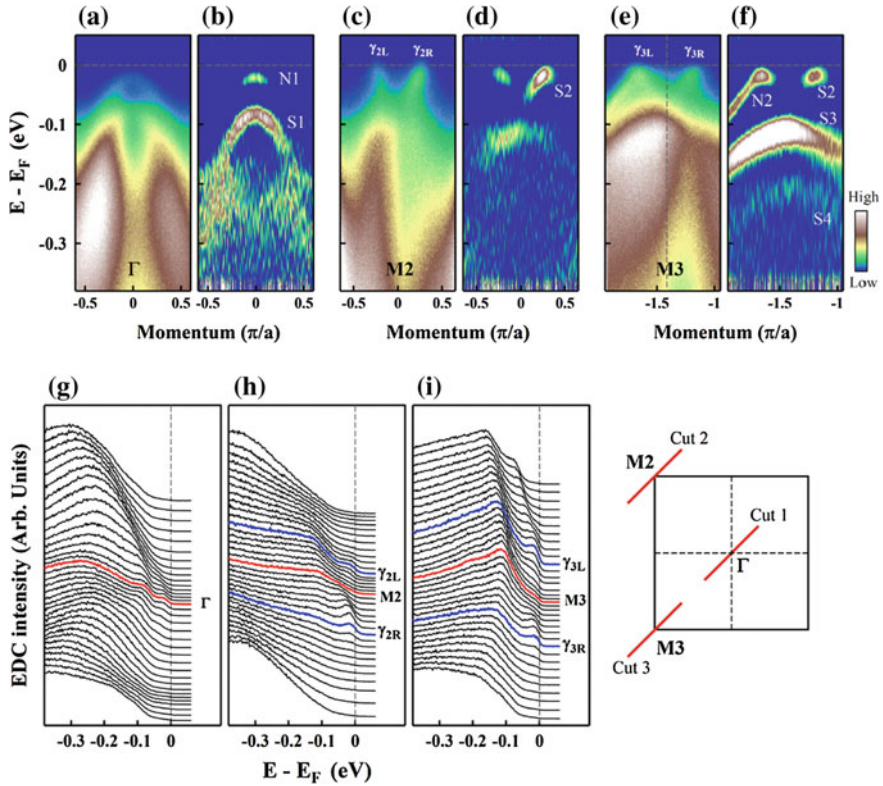


Fig. 7.6 Detailed band structure for N phase and S phase. Photoemission intensity plot (a), the corresponding second derivative image (b), and EDCs (g) for cut1 crossing Γ . c, d, and h are the same but for cut2 crossing $M2$. e, f, and i for cut3 crossing $M3$

Figure 7.6 shows the electronic structure along the three high symmetry cuts for the sequence 8 of the sample #1. As discussed before, whether this electronic structure comes from the real-space phase separation or existence of isolated double-layer islands will be interesting for future research.

7.4 Carrier Concentration Change Induced by Post-Annealing

Since dramatic phase transition has been observed with a concomitant change of the carrier concentration in a given phase, an immediate question is the origin for the carrier doping during the annealing. Since the as-grown thin film was first capped with an amorphous Se layer and then annealed in vacuum at relatively low temperature, there are a couple of possible scenarios to induce charge carriers. The first is the loss

of Se which will introduce electrons into the single-layer film. This is consistent with the observation that the electron pockets in the S phase get larger with annealing. The lost Se can come from the FeSe film itself and give rise to Se vacancies in the FeSe_{1-x} system since indication of Se vacancy in the FeSe film grown on graphene substrate was observed before by scanning electron microscope [21]. Further research to study whether similar Se vacancies can appear in the FeSe film grown on SrTiO_3 substrate will be interesting. Alternatively, the lost Se can also come from the Se capping layer. While most of the amorphous Se capping layer were removed during the first low-temperature annealing, it is possible that there are residual Se atoms on the sample surface which can take electrons from the FeSe film. These residual Se atoms get lost during the following annealing sequences and effectively dope the FeSe films with electrons. The second possibility is the loss of oxygen near the SrTiO_3 surface which can also induce electrons and dope the FeSe layer near the interface. Whether the oxygen loss can be significant enough at such a low annealing temperature remains to be investigated. While further experimental and theoretical efforts are needed to pin down the exact working mechanism, it is also possible that both scenarios are correct. In this case, the initial electrons from the oxygen loss in SrTiO_3 surface are neutralized by the residual amorphous Se atoms from the capping layer, and the electron doping is realized by the further loss of Se and/or oxygen during the following annealing. If this picture is at work, then the cooperation of the two scenarios gives us an ideal wide window to unravel the electronic phase diagram in the single-layer FeSe film.

7.5 N Phase of the Single-Layer FeSe Film and the Magnetic Phase of BaFe_2As_2

The current observation confirms that the appearance of superconductivity in single-layer FeSe film is similar to that of other Fe-based superconductors: The superconductivity is realized by suppressing another competing phase with electron doping. Therefore, it would be interesting to compare the N phase in single-layer FeSe film with the magnetic state in the parent AEFe_2As_2 (AE = Ba or Sr) compounds [22–25].

As shown in Fig. 7.7, the band structure and the spectral weight distribution of the N phase near the M point exhibit clear resemblance to that of the parent AEFe_2As_2 (AE = Ba or Sr) compounds in the magnetic state [22–25]: First, the main band structure near M in N phase is a hole-like band (Fig. 7.7c), which is labeled as N2 in Fig. 7.3d. A similar hole-like band is also observed in AEFe_2As_2 (AE = Ba or Sr) in the magnetic state [22–25] (e.g., Fig. 7.7d for BaFe_2As_2). Second, the spectral weight distribution as a function of momentum for the N phase shows “strong spots-” like feature (Fig. 7.7a). This feature is also similar to that observed in AEFe_2As_2 (AE = Ba or Sr) in the magnetic state [23, 24] (e.g., Fig. 7.7b for BaFe_2As_2).

However, there are also differences between these two phases: First, in the N phase of the single-layer FeSe film, the hole-like band does not cross the Fermi level

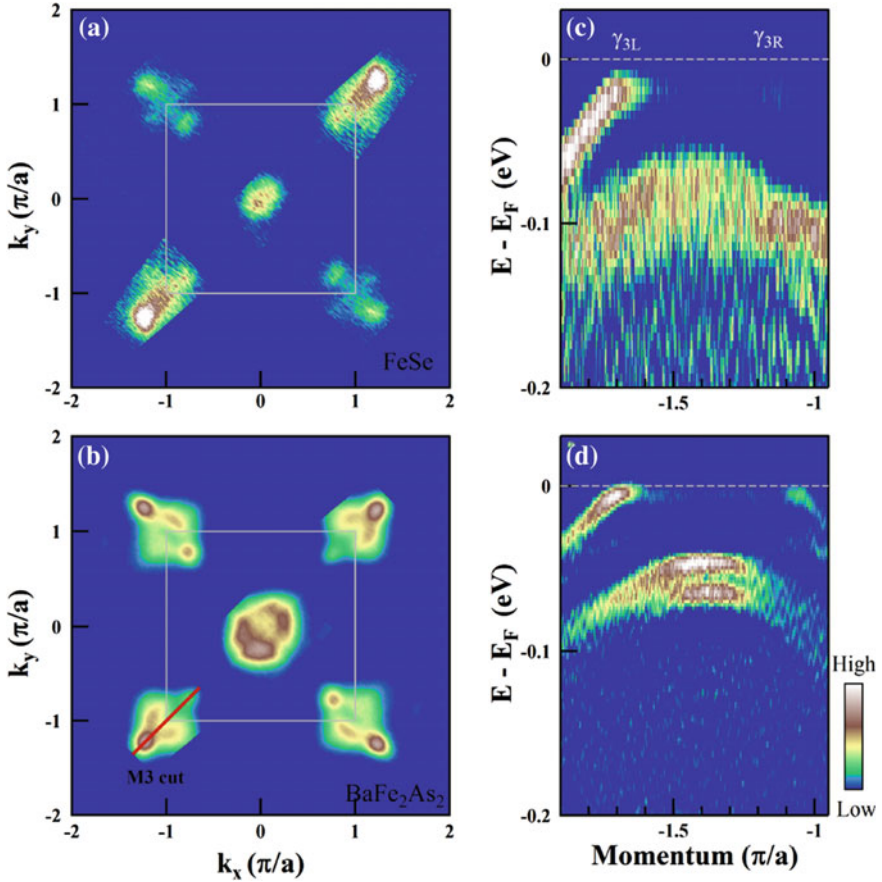


Fig. 7.7 Fermi surface mapping and band structure between the N phase of the single-layer FeSe film and BaFe_2As_2 in its magnetic state

at the initial stage of annealing process. For annealing sequence 1, its peak position of photoemission spectra (energy distribution curve, EDC) is nearly 25 meV below the Fermi level (Fig. 7.3c and f). On the contrary, the hole-like band in BaFe_2As_2 crosses the Fermi level. Second, as shown in Fig. 7.7b, in addition to the “strong spots”, there is also clear component of electron-like band present near M point in the magnetic BaFe_2As_2 [24]. No electron-like band is observed near M in the N phase of the FeSe films. Third, differences also lie in the band structure around the Γ point. While there are several hole-like bands that cross the Fermi level in BaFe_2As_2 near Γ , the bands in the N phase of the single-layer FeSe are well below the Fermi level, and no Fermi surface is observed around the Γ point.

While the N phase competes with the S phase and shows some similarities with the magnetic state in AEFe_2As_2 ($\text{AE} = \text{Ba}$ or Sr), its exact crystal structure and the physical properties remain unclear, which would stimulate future investigations.

Related to the above discussion is an interesting disparity in the electronic behavior between the Γ and M points in the single-layer FeSe film. Near Γ point, the bands are all pushed below the Fermi level. This is true for both the N phase and the S phase, which makes them distinct when compared with BaFe₂As₂ in the magnetic state [24] and bulk Fe(Se, Te) [26], respectively. On the contrary, near M point, the electronic structure of the N phase shows similarities to that of the magnetic state of BaFe₂As₂ and the bands of the S phase shows resemblance to that of the bulk Fe(Se, Te). This disparity cannot be explained by a simple rigid band shift due to electron doping in the FeSe film. It does not happen in bulk Fe(Se, Te) [26] or Ba(Fe, Co)₂As₂ [27] systems with similar doping either. We notice that the first principle band structure calculation was also carried out, but it did not provide a consistent explanation to all the observations [3]. These facts point to the importance of the SrTiO₃ substrate. We note that a strain is exerted on the FeSe film from the SrTiO₃ substrate and a strong interfacial effect is also expected between the single-layer FeSe and the SrTiO₃ [5]. Understanding the origin of this peculiar electronic characteristic of the single-layer FeSe film grown on SrTiO₃ substrate is key to unravel its exotic physical properties.

7.6 Optimization of the High-Temperature Superconductivity in the Superconducting Phase

Disregarding the particular mechanism for the electron doping with annealing, the tunability of the carrier concentration of the S phase by a simple annealing procedure offers an opportunity to investigate the superconductivity with doping. In this section, we will focus on the S phase and discuss the observation and optimization of the high-temperature superconductivity in the S phase. As shown in the last chapter, with sufficient electron doping in the S phase, the single-layer FeSe film becomes superconducting at low temperature. The superconducting gap and its temperature dependence are measured after sufficient annealing but at different annealing sequences (Fig. 7.8, sequence 10 and later) in which the relatively high T_c makes it feasible to perform the detailed measurements and avoid complications from another N phase. At each annealing sequence, photoemission spectra (EDCs) at k_F are measured at different temperatures and symmetrized following the procedure commonly used for high-temperature cuprate superconductors [28]. The symmetrization process can remove the effect of Fermi distribution function near the Fermi level and thus visually present a possible gap opening. In this case, the gap opening is characterized by a spectral dip at the Fermi level, and the gap size is determined by the EDC peak position relative to the Fermi level. The results for annealing sequences 10, 12, 13, and 15 are shown in Fig. 7.8a–d, and the corresponding gap size and its temperature dependence are shown in Fig. 7.8e–h, respectively. We note that both the gap size and the gap closing temperature increase with electron doping: The gap size increases from ~ 10 meV for the sequence 10 to ~ 19 meV for the sequence 15, whereas the gap closing temperature increases from ~ 40 K for the sequence 10 to ~ 65 K for

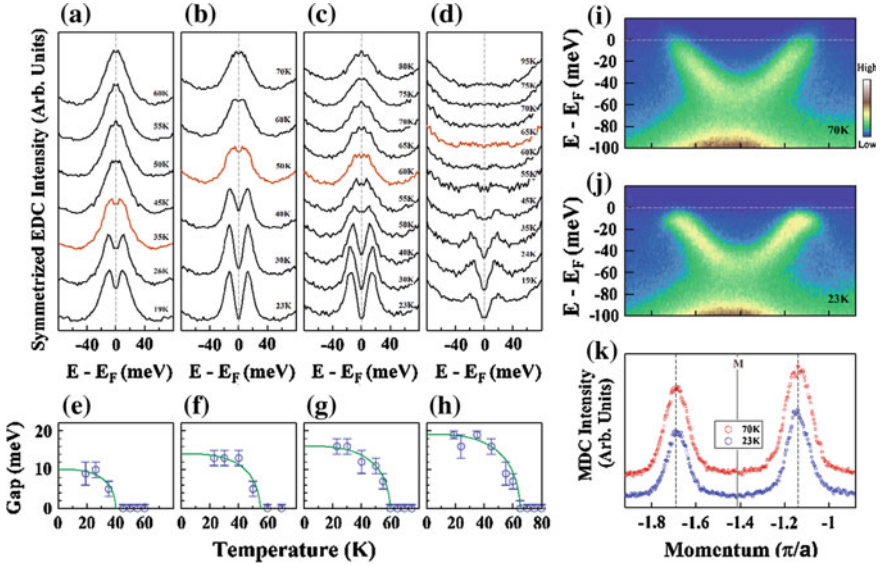


Fig. 7.8 Temperature dependence of the energy gap of the single-layer FeSe film annealed under different conditions. **a–d** Temperature dependence of the symmetrized EDCs at Fermi momentum for different annealing sequences. **e–h** show the corresponding temperature dependence of the energy gap size. **i–j** Band structure along the cut crossing M3 measured at 70 K and 23 K, respectively. The corresponding momentum distribution curves at the Fermi energy are shown in **(k)** [16]

the sequence 15. It is interesting to notice that for a given sequence, the temperature dependence of the gap size roughly follows the BCS form [marked by the green lines in Fig. 7.8e–h].

By optimizing the carrier concentration, a high T_c of 65 ± 5 K can be realized in the single-layer FeSe grown on SrTiO_3 substrate. In fact, both the $T_c \sim 60$ K for the sequence 13 and $T_c \sim 65$ K for the sequence 15 (Fig. 7.8) are higher than the transition temperature record (~ 55 K) [8] for the bulk Fe-based superconductors. The maximum gap size we have obtained by ARPES (~ 19 meV) is smaller but close to the one measured from the STM/STS measurements (~ 20 meV) [1]. Although 65 ± 5 K is the highest T_c we observed so far, we did not find the overdoped region yet. As discussed earlier, too much annealing makes the quality of the sample deteriorate, as seen from the peak broadening and particularly the signal weakening (Fig. 7.8d). Although we have tried to tune the starting point of the film in order to get high electron doping with less annealing, it seems that we cannot go further to achieve higher dopings by annealing and other doping methods are needed for future research.

7.7 Examination of Particle–Hole Symmetry Along the Fermi Surface

While the above energy gap has been carefully examined at various doping levels and attributed to a superconducting gap, a natural question to ask is whether it can be other kinds of gaps. In order to check the particle–hole symmetry and pin down the nature of the gap, detailed momentum dependence [2] and temperature dependence of the gap are shown in Figs. 7.8i–k and 7.9.

In the standard BCS picture, if there is a one-electron-like quasiparticle dispersion crossing the Fermi energy (E_F) with a Fermi momentum k_F in the normal state, upon entering the superconducting state, the formation of Bogoliubov quasiparticles will split the dispersion into two branches. These two branches are separated by the superconducting gap 2Δ and showing back-bending behavior. Since the particle–hole symmetry is conserved during the superconducting transition, the two separated bands should sit symmetrically around the Fermi momentum point with both bending points at k_F . We note that the superconducting gap is the only known case so far which opens along the entire Fermi surface and shows the particle–hole symmetry. In the formation of other electronic orders, such as spin density wave or charge density wave, the gap opens only on the portion of Fermi surface which satisfies

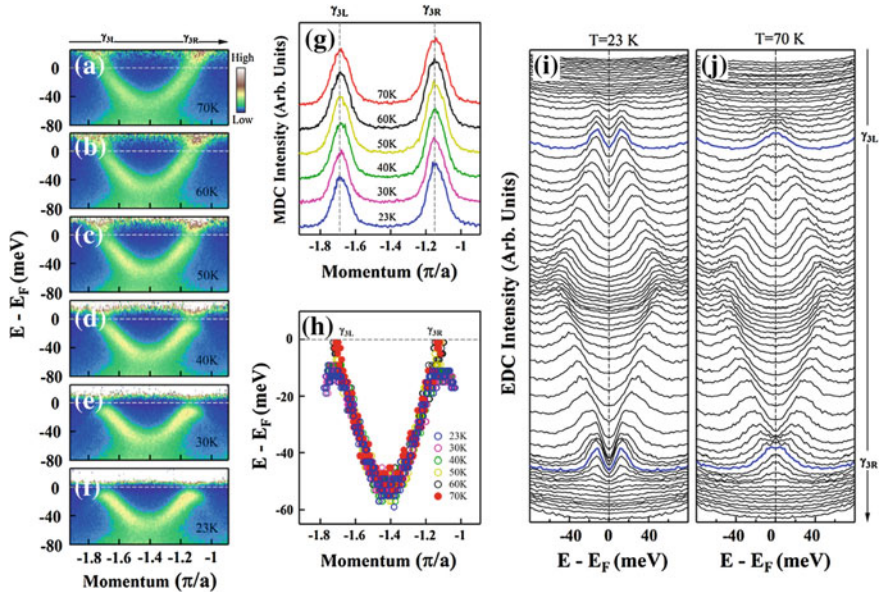


Fig. 7.9 The particle–hole symmetry on the Fermi surface. **a–f** The electron-like bands measured at different temperatures along the cut crossing M3. **g** Temperature dependence of the MDC at Fermi energy. **h** Band dispersions deduced from EDCs as a function of temperature. Symmetrized EDCs at 23 K (**i**) and 70 K (**j**)

the perfect nesting conditions. Moreover, the Fermi momentum is also expected to change its location above and below the transition temperature. Therefore, the examination of the particle–hole symmetry may work as an effective way to identify the superconducting gap.

Figure 7.9 shows the detailed temperature-dependent measurements of the electron-like band near M point in the S phase (annealing sequence 12). Clear Fermi crossings are recognized at 70 K such that the Fermi momenta k_{FS} can be unambiguously determined. The energy gap opens at lower temperatures at which the band back-bending is observed and the bending point can also be clearly identified. Three typical methods have been applied to analyze the data, and all of them point to the conclusion that the particle–hole symmetry is conserved.

First, shown in Fig. 7.9g is the temperature dependence of the momentum distribution curves (MDCs) at the Fermi energy. Little change is found in the peak positions which confirms that the Fermi momenta k_{FS} do not move with temperature.

Second, the dispersion determined by the EDC peaks (Fig. 7.9h) also demonstrates that the Fermi crossing at high temperature is consistent with the bending point at low temperatures.

Third, Fig. 7.9i and j shows the symmetrized EDCs for a low temperature and a high temperature, respectively, in which the Fermi momenta can be determined from the minimum gap locus. The consistency of the Fermi momenta at both temperatures confirms the particle–hole symmetry.

Furthermore, the nearly BCS-like form on the temperature dependence of the gap also indicates that it is unlikely a pseudogap, as observed in cuprates [29].

After identifying the nature of the superconducting gap, another related question is whether one should treat the single-layer FeSe film on the SrTiO₃ substrate as an isolated two-dimensional (2D) FeSe system or as a complex system with strong interfacial effects. Theoretically, in a strict 2D system, one would expect a Kosterlitz–Thouless (KT) transition [30] instead of a superconducting transition. While more efforts are needed to investigate this problem, the fact that the single-layer FeSe film grown on the SrTiO₃ substrate exhibits some distinct behaviors from the bulk FeSe [10] and the FeSe thin films grown on the graphene substrate [21] suggests that the interface must play an important role in the FeSe/SrTiO₃ system.

7.8 Phase Diagram of the Single-Layer FeSe Films

Figure 7.10 summarizes the electronic phase diagram of the single-layer FeSe film during the annealing process. Two distinct phases are observed at two ends of the annealing, respectively. In particular, superconductivity is observed in the S phase with sufficient carrier concentration. The evolution of the superconducting gap (Δ) and the superconducting transition temperature is shown in the phase diagram. Both the superconducting gap and the transition temperature increase with the annealing process. The $2\Delta/k_B T_c$ is around $6 \sim 7$ which indicates that the superconductivity in the single-layer FeSe films is in the strong-coupling regime.

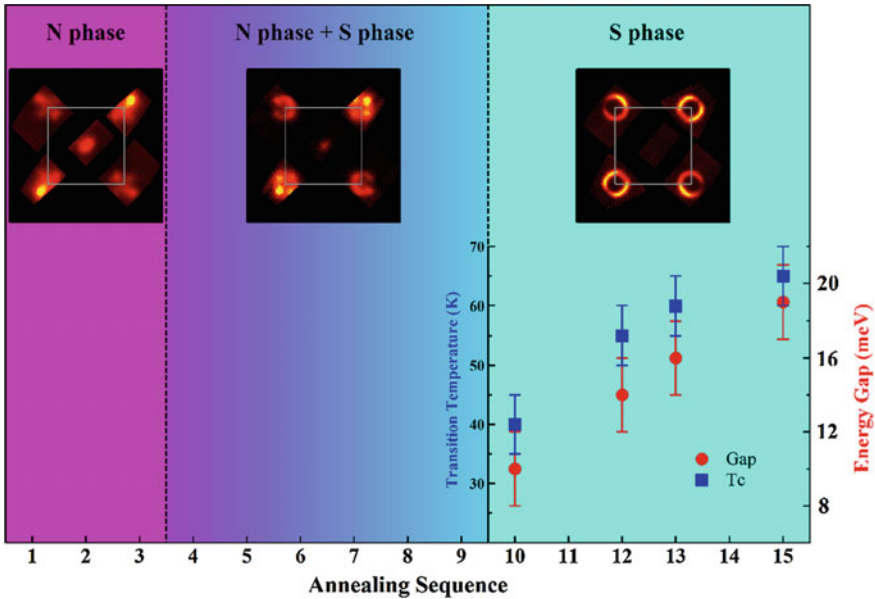


Fig. 7.10 Electronic phase diagram of the single-layer FeSe film [16]

7.9 Summary

In this chapter, the electronic phase diagram of the single-layer FeSe film grown on the SrTiO₃ substrate has been investigated. The electronic structure and physical properties of the films can be tuned by a simple annealing process. Two competing phases can be defined by two sets of distinct electronic structure. N phase appears at the initial annealing sequences in which no signature of superconductivity is observed. S phase appears at higher carrier concentration and competes with N phase. Eventually, superconductivity is realized in S phase with sufficient carriers. The T_c can also be tuned with doping, and a record-high T_c of (65 ± 5) K can be realized in the system under an optimized annealing condition. We note that the current annealing process has not spanned the doping level of the S phase all the way to the over-doped region due to technical difficulties. Therefore, other doping methods are needed for future study. Nevertheless, the current phase diagram we obtained bears similarities with that of other Fe-based superconductors, which sheds light on the understanding of superconductivity and other physical properties in the single-layer FeSe films. The existence of two distinct phases and the tunability of the superconducting properties in the FeSe films have also provided an ideal platform for potential applications which require the combination of a superconductor with other advanced materials [31–33].

References

1. Wang, Q., Li, Z., Zhang, W., Zhang, Z., Zhang, J., Li, W., Ding, H., Ou, Y., Deng, P., Chang, K., Wen, J., Song, C., He, K., Jia, J., Ji, S., Wang, Y., Wang, L., Chen, X., Ma, X., Xue, Q.-K.: Interface-induced high-temperature superconductivity in single unit-cell FeSe films on SrTiO₃. *Chin. Phys. Lett.* **29**(3), 037402 (2012)
2. Liu, D., Zhang, W., Mou, D., He, J., Ou, Y.B., Wang, Q.Y., Li, Z., Wang, L., Zhao, L., He, S., Peng, Y., Liu, X., Chen, C., Yu, L., Liu, G., Dong, X., Zhang, J., Chen, C., Xu, Z., Hu, J., Chen, X., Ma, X., Xue, Q., Zhou, X.J.: Electronic origin of high-temperature superconductivity in single-layer FeSe superconductor. *Nat. Commun.* **3**, 931 (2012)
3. Liu, K., Lu, Z.Y., Xiang, T.: Atomic and electronic structures of FeSe monolayer and bilayer thin films on SrTiO₃ (001): first-principles study. *Phys. Rev. B* **85**(23), 235123 (2012)
4. Bednorz, J.G., Muller, K.A.: Possible high- T_c superconductivity in the Ba-La-Cu O system. *Z. Phys. B Condens. Matter* **64**(2), 189193 (1986)
5. Xiang, Y.Y., Wang, F., Wang, D., Wang, Q.H., Lee, D.H.: High-temperature superconductivity at the FeSe/SrTiO₃ interface. *Phys. Rev. B* **86**(13), 134508 (2012)
6. Lee, P.A., Nagaosa, N., Wen, X.G.: Doping a Mott insulator: physics of high-temperature superconductivity. *Rev. Mod. Phys.* **78**(1), 17–85 (2006)
7. Kamihara, Y., Watanabe, T., Hirano, M., Hosono, H.: Iron-based layered superconductor LaO_{1-x}F_xFeAs ($x = 0.05 - 0.12$) with $T_c = 26$ K. *J. Am. Chem. Soc.* **130**(11), 32963297 (2008)
8. Ren, Z.-A., Lu, W., Yang, J., Yi, W., Shen, X.-L., Li, Z.-C., Che, G.-C., Dong, X.-L., Sun, L.-L., Zhou, F., Zhao, Z.-X.: Superconductivity at 55 K in iron-based f-doped layered quaternary compound SmO_{1-x}F_xFeAs. *Chin. Phys. Lett.* **25**(6), 2215 (2008)
9. Rotter, M., Tegel, M., Johrendt, D.: Superconductivity at 38 K in the iron arsenide (Ba_{1-x}K_x)Fe₂As₂. *Phys. Rev. Lett.* **101**(10), 107006 (2008)
10. Hsu, F.C., Luo, J.Y., Yeh, K.W., Chen, T.K., Huang, T.W., Wu, P.M., Lee, Y.C., Huang, Y.L., Chu, Y.Y., Yan, D.C., Wu, M.K.: Superconductivity in the PbO-type structure α -FeSe. *Proc. Natl. Acad. Sci. USA* **105**(38), 14262–14264 (2008)
11. Wang, X.C., Liu, Q.Q., Lv, Y.X., Gao, W.B., Yang, L.X., Yu, R.C., Li, F.Y., Jin, C.Q.: The superconductivity at 18 K in LiFeAs system. *Solid State Commun.* **148**(11), 538–540 (2008)
12. Paglione, J., Greene, R.L.: High-temperature superconductivity in iron-based materials. *Nat. Phys.* **6**(9), 645–658 (2010)
13. Wang, F., Lee, D.H.: The electron-pairing mechanism of iron-based superconductors. *Science* **332**(6026), 200–204 (2011)
14. Guo, J., Jin, S., Wang, G., Wang, S., Zhu, K., Zhou, T., He, M., Chen, X.: Superconductivity in the iron selenide K_xFe₂Se₂ ($0 \leq x \leq 1.0$). *Phys. Rev. B* **82**(18), 180520(R) (2010)
15. Medvedev, S., McQueen, T.M., Troyan, I.A., Palasyuk, T., Eremets, M.I., Cava, R.J., Naghavi, S., Casper, F., Ksenofontov, V., Wortmann, G., Felser, C.: Electronic and magnetic phase diagram of β -Fe_{1.01}Se with superconductivity at 36.7 K under pressure. *Nat. Mater.* **8**(8), 630–633 (2009)
16. He, S., He, J., Zhang, W., Zhao, L., Liu, D., Liu, X., Mou, D., Ou, Y., Wang, Q., Li, Z., Wang, L., Peng, Y., Liu, Y., Chen, C., Yu, L., Liu, G., Dong, X., Zhang, J., Chen, C., Xu, Z., Chen, X., Ma, X., Xue, Q., Zhou, X.J.: Phase diagram and electronic indication of high-temperature superconductivity at 65 K in single-layer FeSe films. *Nat. Mater.* **12**(7), 605–610 (2013)
17. Zhang, Y., Yang, L.X., Xu, M., Ye, Z.R., Chen, F., He, C., Xu, H.C., Jiang, J., Xie, B.P., Ying, J.J., Wang, X.F., Chen, X.H., Hu, J.P., Matsunami, M., Kimura, S., Feng, D.L.: Nodeless superconducting gap in A_xFe₂Se₂ (A = K, Cs) revealed by angle-resolved photoemission spectroscopy. *Nat. Mater.* **10**(4), 273–277 (2011)
18. Mou, D., Liu, S., Jia, X., He, J., Peng, Y., Zhao, L., Yu, L., Liu, G., He, S., Dong, X., Zhang, J., Wang, H., Dong, C., Fang, M., Wang, X., Peng, Q., Wang, Z., Zhang, S., Yang, F., Xu, Z., Chen, C., Zhou, X.J.: Distinct Fermi surface topology and nodeless superconducting gap in a (Tl_{0.58}Rb_{0.42})Fe_{1.72}Se₂ superconductor. *Phys. Rev. Lett.* **106**(10), 107001 (2011)

19. Zhao, L., Mou, D., Liu, S., Jia, X., He, J., Peng, Y., Yu, L., Liu, X., Liu, G., He, S., Dong, X., Zhang, J., He, J.B., Wang, D.M., Chen, G.F., Guo, J.G., Chen, X.L., Wang, X., Peng, Q., Wang, Z., Zhang, S., Yang, F., Xu, Z., Chen, C., Zhou, X.J.: Common Fermi-surface topology and nodeless superconducting gap of $K_{0.68}Fe_{1.79}Se_2$ and $(Tl_{0.45}K_{0.34})Fe_{1.84}Se_2$ superconductors revealed via angle-resolved photoemission. *Phys. Rev. B* **83**(14), 140508(R) (2011)
20. Qian, T., Wang, X.P., Jin, W.C., Zhang, P., Richard, P., Xu, G., Dai, X., Fang, Z., Guo, J.-G., Chen, X.-L., Ding, H.: Absence of a holelike Fermi surface for the iron-based $K_{0.8}Fe_{1.7}Se_2$ superconductor revealed by angle-resolved photoemission spectroscopy. *Phys. Rev. Lett.* **106**(18), 187001 (2011)
21. Song, C.L., Wang, Y.L., Jiang, Y.P., Li, Z., Wang, L., He, K., Chen, X., Ma, X., Xue, Q.-K.: Molecular-beam epitaxy and robust superconductivity of stoichiometric FeSe crystalline films on bilayer graphene. *Phys. Rev. B* **84**(2), 020503(R) (2011)
22. Yang, L.X., Zhang, Y., Ou, H.W., Zhao, J.F., Shen, D.W., Zhou, B., Wei, J., Chen, F., Xu, M., He, C., Chen, Y., Wang, Z.D., Wang, X.F., Wu, T., Wu, G., Chen, X.H., Arita, M., Shimada, K., Taniguchi, M., Lu, Z.Y., Xiang, T., Feng, D.L.: Electronic structure and unusual exchange splitting in the spin-density-wave state of the $BaFe_2As_2$ parent compound of iron-based superconductors. *Phys. Rev. Lett.* **102**(10), 107002 (2009)
23. Liu, H., Zhang, W., Zhao, L., Jia, X., Meng, J., Liu, G., Dong, X., Chen, G., Luo, J.L., Wang, N.L., Lu, W., Wang, G., Zhou, Y., Zhu, Y., Wang, X., Xu, Z., Chen, C., Zhou, X.J.: Fermi surface and band renormalization of $Sr_{1-x}K_xFe_2As_2$ from angle-resolved photoemission spectroscopy. *Phys. Rev. B* **78**(18), 184514 (2008)
24. Liu, G., Liu, H., Zhao, L., Zhang, W., Jia, X., Meng, J., Dong, X., Zhang, J., Chen, G., Wang, G., Zhou, Y., Zhu, Y., Wang, X., Xu, Z., Chen, C., Zhou, X.J.: Band-structure reorganization across the magnetic transition in $BaFe_2As_2$ seen via high-resolution angle-resolved photoemission. *Phys. Rev. B* **80**(13), 134519 (2009)
25. Richard, P., Nakayama, K., Sato, T., Neupane, M., Xu, Y.M., Bowen, J.H., Chen, G.F., Luo, J.L., Wang, N.L., Dai, X., Fang, Z., Ding, H., Takahashi, T.: Observation of Dirac cone electronic dispersion in $BaFe_2As_2$. *Phys. Rev. Lett.* **104**(13), 137001 (2010)
26. Tamai, A., Ganin, A.Y., Rozbicki, E., Bacsá, J., Meevasana, W., King, P.D.C., Caffio, M., Schaub, R., Margadonna, S., Prassides, K., Rosseinsky, M.J., Baumberger, F.: Strong electron correlations in the normal state of the iron-based $FeSe_{0.42}Te_{0.58}$ superconductor observed by angle-resolved photoemission spectroscopy. *Phys. Rev. Lett.* **104**(9), 097002 (2010)
27. Liu, C., Kondo, T., Fernandes, R.M., Palczewski, A.D., Mun, E.D., Ni, N., Thaler, A.N., Bostwick, A., Rotenberg, E., Schmalian, J., Bud'ko, S.L., Canfield, P.C., Kaminski, A.: Evidence for a Lifshitz transition in electron-doped iron arsenic superconductors at the onset of superconductivity. *Nat. Phys.* **6**(6), 419–423 (2010)
28. Norman, M.R., Randeria, M., Ding, H., Campuzano, J.C.: Phenomenology of the low-energy spectral function in high- T_c superconductors. *Phys. Rev. B* **57**, 11093–11096(R) (1998)
29. Timusk, T., Statt, B.: The pseudogap in high-temperature superconductors: an experimental survey. *Rep. Prog. Phys.* **62**(1), 61 (1999)
30. Kosterlitz, J.M., Thouless, D.J.: Ordering, metastability and phase transitions in two-dimensional systems. *J. Phys. C: Solid State Phys.* **6**(7), 1181 (1973)
31. Bozovic, I., Logvenov, G., Verhoeven, M.A.J., Caputo, P., Goldobin, E., Geballe, T.H.: No mixing of superconductivity and antiferromagnetism in a high-temperature superconductor. *Nature* **422**(6934), 873–875 (2003)
32. Fu, L., Kane, C.L.: Superconducting proximity effect and Majorana fermions at the surface of a topological insulator. *Phys. Rev. Lett.* **100**(9), 096407 (2008)
33. Wang, M.-X., Liu, C., Xu, J.-P., Yang, F., Miao, L., Yao, M.-Y., Gao, C.L., Shen, C., Ma, X., Chen, X., Xu, Z.-A., Liu, Y., Zhang, S.-C., Qian, D., Jia, J.-F., Xue, Q.-K.: The coexistence of superconductivity and topological order in the Bi_2Se_3 thin films. *Science* **336**(6077), 52–55 (2012)

Chapter 8

Insulator-Superconductor Crossover in Single-Layer FeSe/SrTiO₃ Films

After extensive research on the doping evolution of the high-temperature cuprate superconductors, it is now generally agreed that superconductivity is realized by doping an antiferromagnetic Mott insulator. The doping-induced insulator to superconductor transition has been widely observed in cuprates which provides important information and constraints for the superconductivity mechanism. In particular, the concomitant strong electron correlation has been considered very important. The observation of high-temperature superconductivity in iron-based superconductors has provided another platform to study the high T_c problem. However, the parent compound for some iron-based superconductors is antiferromagnetic bad metal and no evidence of doping-induced insulator-superconductor transition has been reported so far, raising a debate on whether strong electron correlation should be considered [1, 2]. Alternatively, the itinerant picture has been suggested to capture the main properties of iron-based superconductors [1]. Therefore, the correct identification of an appropriate starting point is of great importance for understanding the superconductivity mechanism in iron-based superconductors. The observation of high-temperature superconductivity in single-layer FeSe grown on SrTiO₃ substrate has generated much current interests [3–10]. As stated in the previous chapters that this single-layer FeSe film has the simplest crystal structure but holds the highest T_c in iron-based superconductors. Therefore, it is an ideal system to study the superconductivity mechanism. In this chapter, we introduce the electronic evidence of an insulator-superconductor crossover observed in the single-layer FeSe/SrTiO₃ films. By measuring the electronic structure and energy gap, we have observed a clear evolution of an insulator to a superconductor with increasing carrier concentration. This insulator-superconductor crossover bears clear resemblance to that observed in various cuprates. These results suggest that the two-dimensionality and interfacial effect in this system have enhanced electron localization and/or correlation. They have provided not only a bridge connecting cuprates and iron-based superconductors but also a unique pathway toward finding new superconductors with a higher transition temperature.

8.1 Introduction

In cuprate superconductors, continuous efforts have been spent on the study of the doping evolution with a particular emphasis on the insulator to superconductor transition. It is now generally agreed that the superconductivity in cuprates is realized by doping a Mott insulator and strong electron correlation is important [11]. Iron-based superconductors represent the second class of high-temperature superconductors in which a key question under debate is whether an appropriate starting point should go with an itinerant picture or a localized picture. The observation of a poor metallic behavior in the parent compounds of FeAs-related materials seems to support the itinerant picture, e.g., the Fermi surface nesting scenario [1]. However, the existence of high T_c in $A_x\text{Fe}_{2-y}\text{Se}_2$ ($A = \text{K, Cs, Rb, Tl}$) [12–14], whose parent phase might be insulating, has stimulated a reconsideration of the strong electron correlation in iron-based superconductors [2]. Nevertheless, the complicated phases in $A_x\text{Fe}_{2-y}\text{Se}_2$ ($A = \text{K, Cs, Rb, Tl}$) make it hard to identify the real superconducting phase and parent phase. Therefore, no clear experimental evidence of doping-induced insulator-superconductor transition has been reported in the iron-based superconductors so far.

The latest discovery of high-temperature superconductivity in single-layer FeSe/SrTiO₃ films has attracted much attention both experimentally [3–6] and theoretically [7–10]. The reduced dimensionality and enhanced interfacial effect make this system distinct from its bulk counterpart which provides an ideal platform to study the insulator-superconductor crossover. First, the single-layer FeSe film only consists of a Se-Fe-Se unit which is an essential building block of the iron-based superconductors. Second, an insulating energy gap was found in the single-layer FeSe film before post annealing whereas a superconducting phase was clearly identified after sufficient annealing. In particular, it was found that annealing in vacuum can tune the carrier concentration of the FeSe/SrTiO₃ films, thus providing a good opportunity to investigate its carrier-dependent behaviors. Third, comparing to $A_x\text{Fe}_{2-y}\text{Se}_2$ ($A = \text{K, Cs, Rb, Tl}$), the phase diagram in single-layer FeSe is simple and clear.

It has been clearly shown in last chapter [5] that there is a dramatic change in the electronic structure with annealing. Two sets of bands can be identified representing two distinct phases (N phase and S phase). An insulating-like energy gap was found in N phase and the superconductivity was found in S phase. Therefore, a direct question to address is when the insulator to superconductor transition takes place. Is it a concomitant transition with the dramatic change between the two sets of electronic bands? Alternatively, could it be a process taking place in the S phase with the insulating gap gradually filled by electron doping? In order to answer these questions, a systematic doping-dependent study has been performed and will be presented in this chapter.

8.2 Materials and Methods

The single-layer FeSe films were prepared on the SrTiO₃ substrate ($\sim 0.5\%$ Nb doped) by the molecular beam epitaxy (MBE) method and characterized by scanning tunneling microscope. The carrier concentration of the film was tuned by the post annealing at different temperatures and for different times. The carrier concentration was calculated by estimating the area of the Fermi surface measured by ARPES. For simplicity, we call the sample with carrier concentration x as sample x hereafter.

Angle-resolved photoemission (ARPES) measurements were performed on our laboratory system equipped with a Scienta R4000 analyzer. The helium lamp with a photon energy of 21.218 eV was used as the light source. The energy resolution was set between 4 \sim 10 meV. In order to selectively probe the electronic structure of the S phase even when it coexists with the N phase, a proper measurement geometry was selected to suppress the signal from N phase by the photoemission matrix element effect. The Fermi level is referenced to that of a polycrystalline gold.

8.3 Doping Evolution of the Energy Gaps in Single-Layer FeSe/SrTiO₃ Films

The as-grown FeSe/SrTiO₃ films were covered with an amorphous Se capping layer and transferred into the ARPES system. Consecutive annealing process was then carried out, during which two different phases were identified in the single-layer FeSe/SrTiO₃ films by their distinct electronic structures: The initial N phase possesses an electronic structure showing some similarities to that of the parent compound of BaFe₂As₂ in its magnetic state, whereas the S phase shows only electron pockets near the (π, π) zone corners.

In order to understand the insulator to superconductor transition, the primary question to address is, as soon as the S phase emerges with vacuum annealing, whether it is insulating, metallic, or superconducting. Shown in Fig. 8.1 a–e is the band structure evolution with the carrier concentration for the S phase in the single-layer FeSe/SrTiO₃ films. The measurement was performed at ~ 20 K along a momentum cut near M2 point in the Brillouin zone, as marked in the inset of Fig. 8.1a. At a very low carrier concentration, the spectral weight of the electron-like bands in the S phase of the single-layer FeSe/SrTiO₃ film is very weak showing an energy gap at the Fermi level. It gets stronger with the increasing carrier concentration. Symmetrized photoemission spectra (energy distribution curves, EDCs) are shown in Fig. 8.1f–j with the ones at the Fermi momentum of the electron-like band plotted in Fig. 8.1k. The symmetrization procedure can remove the effect of the Fermi distribution function and provides an intuitive way of discerning a gap opening. At a carrier concentration lower than 0.073, there is a gap opening indicated by a spectral dip at the Fermi level. The spectral weight suppression gets weaker with increasing carrier concentration and the gap size, measured by the half-distance between the

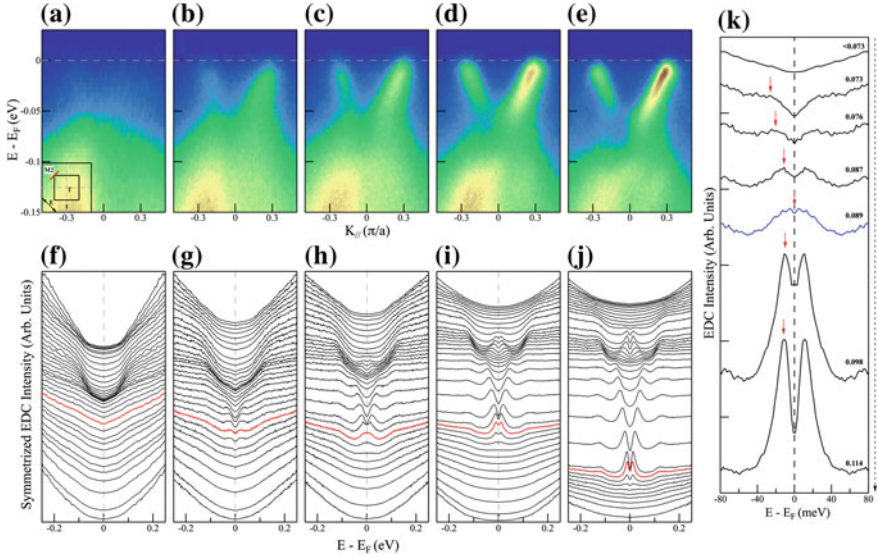


Fig. 8.1 The evolution of the energy gap on S-phase single-layer FeSe as a function of carrier concentration. **a–e** The evolution of the energy band crossing M2 as a function of carrier concentration. **f–j** The corresponding EDCs. **k** The EDC at Fermi momentum M2 as a function of carrier concentration

EDC peaks, closes at $x = 0.089$. However, further increase of the carrier concentration leads to a clear reopening of an energy gap as clearly seen in the samples with carrier concentration of 0.098 and 0.114.

8.4 Two Distinct Gaps

In order to understand the nature of the two gaps at different carrier concentrations, one that opens at carrier concentration lower than 0.089 and the other that opens at carrier concentration higher than 0.089, detailed temperature-dependent measurements have been performed in the S phase of the single-layer FeSe/SrTiO₃ films.

8.4.1 Different Temperature Dependence of the Gap Size

Different temperature dependence has been clearly observed for these two gaps. The energy gap at high carrier concentration shows a clear temperature dependence which closes above a critical temperature, e.g., ~ 40 K in Fig. 8.2b for the 0.098 sample. The gap size as a function of temperature follows a simple BCS-like form (Fig. 8.2d). The temperature dependence, as well as the strong coherence peak (Fig. 8.2b) and

the particle–hole symmetry reported in last chapter, strongly indicates that this high carrier concentration gap is a superconducting gap. On the other hand, the energy gap at low carrier concentration exhibits different behaviors. First, comparing to the coherent peak for the high carrier concentration gap, the EDC peak for the low carrier concentration gap is relatively broad at all temperatures. Thermal broadening makes it even weaker at high temperature (Fig. 8.2a, 0.076 sample). Second, the gap size shows little temperature dependence till the highest temperature we have measured (75 K in Fig. 8.2a and c for the 0.076 sample). Third, the gap size is very large, e.g.,

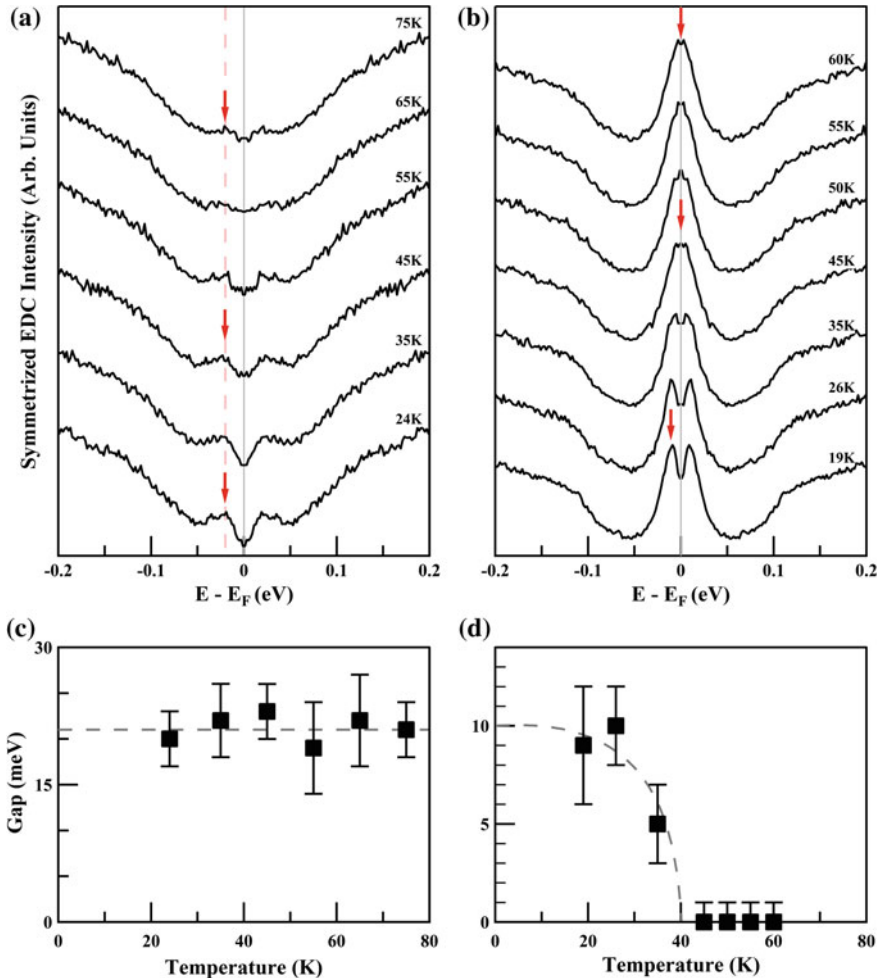


Fig. 8.2 Different temperature dependence of the two energy gaps for the S-phase FeSe films. **a, c** Insulating-like gap showing little temperature dependence. **b, d** The superconducting gap shows a clear temperature dependence [15]

up to ~ 50 meV for the sample with a carrier concentration less than 0.073. This gap is much larger than the largest superconducting gap observed in the single-layer FeSe/SrTiO₃ film [3–6]. The distinct temperature dependence indicates that the low carrier concentration energy gap does not represent the superconducting gap. On the contrary, it is more consistent with an insulating gap.

8.4.2 Different Temperature Dependence of the Peak Intensity

More evidence comes from the temperature dependence of the EDC peak intensity. As has been demonstrated in cuprates that the EDC peak at k_F should be greatly enhanced when the sample enters superconducting state with cooling. This sudden enhancement is related to the formation of superconducting coherent peak. Shown in Fig. 8.3c and f is the temperature dependence of the k_F EDC peak intensity measured

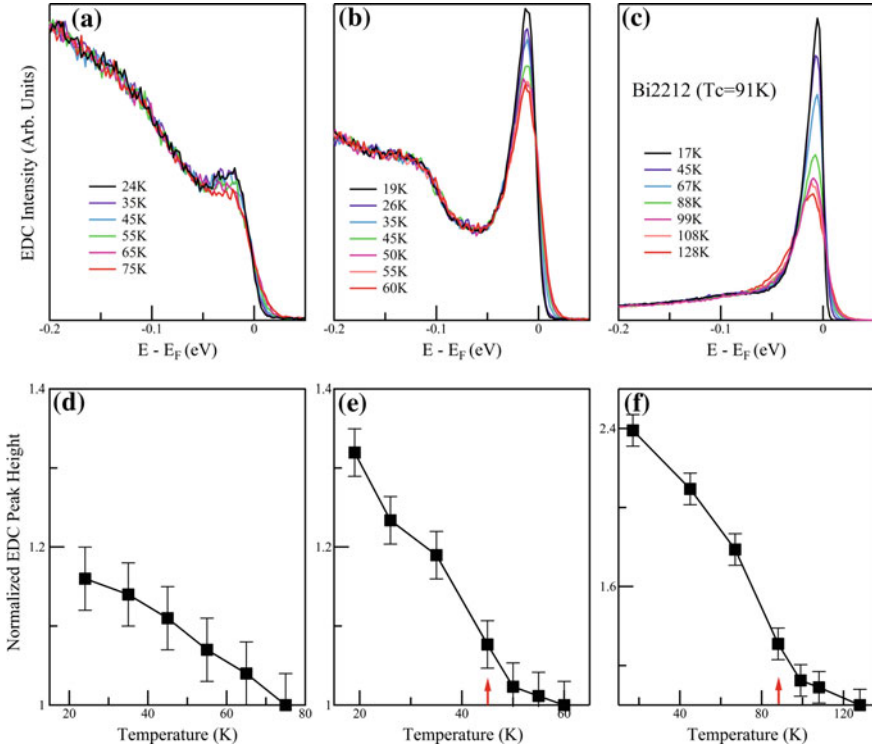


Fig. 8.3 Different temperature dependence of the EDC peak for the two energy gaps. **a** and **b** Different temperature dependence of the EDC. **d** and **e** Different temperature dependence of the EDC peak height. **c** and **f** The EDC at the Fermi momentum of the nodal cut for Bi2212 and its peak height measured at different temperatures

on cuprate superconductor Bi2212 along the nodal direction [16]. It is evident that a sudden peak intensity change takes place at ~ 91 K which is the superconducting transition temperature of the sample. Similar measurements have been done on sample 0.076 and 0.098, respectively. Similar sudden enhancement of the k_F EDC peak is clearly observed in sample 0.098. As shown in Fig. 8.3b, only slight change in peak intensity is observed above 50 K which can be well addressed by the temperature broadening of the electron band. However, a clear enhancement of the EDC peak shows up at 45 K which indicates the appearance of the superconductivity. This critical temperature is also consistent with the gap closing temperature (40 ± 5 K) for the sample. The detailed temperature evolution of the k_F EDC peak for sample 0.098 is summarized in Fig. 8.3e with the critical temperature marked by the red arrow. The same analysis has been applied to sample 0.076. However, no emergent change of the peak intensity is found (Fig. 8.3a and b). The gradual but slight increase of the peak intensity with cooling is simply due to smaller broadening at lower temperature. This observation is consistent with the earlier conclusion that the low carrier concentration energy gap has a different origin from that of a superconducting gap. Therefore, we conclude that there is a doping-induced insulator to superconductor crossover in the S phase of the single-layer FeSe/SrTiO₃ films.

8.5 Similar Doping Evolution Between S Phase of FeSe Films and Cuprates

It is interesting to note that the insulator to superconductor crossover as well as the overall doping evolution of the S-phase single-layer FeSe/SrTiO₃ films show clear resemblance to that of the cuprates. In order to illustrate the similarities, the electronic structures of two typical cuprate materials, La-doped Bi₂Sr₂CuO_{6+ δ} and La_{2-x}Sr_xCuO₄, are presented as a function of carrier concentration and compared with that of the S-phase FeSe films, respectively.

8.5.1 *Single-Layer FeSe/SrTiO₃ Films and La-doped Bi₂Sr₂CuO_{6+ δ}*

Figure 8.4 compares the doping evolution of the band structure for the S phase in the single-layer FeSe/SrTiO₃ films (a–g) with that of the La-doped Bi₂Sr₂CuO_{6+ δ} (La-Bi2201) [17] (h–n). The momentum locations of the cuts are shown in Fig. 8.4o and p, respectively. It has been shown that in the heavily underdoped La-Bi2201, there is an insulator-superconductor transition which occurs near the doping level of ~ 0.10 . Below this doping level, an energy gap persists along the nodal direction and the entire Fermi surface is gapped [17]. When the doping level gets higher, superconductivity starts to appear. The same is true for the S phase of the single-layer FeSe/SrTiO₃

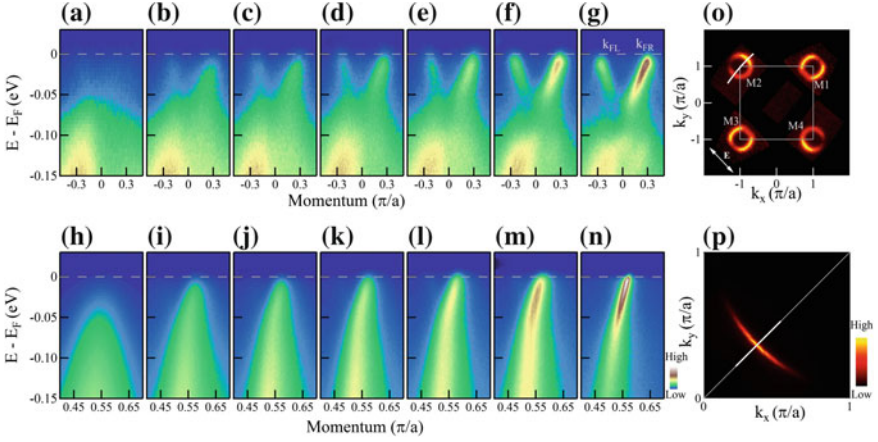


Fig. 8.4 Comparison of the band structure of the S phase in the single-layer FeSe/SrTiO₃ film and La-Bi2201 as a function of carrier concentration. **a–g** Energy band along the cut crossing M2 with the carrier concentrations of <0.073, 0.073, 0.076, 0.087, 0.089, 0.098, and 0.114, respectively. **h–n** The band structure evolution of La-Bi2201 with doping levels of 0.03, 0.04, 0.055, 0.07, 0.08, 0.10, and 0.16, respectively. The corresponding locations of the momentum cuts for the two materials are shown in **(o)** and **(p)**, respectively [15]

films. At a very low carrier concentration, the spectral weight of the electron-like bands is rather weak (Fig. 8.4a). The bands get stronger with the increasing carrier concentration, indicating the accumulation of spectral weight near the Fermi level which eventually leads to the insulator to superconductor transition/crossover.

8.5.2 Single-Layer FeSe/SrTiO₃ Films and La_{2-x}Sr_xCuO₄

Similar doping evolution of the band structure can also be found between the S phase in the single-layer FeSe/SrTiO₃ films and La_{2-x}Sr_xCuO₄ [18, 19]. In La_{2-x}Sr_xCuO₄ (Fig. 8.5 [18, 19]), the EDC at k_F shows little spectral weight at the Fermi level when the doping level is lower than 0.03. As the doping increases, a peak first emerges near the Fermi level, then gets stronger, and becomes a well-defined sharp peak at a doping level higher than 0.10 (Fig. 8.5n [18, 19]). The similar evolution is also found in S-phase single-layer FeSe/SrTiO₃ films (Fig. 8.5m). At a carrier concentration lower than 0.073, little spectral weight is shown at the Fermi level (Fig. 8.5a and m), indicating a large insulating gap. With increasing carrier concentration, spectral weight starts to appear near the Fermi level (e.g., Fig. 8.5b) and a peak emerges in the corresponding EDC at k_F . A well-defined coherent peak can be found at high carrier concentration like $x = 0.114$, indicating the appearance of superconductivity.

The above electronic evidences have clearly illustrated the similarities between the S phase in the single-layer FeSe/SrTiO₃ films and cuprates as a function of carrier

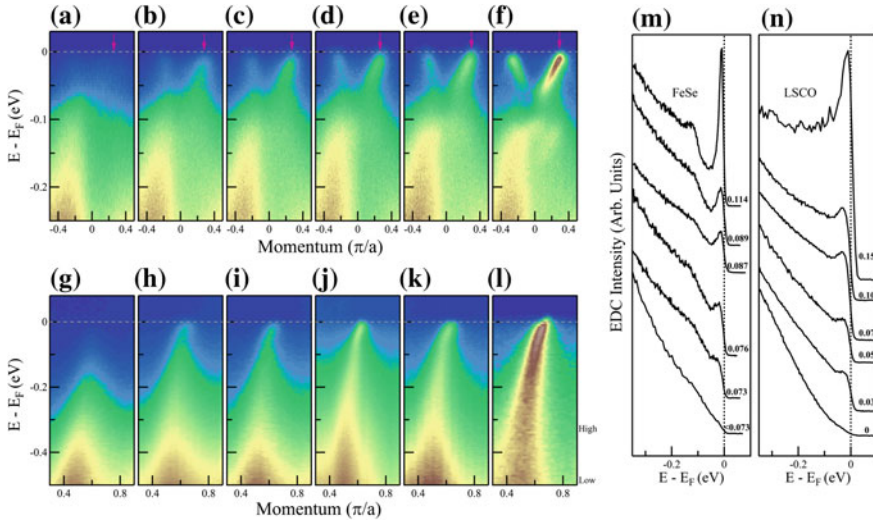


Fig. 8.5 Comparison of the band structure of the S phase in the single-layer FeSe/SrTiO₃ film and La_{2-x}Sr_xCuO₄ as a function of carrier concentration. **a–f** Evolution of the energy band of the S-phase FeSe film with the carrier concentration. The corresponding EDCs at Fermi momenta are shown in **(m)**. **g–l**, Evolution of the band structure of La_{2-x}Sr_xCuO₄. The corresponding EDCs at Fermi momenta are shown in **(n)**

concentration. At low carrier concentration, the S-phase single-layer FeSe film shows an insulating behavior with little spectral weight near the Fermi level. The gap size decreases with increasing carrier concentration, and near $x = 0.089$, the insulating gap approaches zero. Right after this carrier concentration, superconductivity starts to emerge with the appearance of a sharp coherent peak in the photoemission spectra.

On the other hand, we also notice some distinctions between single-layer FeSe/SrTiO₃ film and cuprates. First, in the La-Bi2201 system, the parent compound is an antiferromagnetic insulator. The nodal gap decreases with increasing doping and approaches zero at ~ 0.10 , together with the disappearance of the three-dimensional antiferromagnetism. In the single-layer FeSe/SrTiO₃ film, however, it remains unclear whether there is magnetic order in the S phase at low carrier concentration. Second, the cuprate bulk materials are quasi-two-dimensional and they become three-dimensional upon entering the superconducting state. The single-layer FeSe/SrTiO₃ is an ideal two-dimensional system, which remains to be two-dimensional even in the superconducting state.

8.6 Origin of the Insulator-Superconductor Crossover and Strong Electron Correlation

We note that neither the insulating gap nor the ~ 20 meV superconducting gap was observed in bulk FeSe single crystal; therefore, the observed gap evolution with carrier concentration in single-layer FeSe/SrTiO₃ films is not simply from FeSe itself. On the other hand, the reduced dimensionality and interfacial effect may play an important role. It has been shown that many exotic emergent phenomena can take place in two-dimensional systems with strong interfacial effect. For example, in LaAlO₃/SrTiO₃ system, a pseudogap behavior and carrier density-induced insulator to superconductor transition have been observed which are analogous to those in cuprates. In principle, all electrons in two-dimensional systems are localized even for the smallest levels of disorder. The electrons can be spatially localized, either as a consequence of the random potential, which leads to Anderson localization, or of interactions, which results in a Mott insulator, or a combination of both.

We notice that some residual Se adatoms might appear on the sample surface in the initial stage of annealing. The amount of Se adatoms decreases with annealing. In the final stage of annealing, however, some Se vacancies tend to appear. On the one hand, the decreasing of Se adatoms is consistent with an insulator-superconductor crossover caused by weakened disorder effect, if the insulating state is due to the disorder-induced Anderson localization. On the other hand, the enhanced disorder effect from the Se vacancy formation in the final stage of annealing is inconsistent with this scenario.

Alternatively, electron correlation might also play a role in the observed insulator-superconductor crossover since strong electron correlation might push the system to the verge of Mott physics region. Several observations are consistent with this possibility. First, theoretical calculations have predicted that the iron-based superconductors may be on the verge of the doped Mott insulator [20] and electron correlation in the iron chalcogenides is stronger than that in the iron pnictides. The electron correlation in the single-layer FeSe film can be further enhanced by its two-dimensionality as well as the tensile stress exerted from the SrTiO₃ substrate. Therefore, the single-layer FeSe/SrTiO₃ film may exhibit the strongest electron correlation among all the iron-based superconductors. Second, in a multiorbital system the carrier density-induced Mott transition may be realized in an orbital-selective fashion in which the bands with a particular orbital may behave like a Mott insulator while the others remain the metallic behavior. Such an orbital-selective Mott transition has been observed in iron-based compounds. For example, in A_xFe_{2-y}Se₂ superconductor, the d_{xy} orbital which forms an electron-like band near the M(π , π) point is found to be responsible for such a Mott transition. We note that the same d_{xy} orbital forms the electron-like band near M point in the S phase of the single-layer FeSe/SrTiO₃ film. Third, strong electron correlation is generally considered to be important in cuprate superconductors, and the superconductivity is believed to be realized by doping the Mott insulator. The similar doping evolution of the band structure and the similar insulator to super-

conductor transition observed in the S phase of the single-layer FeSe/SrTiO₃ film and underdoped cuprates strongly suggest the importance of electron correlation in the single-layer FeSe films.

8.7 Summary

In summary, systematic study has been carried out on the carrier evolution of the S phase in the single-layer FeSe/SrTiO₃ films. An insulator-superconductor crossover has been clearly identified with increasing carrier concentration. It may represent the first example of a carrier density-induced insulator-superconductor crossover in the iron-based superconductors. Different scenarios, such as the Anderson localization and the orbital-selective Mott transition, have been discussed as the potential origin of the insulator-superconductor crossover in this system. While more efforts considering the reduced dimensionality and enhanced interfacial effect are needed to pin down the exact origin, the similar band evolution as a function of carrier concentration between the single-layer FeSe/SrTiO₃ films and the cuprate superconductors indicates the possible existence of strong electron correlation in the FeSe/SrTiO₃ system.

References

1. Mazin, I.I., Johannes, M.D.: A key role for unusual spin dynamics in ferropnictides. *Nat. Phys.* **5**(2), 141–145 (2009)
2. Yu, R., Si, Q.: Mott transition in multiorbital models for iron pnictides. *Phys. Rev. B* **84**(23), 235115 (2011)
3. Wang, Q., Li, Z., Zhang, W., Zhang, Z., Zhang, J., Li, W., Ding, H., Ou, Y., Deng, P., Chang, K., Wen, J., Song, C., He, K., Jia, J., Ji, S., Wang, Y., Wang, L., Chen, X., Ma, X., Xue, Q.-K.: Interface-induced high-temperature superconductivity in single unit-cell FeSe films on SrTiO₃. *Chin. Phys. Lett.* **29**(3), 037402 (2012)
4. Liu, D., Zhang, W., Mou, D., He, J., Ou, Y.B., Wang, Q.Y., Li, Z., Wang, L., Zhao, L., He, S., Peng, Y., Liu, X., Chen, C., Yu, L., Liu, G., Dong, X., Zhang, J., Chen, C., Xu, Z., Hu, J., Chen, X., Ma, X., Xue, Q., Zhou, X.J.: Electronic origin of high-temperature superconductivity in single-layer FeSe superconductor. *Nat. Commun.* **3**, 931 (2012)
5. He, S., He, J., Zhang, W., Zhao, L., Liu, D., Liu, X., Mou, D., Ou, Y., Wang, Q., Li, Z., Wang, L., Peng, Y., Liu, Y., Chen, C., Yu, L., Liu, G., Dong, X., Zhang, J., Chen, C., Xu, Z., Chen, X., Ma, X., Xue, Q., Zhou, X.J.: Phase diagram and electronic indication of high-temperature superconductivity at 65 K in single-layer FeSe films. *Nat. Mater.* **12**(7), 605–610 (2013)
6. Tan, S., Zhang, Y., Xia, M., Ye, Z., Chen, F., Xie, X., Peng, R., Xu, D., Fan, Q., Xu, H., Jiang, J., Zhang, T., Lai, X., Xiang, T., Hu, J., Xie, B., Feng, D.L.: Interface-induced superconductivity and strain-dependent spin density waves in FeSe/SrTiO₃ thin films. *Nat. Mater.* **12**(7), 634–640 (2013)
7. Liu, K., Lu, Z.Y., Xiang, T.: Atomic and electronic structures of FeSe monolayer and bilayer thin films on SrTiO₃ (001): first-principles study. *Phys. Rev. B* **85**(23), 235123 (2012)
8. Xiang, Y.Y., Wang, F., Wang, D., Wang, Q.H., Lee, D.H.: High-temperature superconductivity at the FeSe/SrTiO₃ interface. *Phys. Rev. B* **86**(13), 134508 (2012)

9. Bazhiron, T., Cohen, M.L.: Effects of charge doping and constrained magnetization on the electronic structure of an FeSe monolayer. *J. Phys.: Condens. Matter* **25**(10), 105506 (2013)
10. Zheng, F., Wang, Z., Kang, W., Zhang, P.: Antiferromagnetic FeSe monolayer on SrTiO₃: the charge doping and electric field effects. *Sci. Rep.* **3**, 2213 (2013)
11. Lee, P.A., Nagaosa, N., Wen, X.G.: Doping a Mott insulator: physics of high-temperature superconductivity. *Rev. Mod. Phys.* **78**(1), 17–85 (2006)
12. Guo, J., Jin, S., Wang, G., Wang, S., Zhu, K., Zhou, T., He, M., Chen, X.: Superconductivity in the iron selenide K_xFe₂Se₂ (0 ≤ x ≤ 1.0). *Phys. Rev. B* **82**(18), 180520(R) (2010)
13. Fang, M.H., Wang, H.D., Dong, C.H., Li, Z.J., Feng, C.M., Chen, J., Yuan, H.Q.: Fe-based superconductivity with T_c = 31 K bordering an antiferromagnetic insulator in (Tl, K)Fe_xSe₂. *Europhys. Lett.* **94**(2), 27009 (2011)
14. Mou, D.X., Zhao, L., Zhou, X.J.: Structural, magnetic and electronic properties of the iron-chalcogenide A_xFe_{2-y}Se₂ (A = K, Cs, Rb, and Tl, etc.) superconductors. *Front. Phys.* **6**(4), 410–428 (2011)
15. He, J., Liu, X., Zhang, W., Zhao, L., Liu, D., He, S., Mou, D., Li, F., Tang, C., Li, Z., Wang, L., Peng, Y., Liu, Y., Chen, C., Yu, L., Liu, G., Dong, X., Zhang, J., Chen, C., Xu, Z., Chen, X., Ma, X., Xue, Q., Zhou, X.J.: Electronic evidence of an insulator-superconductor crossover in single-layer FeSe/SrTiO₃ films. *Proc. Natl. Acad. Sci. USA* **111**(52), 18501–18506 (2014)
16. Zhang, W.T.: A study of Bi₂Sr₂CaCu₂O₈ by laser-based angle-resolved photoemission. Springer Theses Recognizing Outstanding Ph.D. Research. (2012). doi:[10.1007/978-3-642-32472-7](https://doi.org/10.1007/978-3-642-32472-7)
17. Peng, Y., Meng, J., Mou, D., He, J., Zhao, L., Wu, Y., Liu, G., Dong, X., He, S., Zhang, J., Wang, X., Peng, Q., Wang, Z., Zhang, S., Yang, F., Chen, C., Xu, Z., Lee, T.K., Zhou, X.J.: Disappearance of nodal gap across the insulator-superconductor transition in a copper-oxide superconductor. *Nat. Commun.* **4**, 2459 (2013)
18. Damascelli, A., Hussain, Z., Shen, Z.-X.: Angle-resolved photoemission studies of the cuprate superconductors. *Rev. Mod. Phys.* **75**, 473–541 (2003)
19. Yoshida, T., Zhou, X.J., Sasagawa, T., Yang, W.L., Bogdanov, P.V., Lanzara, A., Hussain, Z., Mizokawa, T., Fujimori, A., Eisaki, H., Shen, Z.X., Kakeshita, T., Uchida, S.: Metallic behavior of lightly doped La_{2-x}Sr_xCuO₄ with a Fermi surface forming an arc. *Phys. Rev. Lett.* **91**(2), 027001 (2003)
20. Si, Q., Abrahams, E.: Strong correlations and magnetic frustration in the high T_c iron pnictides. *Phys. Rev. Lett.* **101**(7), 076401 (2008)